DEVELOPMENT OF EFFICIENT NUMERICAL MODELS FOR THE SIMULATION OF LOW VELOCITY IMPACT AND COMPRESSION AFTER IMPACT ON COMPOSITE STRUCTURES

Albert Soto Masip

Universitat de Girona

Doctoral Thesis

DEVELOPMENT OF EFFICIENT NUMERICAL MODELS FOR THE SIMULATION OF LOW VELOCITY IMPACT AND COMPRESSION AFTER IMPACT ON COMPOSITE STRUCTURES

by

Albert Soto Masip

2018

Universitat de Girona

Doctoral Thesis

DEVELOPMENT OF EFFICIENT NUMERICAL MODELS FOR THE SIMULATION OF LOW VELOCITY IMPACT AND COMPRESSION AFTER IMPACT ON COMPOSITE STRUCTURES

by
Albert Soto Masip

2018

Doctoral Programme in Technology

supervised by
Dr. Emilio Vicente González Juan and Dr. Pere Maimí Vert

Thesis submitted to the University of Girona for the degree of Doctor of Philosophy

Acknowledgments

The work presented in this Ph.D. thesis was conducted in the AMADE research group (Department of Mechanical Engineering and Industrial Construction, University of Girona, Spain). The thesis was carried out under the grant BES-2014-070374 from the Spanish *Ministerio de Economía, Industria y Competitividad* within the FPI program and partially funded by the contract MAT2013-46749-R. Part of the research presented in this thesis was developed during the Ph.D. candidate's stay at the *Faculdade de Engenharia da Universidade do Porto* (Porto, Portugal), which was funded by the Spanish *Ministerio de Economía, Industria y Competitividad* under the mobility grant EEBB-I-16-11715.

First of all, I would like to thank my advisor's Dr. Emilio González and Dr. Pere Maimí for their guidance, support and patience throughout the thesis. Their thoughts and perspective have been the cornerstones of the thesis content. During my Ph.D. stay at the University of Porto, I visited Pr. Pedro Camanho and his research group. I would like to thank their hospitality and support. I learnt a lot from their expertise on composite modeling and the mechanics of thin ply composite laminates. I would also like to thank Paulo Pasquali from EMBRAER Composites R+D (São José dos Campos, Brazil). His help and his time have enriched the content of the thesis.

I could not miss acknowledging the support from AMADE research group in everything I needed during these years and for giving me the chance to participate in different research projects. I could not miss either to thank my colleagues from AMADE for making such a friendly working atmosphere.

Finally, my deepest gratitude goes to my family for their unconditional support and love. Especially, I would like to thank the support and understanding from Raquel.

Publications

Listed below are the papers derived during the development of the thesis:

Peer-reviewed journal articles

- A. Soto, E. V. González, P. Maimí, A. Turon, J. R. Sainz de Aja, F. M. de la Escalera, Cohesive zone length of orthotropic materials undergoing delamination, *Engineering Fracture Mechanics*, Volume 159, 2016, Pages 174-188, doi.org/10.1016/j.engfracmech.2016.03.033, ISSN 0013-7944.

- A. Soto, E. V. González, P. Maimí, F. Martín de la Escalera, J. R. Sainz de Aja, E. Alvarez, Low velocity impact and compression after impact simulation of thin ply laminates. *Composites Part A: Applied Science and Manufacturing*, Volume 109, 2018, Pages 413-427, doi.org/10.1016/j.compositesa.2018.03.017, ISSN 1359-835X.

- A. Soto, E. V. González, P. Maimí, J. A. Mayugo, P. R. Pasquali, P. P. Camanho, A methodology to simulate low velocity impact and compression after impact in large composite stiffened panels. *Submitted*.

Other publications that have been derived from this thesis but from which their content is not included in this document are listed below:

- E.V. González, P. Maimí, E. Martín-Santos, A. Soto, P. Cruz, F. Martín de la Escalera, J.R. Sainz de Aja. Simulating drop-weight impact and compression after impact tests on composite laminates using conventional shell finite elements. *International Journal of Solid and Structures*, Volume 144-145, 2018, Pages 230-247, doi.org/10.1016/j.ijsolstr.2018.05.005, ISSN 0020-7683.

Book chapters

- A. Turon, P. P. Camanho, A. Soto and E. V. González, 8.8 Analysis of Delamination Damage in Composite Structures Using Cohesive Elements, *Comprehensive Composite Materials II*, Elsevier, Oxford, 2018, Pages 136-156, doi.org/10.1016/B978-0-12-803581-8.10059-1, ISBN 9780081005347.

Conference proceedings

- A. Soto, E. V. González, P. Maimí, A. Turon. Length of the cohesive zone in orthotropic materials under pure fracture modes. *9th European Solid Mechanics Conference*. Madrid, 6 - 10 July 2015.
- E. V. González, A. Soto, P. Maimí, J. R. Sainz de Aja, J. M. de la Escalera, R. Olsson, E. Alvarez. Low velocity impact and compression after impact response of thin ply based composite laminates. *20th International Conference on Composite Materials*. Copenhagen, 19 - 24 July 2015.
- A. Soto, E. V. González, P. Maimí, J. R. Sainz de Aja, J. M. de la Escalera. Low velocity impact and compression after impact simulation of thin ply laminates. *17th European Conference on composite materials*. Munich, 26 - 30 June 2016.
- A. Soto, E. V. González, P. Maimí. Low velocity impact and compression after impact: Modelling guidelines. *SAMPE Europe Conference*. Liège, 13 - 15 September 2016.

Universitat de Girona

Dr. Emilio Vicente González Juan, Lecturer Prof. at University of Girona, and Dr. Pere Maimí Vert, Assoc. Prof. at University of Girona

hereby CERTIFY that:

The thesis entitled *Development of efficient numerical models for the simulation of low velocity impact and compression after impact on composite structures*, submitted for the degree of Doctor of Philosophy by Albert Soto Masip, has been conducted under our supervision and fulfills the requirements for the *International Doctorate*.

Emilio Vicente González Juan
Lecturer Prof. at University of Girona

Pere Maimí Vert
Assoc Prof. at University of Girona

Girona, June 2018

List of Figures

List of Tables

Acronyms

PMC	Polymer Matrix Composites
MMC	Metal Matrix Composites
CMC	Ceramic Matrix Composites
UD	Unidirectional
AFP	Automatic Fiber Placement
FRP	Fiber Reinforced Polymers
LVI	Low Velocity Impact
BVID	Barely Visible Impact Damage
CAI	Compression After Impact
VID	Visible Impact Damage
FEA	Finite Element Analysis
FEM	Finite Element Method
CDM	Continuum Damage Mechanics
CZM	Cohesive Zone Model
STI	Stable Time Increment
WWFE	World Wide Failure Exercise
FPZ	Failure Process Zone
COD	Crack Opening Displacements
CZL	Cohesive Zone Length
ENF	End Notched Flexural
LEFM	Linear Elastic Fracture Mechanics
DCB	Double Cantilever Beam
C-ELS	Calibrated End Load Split
MMB	Mixed Mode Bending
CFRP	Carbon Fiber Reinforced Polymer
R3D4	Abaqus rigid element
SFM	Abaqus surface elements
S4R	Abaqus conventional shell element with reduced integration
COH3D8	Abaqus cohesive elements
SC8R	Abaqus continuum shell with reduced integration
C3D8R	Abaqus solid element with reduced integration
CT	Compact Tension
CC	Compact Compression
RTM	Resin Transfer Molding
B-K	Benzeggagh and Kenane

Contents

Abstract

Fiber reinforced composite materials are nowadays used in several industrial applications that pursue structural weight reduction to reduce fuel consumption. The stiffness-to-weight and strength-to-weight ratios of composite materials made them an excellent choice for aerospace applications. However, impact loads is one of the major design concerns of aeronautical structures made by laminate composite materials. It is especially the case of Low Velocity Impact (LVI) events that despite leading to barely visible impact damage can significantly reduce the mechanical performance of composite structures. Reliable numerical models can help in reducing the actual amount of physical tests that are time-consuming and costly. Nevertheless, impact simulations are computationally intensive and their application in large composite structures is limited. Furthermore, the numerical models require many parameters that affect their efficiency, accuracy, objectivity and robustness. The present thesis aims to define a clear and efficient methodology to build reliable numerical models for the LVI and Compression After Impact (CAI) simulation of composite structures that can be applied in challenging applications of scientific and industrial interest.

Firstly, the present work describes a methodology to simulate LVI and CAI on composite laminates that is validated experimentally at the coupon level. The key definitions are discussed and especial attention is devoted to the definitions that affect the computational efficiency. Novel formulas, which are useful for optimum mesh discretization, are proposed to predict the cohesive zone length of composites undergoing delamination under pure fracture modes. A numerical benchmark of different finite element types and interaction technologies commonly used in the literature is performed to compare their computational performance and accuracy. Furthermore, criteria to efficiently define cohesive numerical parameters are proposed.

Numerical simulations can help in the understanding of the damage sequence of polymer based composite laminates during an impact event, which can be a difficult task to perform experimentally when dealing with a large number of plies. The proposed methodology is applied to predict the LVI and CAI of thin ply fabric laminates, which is a computationally challenging case due the large number of plies and interfaces involved. The numerical results indicate that matrix cracking effects can be assumed negligible for the

studied thin ply laminate while delamination and especially the fiber traction separation law shape are important for accurate predictions.

Finally, the methodology is applied for the prediction of relatively large composite sub-components with the aim to show that the proposed methodology enables analyses at larger scales. It is demonstrated the potential of the methodology and employed techniques to address problems of industrial interest such as the strength prediction of both undamaged and damaged stiffened panels.

Resum

Els materials compòsits són actualment utilitzats en diferents sectors industrials que busquen la reducció de pes estructural amb la finalitat de reduir el consum de combustible. La rigidesa i resistència que ofereixen en relació amb el seu pes els ha convertit en una excel·lent opció per aplicacions aeronàutiques. No obstant això, les càrregues a impacte són una de les principals preocupacions en el disseny d'estructures aeronàutiques fabricades amb laminats de material compòsit. És especialment el cas d'impactes a baixa velocitat que deixen dany difícil de detectar durant inspeccions visuals però que poden reduir significativament la resistència de l'estructura. L'ús de models numèrics fiables pot ajudar a reduir l'actual nombre d'assaigs experimentals que són costosos tant en temps com econòmicament. Tanmateix, l'aplicació de models numèrics en estructures de material compòsit de gran dimensió es veu limitada pel cost computacional que representen. A més, els models numèrics requereixen moltes definicions que afecten la seva eficiència, precisió, objectivitat i robustesa. La present tesi té com a objectiu desenvolupar una metodologia clara i eficient per realitzar prediccions fidedignes d'impacte a baixa velocitat i compressió després d'impacte en estructures de material compòsit que pugui ser aplicada en casos de rellevància científica i industrial.

En primer lloc, es descriu una metodologia per a la simulació d'impacte a baixa velocitat i compressió després d'impacte en laminats de compòsit la qual és validada experimentalment a escala de proveta de laboratori. Les definicions més importants es discuteixen i es té especial atenció en aquelles que afecta l'eficiència computacional. Per una òptima discretització del model és desitjable conèixer la longitud de zona cohesiva. Noves fórmules per predir la longitud de zona cohesiva en delaminació es proposen per modes purs de fractura. Es realitza un estudi numèric comparatiu de diferents tecnologies d'element finit i d'interacció cohesiva típicament utilitzades en la literatura amb la finalitat de comparar la seva precisió i eficiència computacional. A més, es proposen criteris per definir paràmetres numèrics del model cohesiu que afecten el temps computacional.

Els models numèrics poden ajudar a entendre la seqüència de dany durant esdeveniments d'impacte, els quals poden ser complicats d'analitzar experimentalment. La metodologia proposada s'aplica per predir la resposta

a impacte i compressió després d'impacte en laminats de capes primes. És un cas que representa un repte computacional per l'elevat nombre de capes i interfases involucrades. Els resultats numèrics contrastats experimentalment indiquen que els efectes de trencament de matriu es poden obviar mentre que la delaminació i especialment la forma de la llei cohesiva de la fibra són de gran importància en les prediccions de laminats de capes primes.

Finalment, la metodologia s'aplica per la predicció de sub-components rigiditzats de material compòsit amb la finalitat de mostrar que la metodologia permet anàlisis a escales majors. Es demostra el potencial de la metodologia i tècniques utilitzades per adreçar problemes d'interès industrial com és la predicció de la resistència d'un panell rigiditzat abans i després de ser danyat per un eventual impacte.

Resumen

La aplicación de materiales compuestos se puede encontrar actualmente en distintos sectores industriales que buscan la reducción de peso estructural con la finalidad de reducir el consumo de combustible. La rigidez y resistencia que ofrecen con relación a su peso les hace una excelente opción para aplicaciones aeronáuticas. No obstante, las cargas a impacto es uno de los casos de mayor preocupación para el diseño de estructuras aeronáuticas de material compuesto. Este es especialmente el caso de impacto a baja velocidad que induce un daño difícil de detectar durante inspecciones visuales pero que puede reducir significativamente la resistencia mecánica en estructuras de material compuesto. El uso de modelos numéricos fiables puede ayudar a reducir la actual cantidad de ensayos experimentales que son costosos tanto en tiempo como económicamente. Sin embargo, la aplicación de modelos numéricos a estructuras de material compuesto de gran tamaño se ve limitada por su coste computacional. Además, los modelos requieren muchas definiciones que afectan a su eficiencia, precisión, objetividad y robustez. La presente tesis tiene como objetivo desarrollar una metodología clara y eficiente para realizar predicciones fiables de impacto a baja velocidad y compresión después de impacto en estructuras de material compuesto que pueda ser aplicada a casos de relevancia científica e industrial.

En primer lugar, se describe una metodología para la simulación de impacto a baja velocidad y la compresión después de impacto en laminados de material compuesto la cual se valida experimentalmente a escala de probeta. Las definiciones más importantes se discuten y se presta especial atención a las definiciones que comprometen la eficiencia computacional. Para una óptima discretización del modelo es deseable conocer la longitud de zona cohesiva. Nuevas fórmulas para predecir la longitud de zona cohesiva en deslaminación se proponen por modos puros de fractura. Se realiza un estudio numérico comparativo de distintas tecnologías de elemento finito e interacción cohesiva comúnmente utilizadas en la literatura para comparar su precisión y eficiencia computacional. Además, se proponen criterios para definir parámetros numéricos del modelo cohesivo que afectan al tiempo computacional.

Los modelos numéricos pueden ser utilizados para entender la secuencia de daño en el material durante eventos de impacto, los cuales son difíciles de

analizar experimentalmente. La metodología propuesta es aplicada para predecir la respuesta a impacto y compresión después de impacto de laminados de lámina delgada. Es un caso que representa un reto computacional debido al elevado número de láminas e interfaces que contienen este tipo de laminados. Los resultados numéricos contrastados experimentalmente indican que el efecto de rotura de matriz es insignificante mientras que la deslaminación así como la forma de la ley cohesiva de la fibra resultan de vital importancia para las predicciones de laminados de lámina delgada.

Finalmente, la metodología es aplicada para la predicción de sub-componentes rigidizados de material compuesto con la finalidad de mostrar que la metodología permite análisis a escalas superiores. Se demuestra el potencial de la metodología y técnicas empleadas para problemas de interés industrial como es la predicción de la resistencia de sub-componentes de material compuesto antes y después de ser dañados por un impacto.

Part I

Introduction and Literature Review

Chapter 1

Introduction

1.1 Background

A composite material can be defined as the result of merging two or more different materials. Wood, rocks or shells are examples of composite materials found in the nature but there exist man-made composite materials such as paper, bricks or concrete. More recent man-made composite materials are those made by glass or carbon fibers embedded within a polymeric matrix. Composites aims to merge different materials that combined offer better performance that their constituents acting independently.

Composite materials can be classified depending on the matrix material or the reinforcement type. Polymer Matrix Composites (PMC) (e.g. thermoplastics or thermosets), Metal Matrix Composites (MMC), and Ceramic Matrix Composites (CMC) are the most common matrix types. The reinforcement can be in the form of continuous fibers, discontinuous fibers, or particles as shown in Fig. 1.1.

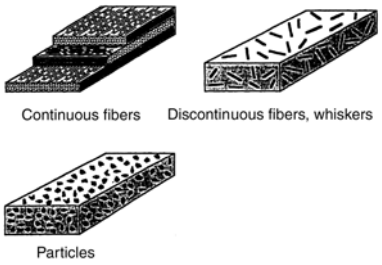

Fig. 1.1: Composite reinforcement forms (source: Zweben [94]).

The reinforcement can present different fiber architectures as shown in Fig. 1.2 depending on the design requirements or the manufacturing pro-

cess. On the one hand, discontinuous fibers or also called short fiber reinforcements are typically randomly distributed or oriented according to the manufacturing process (e.g. injection molding process). On the other hand, continuous fiber reinforcements are commercially available in the form of unidirectional (UD) tapes or forming woven fabrics (also 3-D textiles) with different weave features possibilities. The fabric fabrication is done by weaving, braiding, knitting, stitching, and by using non-woven techniques. Continuous fiber reinforcements are usually employed in the form of laminates. A laminate consists of more than one layer, which is also called ply or lamina, stacked over each together. The orientation of each ply can be different according to mechanical design requirements. In fact, there exists manufacturing systems such as Automatic Fiber Placement (AFP) that allows to change the fiber orientation point-to-point.

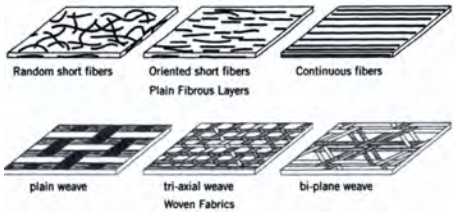

Fig. 1.2: Fiber arrangement patterns at the lamina level (source: Gürdal et al. [71]).

Fiber Reinforced Polymers (FRP) composite materials (e.g. carbon/epoxy, kevlar/epoxy) have outstanding specific stiffness and strength properties, corrosion resistance and fatigue performance. Furthermore, the ability to mold composite materials into complicated shapes more easily that most other materials allows more freedom to designers and engineers. These factors allow building structures with significant savings in terms of maintenance and weight. Applications of FRP is found in several fields such as wind energy, sport goods, civil engineering, car and marine industry. However, it is the aerospace industry, including military and commercial aircraft, the largest consumer of FRP composite materials [43] in an effort to reduce green house gas emissions and fuel costs, which are the largest operating expense for airlines. Nowadays, composite materials have been introduced in primary structure components in the most recent long range air-planes as shown in Fig. 1.3 and reported by Jerome [85].

Composite materials are generally tailored to work under in-plane loads. Impact events are one of the most critical loads for composite structures because different damage mechanisms might take place even for low impact energies. Vaidya and Uday [162] categorized the impact response of materials into hyper velocity impact, high velocity impact or ballistic impact, intermediate velocity impact, and low velocity impact regimes. Hyper ve-

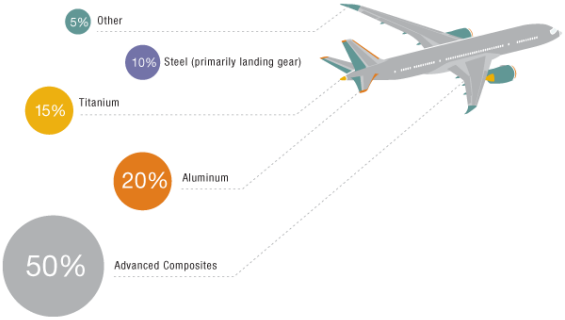

Fig. 1.3: Materials used in the body of Boeing 787 (source: [168]).

locity impact occurs for velocities larger than 1000 m/s. The target material behaves like a fluid. This type of impact occurs in the context of micrometeorites protection. High velocity impact ranges from 50 m/s to 1000 m/s. It is usually the result of arms fire or explosive warhead fragments but also due to bird strikes. This impact type leads to localized damage. The boundary condition effects can be ignored because the structure does not have time to respond. Intermediate velocity impact occur at velocities in the range from 10 m/s to 50 m/s which are related to foreign object debris on roads and runaways. Low Velocity Impact (LVI) occur at velocities below 10 m/s which are commonly related to tool drops. It is generally accepted that LVI can be treated as a quasi-static event [145, 148, 171]. Global plate motion occurs and the dynamic structural response of the target is important because it can absorb energy elastically. Sometimes high-velocity impact is associated to a small mass of the impactor while LVI to a large mass impactor. However, Olsson [114] and Christoforou and Yigit [42] demonstrate that the response under elastic conditions depends on the impactor mass, the mass of the impacted plate and the structural stiffness.

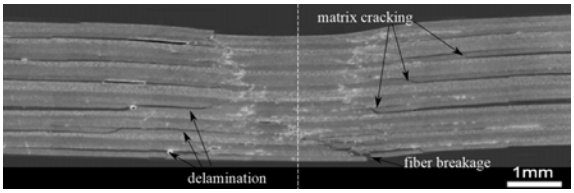

Fig. 1.4: SEM micrograph of a specimen cross section after a 3.9 mm indentation [163]. The specimen was cut along the 90º direction. The dashed white line represents the center of the indentation.

Fig. 1.4 shows the three most commonly observed types of impact-

induced damage in carbon/epoxy composite laminates: matrix cracking, fiber breakage and delaminations. The micrograph is taken from an indentation test [163]. Quasi-static indentation tests are often used to obtain experimental evidence of the damage sequence occurred during a LVI test.

Laminated composites can easily undergo Barely Visible Impact Damage (BVID) under transverse loads such as LVI. BVID is associated with impact events where delamination is the main damage mechanism with almost no indentation. Delaminations are a major threat in composite laminates because they are hidden and reduce significantly the compressive strength of an impacted structure. BVID is mainly associated to damage in the form of delaminations while in Visible Impact Damage (VID) matrix cracking and fiber failure are also present and the damage is are visible in both faces as sketched in Fig. 1.5.

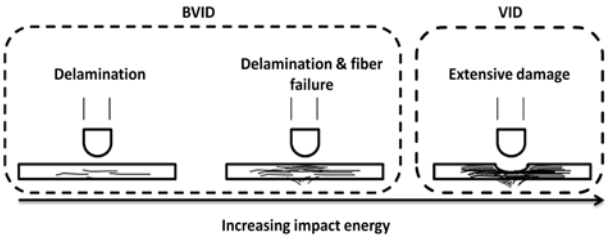

Fig. 1.5: Sketch of damage mechanisms associated to BVID and VID (source: [29]).

In conventional composite laminates, matrix cracking is usually the first damage mechanism to appear due to intralaminar shear and tension stresses and often trigger delamination [163]. Delaminations are prone to propagate under in-plane loading. Fibre, matrix cracking and delaminations reduce the residual strength of a structural component and decrease its buckling load limit. Fig. 1.6 sketches the type of damage and the effect on the compression strength after impact as a function of the impact energy. For this reason, it is of paramount importance the structural behaviour of a component under compression load during the design process.

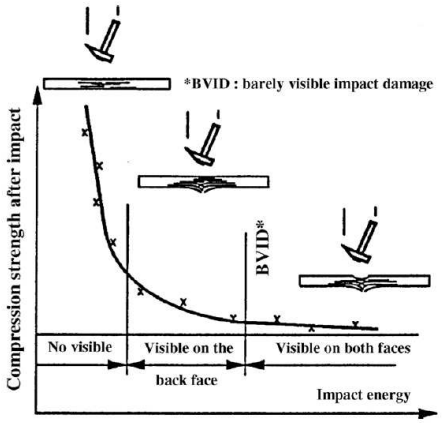

Fig. 1.6: Sketch of the induced damage and the compression strength after impact as a function of the impact energy (source: [128]).

1.2 Motivation

The use of composite laminates in structural applications has become a reality during the last years within the commercial aeronautical industry. Weight reduction is a cornerstone to reduce fuel consumption and CO_2 emissions. Nevertheless, LVI events are a major concern during the design of aerospace structures made of composite laminates because they can leave the structure with BVID. BVID is difficult to detect by visual inspection while the mechanical performance can be significantly reduced due to the presence of hidden delaminations. This is especially the case under compression loading in which existent delamination reduce the buckling load. Delaminations can open (i.e. buckling of sub-laminates) under compression loading and then allowing the damage to propagate from the initial state until the subsequent failure of the structure. Thus, it is of interest to assess the damage tolerance of the impacted composite laminate, which is usually done through the Compression After Impact (CAI) test [17]. Fig. 1.7 sketches different buckling modes that can occur during the CAI test. It is worth noting that LVI can reduce the CAI strength as much as 60% in a typical aerospace fibre-resin system [74].

The certification of new materials in aerospace applications involves extensive experimental campaigns that are time-consuming and costly. The building block approach [81] is followed to gain understanding and to minimize the amount of large scale tests. At each step of the building block approach, experimental tests and analysis techniques are combined because it would be infeasible to test all loading and environmental scenarios [44]. Thus, reliable analysis techniques can help in reducing the actual amount of

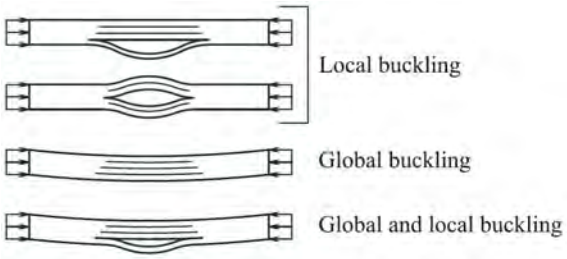

Fig. 1.7: Buckling modes of delaminated plates under compression loading (source: [47]).

physical tests. For this reason, modeling impact events has been the focus of many researchers over the years.

The resulting damage from an LVI depends on the impactor features (e.g. material, shape, mass, velocity), the composite structure features (e.g. material, geometry, boundary conditions) as well as the environmental conditions. The prediction of CAI strength depends on the composite structure features, and especially on the damage occurred during the impact event. Modeling LVI and CAI events have been treated either analytically or by means of numerical methods in the literature.

Analytic impact models are a powerful tool for their conceptual framework that provides a fast assessment on the type of damage. Some relevant contributions are the work from Abrate [4] and Olsson [115, 118, 119]. However, impact analytical models are usually restricted to the elastic regime and specific geometries. The interaction among damage mechanisms and their progression is difficult to be considered. For damage tolerance assessments such as the CAI, an initial damage has to be assumed to predict analytically the residual strength [111, 169] what limits their predictive capability.

Virtual testing by means of non-linear Finite Element Analysis (FEA) is an alternative that can tackle the complexity of the physical phenomena - geometric and material non-linearities, dynamic structural behavior and loading, contact - without any restriction in terms of geometry and boundary conditions. The stress field takes into account the interaction among damage mechanisms and their damage progression. In addition, the impacted model can be used for the damage tolerance analysis sequentially without assuming any initial damage.

However, virtual testing is computationally intensive which limits its application to structural components. The advent of new materials such as thin ply laminates represent a computational challenge for the large number of plies and interfaces involved. Furthermore, virtual testing requires many parameters that can affect the model efficiency, objectivity and robustness, which sometimes are not clearly reported in the literature.

1.3 Objectives

The present thesis aims to present a clear and efficient methodology to build reliable numerical models for the LVI and CAI simulation that can be applied in challenging applications of scientific and industrial interest in the field of composite structures. In essence, a methodology that enables analyses at larger scales than the coupon-level.

To achieve this main goal, the specific objectives of the thesis are, firstly to provide a methodology that defines the key parameters to feed the numerical models in order to make them reliable and efficient with the current state-of-the-art numerical tools and material models. Secondly, to validate the methodology with experimental data. Finally, to use the methodology for applications of scientific and industrial interest such as the LVI and CAI on thin ply laminates and aircraft composite stiffened panels.

1.4 Thesis lay-out

The thesis is structured in four parts. The first part includes an introduction and a literature review of the topic. The second part describes the methodology used throughout the thesis while the third part presents two cases in which the methodology described in the second part is applied and validated. Finally, the fourth part concludes with an assessment of the achievements made and suggestions for future work.

More specifically, Chapter 2 reviews the numerical investigations dealing with LVI and CAI from the literature. The existent techniques and approaches to model impact as well as the required definitions to set-up the models (e.g. finite element discretization, material models) are reported concisely. The literature review is not restricted to LVI at the coupon level for standard plies. It also covers numerical studies dealing with composite structures.

The finite element discretization is an important aspect to correctly dissipate the energy of the model. In Chapter 3, the range of applicability of the existent analytical formula to predict the cohesive zone length for material undergoing delamination is studied and new formula are proposed.

Chapter 4 presents a methodology to simulate LVI and CAI on composite laminates, which pays special attention to definitions related to model accuracy, objectivity, efficiency and robustness. A numerical benchmark is performed at the coupon level, which is supported with experimental data, to compare different modeling strategies in terms of computational performance and accuracy.

The methodology from Chapter 4 is applied in Chapters 5 and 6. The results of both Chapters are compared with experimental data. Chapter

5 presents the LVI and the CAI simulation results of thin ply weave laminates, which represents a computational achievement due to the large number of plies and interfaces involved. The numerical results provide understanding on the governing damage mechanisms of thin ply laminates during LVI events and highlight the importance of the fiber traction separation law. Chapter 6 presents novel results of LVI and the sequential CAI tests on large composite stiffened panels.

Finally, the thesis is concluded in Chapter 7 with overall concluding remarks and Chapter 8 discusses suggestions for future work.

Chapter 2

Literature review

The increase of computing power during the last decade allowed reasearchers to perform numerical investigations to better understand and predict the LVI and CAI of composite laminates. However, they are still computationally expensive. For this reason, most numerical investigations in the literature address LVI and CAI predictions at the coupon-level and their use at larger scales is still limited. This chapter aims to provide perspective for improvements on the existent techniques and modeling methodologies used in the literature for the simulation of LVI and CAI of composite laminates, paying special attention towards the computational efficiency.

2.1 LVI and CAI numerical modeling

Several investigations [2, 32, 45, 53, 61, 65, 67, 80, 86, 98, 99, 109, 126, 132, 136, 154] agree with using the Finite Element Method (FEM) to model the meso-scale of composite laminates to predict the LVI and CAI at the coupon level.

Within the FEM framework, impact numerical models can be classified as strength based models [78, 100], fracture mechanics based models [96] or Continuum Damage Mechanics (CDM) based models.

Strength based impact models [78, 100] allow to accurately predict the damage initiation during an impact event if appropriate failure criteria are used. The limitation of strength based numerical models is that they cannot account for damage propagation unless the elements are deleted or mechanical properties are knocked down once reached certain failure criteria. However, if this is done without any mesh regularization procedure the energy dissipated depends on the element size [26, 113]. As a consequence, the model becomes mesh dependent and the damage progression as well as the dissipated energy is not objective.

However, impact involves dissipation of energy through different damage

mechanisms. Thus, fracture mechanics based impact models [96] can take into account the material fracture toughness and the damage progression. However, this type of analyses might require to have an initial crack.

CDM based models have proved their suitability in several studies for the prediction of LVI [32, 53, 61, 77, 98, 99, 132], and LVI with the sequential CAI tests [2, 3, 36, 45, 65, 67, 109, 126, 136, 154] of composite laminates at the coupon level.

The CDM framework [92, 123] combines failure criteria to predict damage initiation with fracture mechanics to predict damage progression through coupling internal damage variables, which represent each damage mechanism. Different continuum finite element types can be used depending on the desired detail of the stress state. Most LVI studies [2, 3, 32, 36, 45, 61, 65, 67, 77, 86, 98, 99, 109, 126, 136, 154] support the use of CDM in combination with the Cohesive Zone Model (CZM) as frameworks to model intralaminar and interlaminar damage, respectively. The CZM is widely used to model delamination which can be used by means of cohesive elements or cohesive surfaces.

Impact involves geometric and material non-linearities, contact, dynamic structural behaviour and loading. For this reason, explicit schemes are generally used in the literature for LVI and CAI simulations [2, 32, 45, 53, 61, 65, 67, 80, 86, 98, 99, 109, 126, 132, 136, 154] to avoid some of the numerical difficulties from implicit solvers.

Explicit dynamics procedure solves the boundary - value problem as a wave propagation problem. A bounded solution is obtained when the simulation time increment ($\triangle t$) is below the Stable Time Increment (STI), which is a stability limit; the minimum time that a dilatation wave takes to move across any element of the model.

The STI of a continuum finite element ($\triangle t_{elem}$) or a finite thickness cohesive element is given by:

$$\triangle t_{elem} \leq l^* \alpha \sqrt{\frac{\rho}{E}} \tag{2.1}$$

where ρ is the material density, E the maximum component of the constitutive tensor, and $\alpha = \sqrt{1+\zeta^2} - \zeta$ with ζ being the fraction of critical damping that prevent finite elements from ringing or even collapsing in the highest element frequency [1]. l^* is the characteristic element length, which is related to the shortest finite element edge.

The STI of a cohesive element (i.e. zero-thickness) or cohesive surface ($\triangle t_{int}^{coh}$) is:

$$\triangle t_{int}^{coh} \leq \sqrt{\frac{\bar{\rho}}{K_{coh}}} \tag{2.2}$$

where $\bar{\rho}$ and K_{coh} are the surface density and the penalty stiffness from the cohesive element or cohesive surface, respectively.

In case of using the contact penalty method, the STI due to contact ($\triangle t_{int}^{con}$) is controlled by:

$$\triangle t_{int}^{con} \leq \sqrt{\frac{\rho h_{elem}}{K_n}} \tag{2.3}$$

where ρ is the material density, h_{elem} the element thickness where contact occurs and K_n the normal contact penalty stiffness.

The computational time of an explicit simulation is governed by the STI; $\triangle t_{min} = \min(\triangle t_{elem}, \triangle t_{int}^{coh}, \triangle t_{int}^{con})$. Therefore, special attention on the minimum element size of the model must be paid because even if it is a single finite element with a smaller size than the remaining elements from the model, it will control the model STI. This is one of the reasons why most LVI studies that use an explicit approach employ structured meshes.

The main definitions needed for an impact numerical model are: the intralaminar damage model, the interlamimar damage model, the modeling strategy, the finite element discretization, and the element deletion criterion. These definitions involve several parameters that affect the model robustness, efficiency, accuracy and objectivity, which sometimes are not clearly reported in the literature.

2.1.1 Intralaminar damage model

There are several numerical studies on LVI predictions of composite laminates in which different CDM models are used to model the intralaminar damage [53, 80, 87, 95, 101, 102, 106, 108, 132, 154, 167]. The main differences among them are: three-dimensional or plane stress conditions; in-plane shear loading behaviour; the mesh regularization algorithm used to address strain - softening; and especially the damage initiation and the damage propagation criteria.

Impact models assuming plane stress conditions [61,67,80,86,131,142,166] or three dimensional conditions [2, 7, 45, 53, 59, 65, 87, 98, 99, 126, 132, 154] are used in the literature depending on the desired compromise among computational effort and detailed analysis. Out-of-plane damage mechanisms are neglected under plane stress conditions.

Plasticity under in-plane shear loading is generally considered [7,53,59,61, 80,86] even though there are some authors that neglects it [65,98,99,132,166].

The crack band model [26] is widely used to deal with strain localization. Tan et al. [154] calculates the characteristic element length more accurately by considering the actual fracture plane in the finite element. Donadon et al. [53] extended to 3-D the solution proposed from Oliver et al. [113] to overcome some of the crack band model limitations.

Generally, rate-dependency is neglected in LVI numerical models [2,3,32, 36,45,53,61,65,67,86,98,99,109,126,132,136,154]. However, Williams and Vaziri

[166] and Iannucci et al. [80] considered strain-rate effects in the CDM. It is generally accepted that in LVI the velocity is low enough to assume a static response of the structure [145,148,171]. Furthermore, carbon fiber composites are considered rate-independent in fiber-dominated modes, but glass and Kevlar do show rate stiffening and strengthening [72]. However, matrix-dominated modes are rate-dependent [79] but it depends on the matrix type. Generally, thermoset resins are less rate-dependent than thermoplastic resins.

Some impact models use simplified damage initiation criteria (e.g. maximum strain or stress) [80,87,166,167] while others use more physically based approaches [53, 65, 98, 99, 132, 154]. The main differences among them are in the definition of the fiber compression and the matrix compression strength. Initiatives like the World Wide Failure Exercise (WWFE) organized by Hinton et al. [76] assess and review the predictive capability of some established failure theories from the literature.

The damage evolution is usually represented by linear or quasi-exponential strain - softening laws [53,59,61,65,80,98,99,132,142,154]. However, it is worth mentioning that some studies [50,121,122] highlight the importance of the damage evolution because multiple damage mechanisms occur during the fracture of a composite laminate (e.g. fiber-bridging, fiber pull-outs), which are actually embedded within the traction separation law shape at the macro-scale level.

Standard test methods are available to measure the majority of the independent ply material properties needed for the definition of damage models defined at the ply-level. Ply elastic and strength properties can be obtained according to American Society for Testing Materials (ASTM) for tensile [18], compression [15] and shear loading [19, 20]. The tensile and shear matrix fracture toughness can be obtained according to [21] and [83, 105], respectively. The matrix compression fracture toughness is dependent on the shear matrix fracture toughness and on the fracture angle [101, 102]. There is no standard for measuring the fiber fracture toughness. However, there exist proposed procedures in the literature [37, 129]. The same occurs to measure the traction separation law associated to fiber damage [121, 122].

2.1.2 Interlaminar damage model

The CZM was introduced in the early sixties by Barenblatt [62] and Dugdale [55] to model different non-linear processes while avoiding the stress singularity at the front of an existing crack. Barenblatt focused on brittle fracture while Dugdale focused on plastic fracture. The CZM assumes that the entire Failure Process Zone (FPZ) is lumped into the crack plane. This assumption makes the CZM very efficient in situations that the crack path is known beforehand. As a consequence, the CZM is generally used to model delamination which can be used by means of cohesive elements or cohesive

surfaces.

The CZM concept is sketched in Fig. 2.1. The CZM represents the FPZ (damaged material) through a fictitious crack (dashed line) able to transfer cohesive forces from one face to another. These forces are given by the so-called cohesive law (see Fig. 2.7), which relates them with the Crack Opening Displacements (COD). The area underlying area is the facture energy. There exist standard procedures to obtain the interlaminar fracture energy [21, 22, 83]. The Cohesive Zone Length (CZL) is the distance at the crack plane where the cohesive forces are acting.

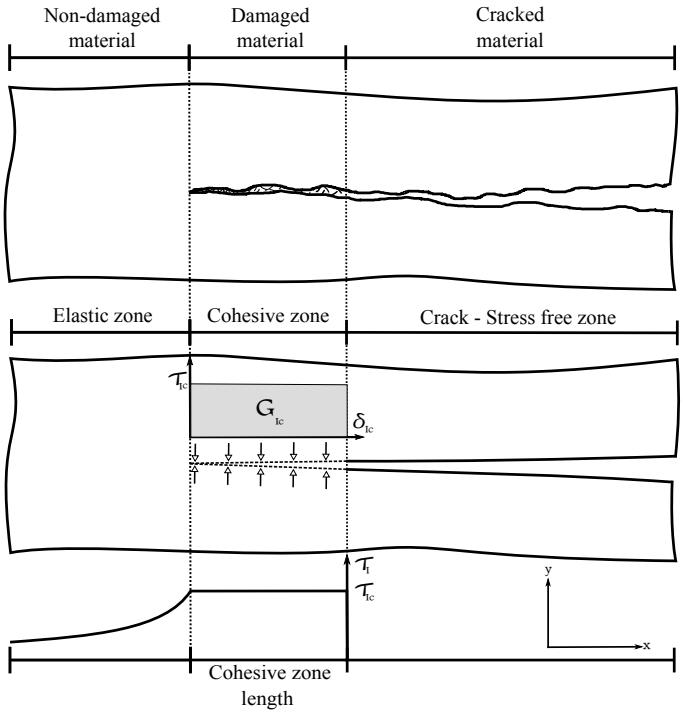

Fig. 2.1: FPZ of a quasi-brittle material (top), CZM concept (middle) and stress distribution along the crack path for a constant cohesive law under pure mode I loading (bottom).

The main differences among interlaminar CZM's from the literature are the initiation and propagation criteria under mixed mode conditions as well as the cohesive law shape considered, which controls the damage evolution.

Orifici et al. [120] reviewed the existent formulations to model delamination based on the CZM approach. Maximum stress criterion [86] or quadratic nominal stress criterion [59,61,87,134,136,142,154] are generally used. Turon et al. [155] proposed a thermodynamically consistent damage model in which the damage initiation criteria is formulated according to the damage propagation (i.e. Benzeggagh and Kenane criterion [27]). Some LVI studies [65,98]

use a CZM [66] based on it. However, failure criteria that predict delamination initiation under mixed-mode conditions have not been fully validated due to the lack of experimental data [155].

A power law criterion is used for mixed-mode fracture propagation [61,80, 86, 87, 134]. Some authors assume a linear coupling between fracture modes [77,136], while others [59,65,98,99] use the Benzeggagh-Kenane criterion [27]. Camanho et al. [33] argues that Benzeggagh-Kenane criterion [27] is a suitable criterion for the critical energy release rate under mixed-mode ratio in epoxy and PEEK composites.

Most impact models assume a cohesive law with linear softening [59, 61, 77, 87, 134, 136, 142, 154] and some with an exponential one [77, 136]. Linear softening cohesive laws has a good compromise among accuracy and computational efficiency to model delamination [5]. The FPZ in composites delamination under pure mode I is usually small unless fiber-bridging mechanisms are present. Consequently, the effect of the cohesive law shape on the structural response is negligible as Alfano reported [5]. However, it is less clear the importance of the cohesive law shape under pure mode II delamination because the FPZ is usually larger than in mode I. Dourado et al. [54] studied the importance of the cohesive law shape to predict End Notched Flexural (ENF) tests. A bi-linear law was needed for HS160REM carbon/epoxy specimens while a linear softening was used for T800H/3900-2. Catalanotti et al. [38] investigated the effect of through-thickness compressive stress and friction on mode II interlaminar fracture toughness experimentally and numerically. Linear softening together with frictional effects could predict the experimental tests of IM7/8552. There is no standard procedure to determine the interlaminar traction separation law shape. However, Sarrado et al. [138] devised an experimental procedure to obtain the cohesive law shape of composite bonded joints (i.e. epoxy adhesive). In the case of adhesive bonded joints the cohesive law shape has an impact on the structural response because the FPZ is larger than in composite delmaintion. This could be also the case in composite delamination with significant fiber-bridging.

Turon et al. [156] demonstrated that changes in the local mode ratio during the evolution of damage under mixed-mode loading might cause errors in the energy dissipation calculation. To solve this issue, it was proposed a relationship between interlaminar strengths and fracture toughness [156] and more recently a new formulation has been proposed [159].

2.1.3 Modeling strategy

As previously mentioned, there is agreement that the meso-scale provides enough detail of the stress state for LVI and CAI prediction. The plies are modeled as a homogeneous orthotropic continuum material and the interfaces between plies where delamination can potentially takes place are mod-

eled by means of cohesive interactions (e.g. cohesive elements, cohesive surfaces) as sketched in Fig. 2.2. In fact, the potential interface for delamination under impact loading only occurs between plies with different fiber orientation [64]. In LVI and CAI simulations, the CZM is commonly employed only at the interfaces between plies with mismatch angle. The interlaminar fracture toughness is obtained from standard interlaminar tests [21, 83], which use 0^o specimens. However it is known that depending on the interface mismatch angle [9,51] and the stacking sequence [133] different interlaminar fracture toughness can be obtained what is explained by the presence of more or less fiber bridging and crack migration [127].

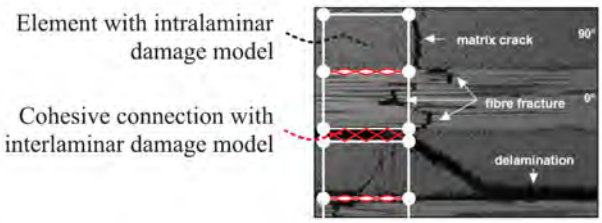

Fig. 2.2: Superposition of the finite element meso-scale model idealization with a damaged composite laminate (source: González et al. [65]).

Within the FEM, the CZM can be used by means of cohesive elements that computes the openings based on the cohesive element nodal displacements or by means of cohesive surfaces which compute the openings through a contact algorithm without requiring perfect match between upper and lower surface nodes. Depending on the cohesive interaction, different modeling strategies can be used as discussed in González et al. [65] and sketched in Fig. 2.3. The use of conforming meshes is the simplest pre-processing approach. Non-conforming meshes might be used in case of meshing each ply according to the corresponding fiber orientation to avoid mesh bias effect [63,97]. Cohesive surfaces can be used in non-conforming meshes straightforwardly while tie constraints are needed if cohesive elements are used.

Another approach, which is sketched in Fig. 2.4, is the one used by some authors [2,32,77,136,150] that model the plies according to the fiber direction with solid elements and insert cohesive elements vertically and horizontally to model matrix cracking and delamination, respectively. The discontinuity formed by matrix cracking can be well represented while the approach avoids large element distortions due to modeling matrix damage through a smear damage approach. The approach only allow conventional ply orientations (i.e. 0^o, 45^o , 90^o) due to topological reasons. The authors [2,32,77,136] use a strength based model to model matrix cracking while damage initiation and propagation criteria are considered for delamination. Sun and Hallett [150] used damage initiation and propagation criteria for both intralaminar and

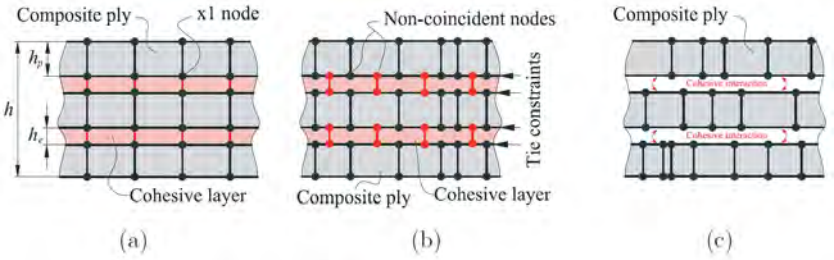

Fig. 2.3: Strategies for modeling laminate composites at the meso-scale: (a) using conforming meshes between cohesive elements and continuum elements, (b) using non-conforming meshes between cohesive elements and continuum elements by means of tie constraints, or (c) cohesive surfaces and continuum elements that allows conforming and non-conforming meshes. The variables shown are: h laminate thickness; h_e cohesive element thickness; h_p ply or sublaminate thickness (source: González et al. [65]).

interlaminar cohesive elements. This approach offers computational benefits because it makes the intralaminar constitutive model simple by only accounting for fiber breakage or even simpler if only linear elastic behaviour is considered as in [150]. Nevertheless, it is not clear the mesh discretization criterion needed to correctly capture matrix cracking. In fact, the computational benefits can be compromised if fine discretization is needed.

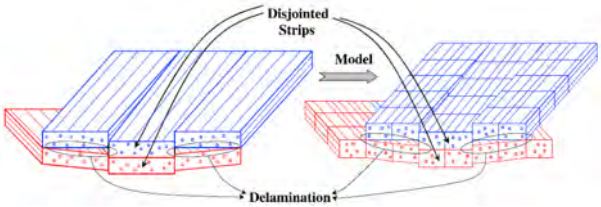

Fig. 2.4: Sketch of the meso-scale modeling approach used in [2, 32, 136, 150] (source: Bouvet et al. [32]).

Some authors [53, 80, 166] neglect modeling the effect of delamination and only consider the ply damage mechanisms to reduce the computational effort even though it generally implies a loss of accuracy. Raimondo et al. [132] proposed a constitutive model which takes into account both intralaminar and interlaminar damage mechanisms for the sake of computational efficiency. Delamination is assumed to occur at the mid-plane of each ply. Despite the approximation on the delamination kinematics, they obtained good correlation with the experimental results. Other authors only consider few interfaces for delamination [86, 87, 109]. It is worth remarking the results from Johnson et al. [86] which shows the results sensitivity to the number of interfaces for delamination considered (see Fig. 2.5). Similar results were reported by

Mendes et al. [109] who considered zero and one interface for delamination at the mid-plane of the laminate.

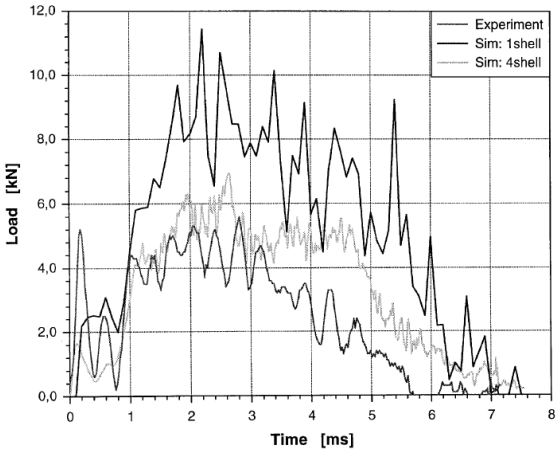

Fig. 2.5: Effect of modeling different number of interfaces for delamination (source: Johnson et al. [86]).

Different cohesive interaction technologies and finite element types are possible within the FEM to account for intralaminar and interlaminar damage, respectively.

The CZM by means of cohesive elements or cohesive contact surfaces is widely used in the literature to model delamination.

Cohesive surfaces naturally handles large displacements and non-conforming meshes. However, they are more expensive computationally than cohesive elements due to the contact tracking algorithm [99]. Zero-thickness cohesive elements [3, 32, 59, 61, 87, 142] and finite thickness cohesive elements [36, 45, 65, 98, 99, 126, 134] have been mostly used to model LVI in comparison with cohesive surfaces [67, 99, 154]. This is probably due to the fact that cohesive elements are easier to implement and develop them than cohesive surfaces. Within an explicit finite element framework, finite thickness cohesive elements detrimentally affect the element STI due to the small thickness. Different thickness are used in the literature: 0.001 mm in [36]; 0.01 mm in [65, 98, 99, 134]; 0.02 mm in [45]; 0.1 mm [126]. The STI of zero-thickness cohesive elements is governed by two numerical parameters (see Eq. (2.2)): the surface density ($\bar{\rho}$) and the penalty stiffness (K_{coh}). Both parameters affect the model efficiency and accuracy and it is not clear in the literature how they should be defined.

The penalty stiffness (K_{coh}) could be defined as the ratio of the interface elastic modulus with the interface thickness [46]. Some authors [46, 80] consider the interface thickness as one fifth of the adjacent sublaminate. Turon et

al. [158] recommended to define the penalty stiffness as $K_{coh} \geq \frac{50E_{22}}{h_p}$ to avoid affecting the compliance of the system; E_{22} is the transverse elastic moduli and h_p the adjacent sublaminate thickness. The aforementioned definitions lead to penalty stiffness values on the order of 5×10^5 - 1×10^6 N/mm^3, which are values used by other authors with satisfactory results [33,154,158]. Schwab et al. [142] chose the penalty stiffness such as the contact work is smaller than a tenth of the energy contribution of any other mechanism. Nevertheless, different values are used in the literature without a clear definition [32,59,61,87].

On the other hand, zero-thickness cohesive elements have no volume. Therefore, their mass should be zero. However, they require a mass definition (i.e. density by unit surface $\bar{\rho}$) because in a dynamics system all the nodes need inertia and mass terms, which is usually not reported.

Solid elements with reduced integration are mostly used in LVI simulations [32,53,59,61,65,87,98,99,132,136,154] for their computational efficiency but also to alleviate locking pathologies while taking into account the three dimensional stress state. Mechanisms such as the *in situ* effect [34, 56] or matrix cracking induced delamination can be naturally captured with appropriate failure criteria and accurate stress fields. However, several elements through the thickness of every ply as well as good aspect ratios may be needed for accurate transverse stress fields.

Continuum shell elements or also called solid-shell finite elements are three dimensional elements with a shell-like kinematics but continuum topology. Contact takes place on the actual shell surface and thickness variations based on physical nodes are accounted for. Furthermore, they can be naturally connected with solid elements since both have displacements as degrees of freedom. Continuum shell elements allow higher aspect ratios than solid elements between in-plane and thickness dimensions. Nonetheless, the STI of continuum shell elements in explicit simulations can be controlled by the shell element thickness. Continuum shell elements have been used as an efficient alternative to solid elements for LVI and CAI simulation [3,36,116,117,131,134].

Conventional shell elements are structural elements based on plate theory. Plate theory takes advantage of the small thickness compared to the planar dimensions to reduce the full three-dimensional solid mechanics problem to a two-dimensional one. This involves a reduction in terms of computational cost while being suitable for bending problems because of the rotational degrees of freedom. Furthermore, in explicit simulations the element thickness does not detrimentally affect the element STI of the model. However, conventional shell elements do not provide accurate results for transverse shear and normal strains [153]. Love - Kirchhoff plate theory neglects transverse shear deformations while Reissner - Mindlin first order theory assume through the

thickness constant deformation by considering shear coefficients to correct the corresponding strain energy terms. Higher order theories have been proposed in the literature to improve the transverse description and a review can be found in Noor et al. [112]. Despite a poorer transverse description in comparison with solid or advanced continuum shell elements formulations, conventional shell elements are considered a well balanced combination in terms of accuracy and computational efficiency [112]. Nevertheless, contact related issues and poor kinematic description to account for delamination is reported when stacking several conventional shell elements over each other [31, 48]. This has probably limited its application for the simulation of the LVI and CAI simulation. Johnson et al. used conventional shell elements for the simulation of LVI on composite laminates [86]. Schwab et al. [141, 142] used conventional shell elements together with zero-thickness cohesive elements to model intermediate velocity impact and high energy impact on glass fabric reinforced epoxy components due to fan blade out. Shell elements are merged with zero-thickness cohesive element but with geometrical finite thickness as sketched in Fig. 2.6. The ply thickness is scaled within the contact formulation in regions of delaminations to avoid interpenetration issues when the cohesive elements are deleted. It is a computationally efficient approach but it is worth noting that non-conforming meshes cannot be used and inter-ply friction effects could only be accounted for if the interlaminar damage model is formulated accordingly. Also, the computed openings (i.e. slidings) might be inaccurate in some situations because the cohesive elements nodes are placed at the ply or sublaminate mid-plane and not at the actual interface position. Nevertheless, in situations where damage is highly localized (e.g. intermediate and high energy impact) or small transverse shear occurs (e.g. very small ply thickness) could be accurate enough.

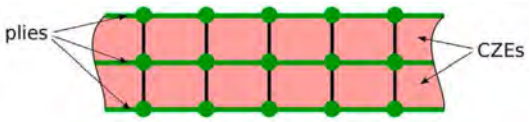

Fig. 2.6: Modeling strategy employed in Schwab et al. [141, 142] (source: Schwab et al. [142]).

Several modeling strategies are reported in the literature for the simulation of LVI of composite laminates. Despite being accepted the computational efficiency of conventional shell elements, they have not been used for the simulation of LVI and the sequential CAI of composite laminates. Furhtermore, a study that compares the different technologies in terms of computational performance and accuracy is missing in the literature.

2.1.4 Finite element discretization

The element size of the model is an important aspect that affects the stress field predictions and the correct intralaminar and interlaminar energy dissipation. Thus, it is related to model objecitivy.

Intralaminar discretization

The element size is important to accurately predict the stress field but also for correct intralaminar energy dissipation. Element sizes ranging from 0.5 to 2 mm are typically reported [2, 32, 36, 45, 53, 80, 87, 109, 126, 131, 132, 134, 136]. However, some authors [3, 65, 67, 98, 99, 154] highlight the importance of avoiding snap-back at the element level for correct intralaminar energy dissipation despite using a mesh regularization algorithm. The maximum element size is calculated for each damage mechanism ($N = \pm 1, \pm 2, 6$) by Eq. (2.4).

$$l^* \leqslant \frac{2G_N E_N}{X_N^2} \tag{2.4}$$

where l^*, E_N and X_N are the characteristic element length, the elastic modulus, and the strength for a given damage mechanism N, respectively.

If it is unfeasible the mesh size size prescribed by Eq. (2.4), the snap-back at the element level can be avoided by reducing the corresponding strength [26]:

$$X_N = \sqrt{\frac{2G_N E_N}{l^*}} \tag{2.5}$$

The damage initiation predictions is affected but the strength modification ensures correct energy dissipation.

Interlaminar discretization

The interlaminar mesh discretization has to be chosen according to the interlaminar FPZ size. The damage initiation and propagation are not correctly computed if the interlaminar FPZ or also called the CZL is not properly discretized, as highlighted in Turon et al. [158]. At least three elements are needed along the CZL for correct interlaminar damage predictions [60, 110]. Turon et al. [158] proposed an engineering solution for the use of coarse meshes on delamination which consists of reducing the material interface strength so as to enlarge the interlaminar FPZ while keeping the actual interlaminar fracture toughness for correct interlaminar energy dissipation.

The interlaminar FPZ is not generally considered in the selection of the mesh size but some authors [65, 87, 154] do consider this aspect through the formula proposed by Rice [135]. However, the expression was derived for infinite specimens under mode II fracture mode leading to an over-prediction of the actual CZL.

Hillerborg [75], one of the pioneers in using CZM with FEM, defined a characteristic length parameter (l_{ch}), which is a material property. Based on the definition from Hillerborg [75] and the equivalent elastic modulus for orthotropic materials derived by Sih et al. [146], Yang et al. [170] defined the characteristic length of orthotropic materials for pure mode I as:

$$l_{chI} = \frac{G_{Ic}E'_I}{\tau^2_{Ic}} = \frac{K^2_{Ic}}{\tau^2_{Ic}} \tag{2.6}$$

While the characteristic length for orthotropic materials under pure mode II loading is defined as [170]:

$$l_{chII} = \frac{G_{IIc}E'_{II}}{\tau^2_{IIc}} = \frac{K^2_{IIc}}{\tau^2_{IIc}} \tag{2.7}$$

where E'_i, G_{ic}, τ_{ic} and K_{ic} are the equivalent elastic modulus, the critical energy release rate, the strength, and the critical stress intensity factor, respectively. They are defined accordingly to the fracture mode (i = I, II).

The CZL and the characteristic length are proportional, but generally not the same. In fact, the characteristic length can significantly over-predict the CZL as demonstrated by the existing analytic [25, 55, 68, 84] and numerical studies [73, 157].

Within the CZM framework, different cohesive law shapes can be employed depending on the fracture mechanism to be modeled. The cohesive law shape contains information from physical processes occurring at the micro-scale. Some examples traditionally used are the constant, linear and quasi-exponential softening laws (see Fig. 2.7).

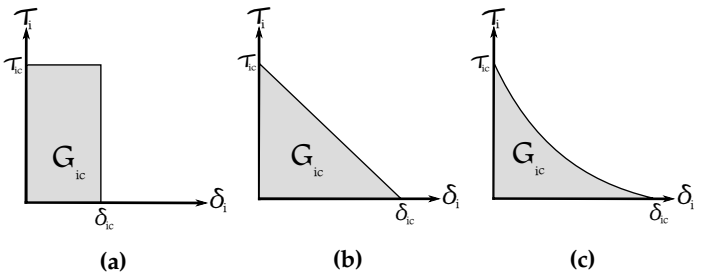

Fig. 2.7: a) Constant b) Linear and c) Quasi-exponential softening cohesive laws. $\tau_i - \delta_i$ represents traction vs. opening for mode I and shear stress vs. sliding for mode II (i = I, II).

Fig. 2.8 sketches the CZL with the stress profile for a linear and constant cohesive law shape. It is also sketched how the CZL drastically decreases with the arm thickness for slender bodies. The COD along the CZL depend on the cohesive law shape, the characteristic length, and structure geometry and size.

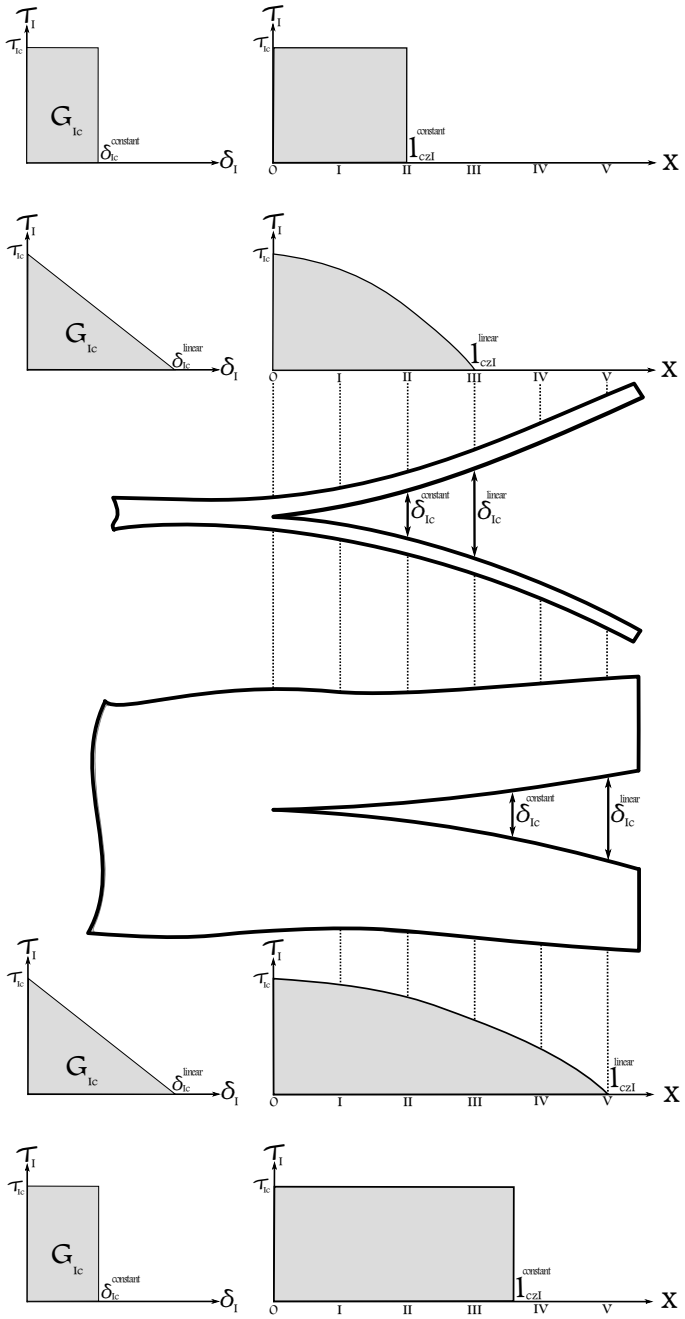

Fig. 2.8: Effect of the cohesive law shape and the structure size on the CZL and the stress distribution under pure mode I loading.

The CZL has an upper limit in which is not affected by the structure size. This occurs when the CZL is much smaller than the specimen size.

In Turon et al. [157], the CZL for a crack in an infinite specimen (l_{czi}^{∞}) was defined as:

$$l_{czI}^{\infty} = M_I^{\infty} \frac{G_{Ic} E_I'}{\tau_{Ic}^2} = M_I^{\infty} \, l_{chI} \tag{2.8}$$

$$l_{czII}^{\infty} = M_{II}^{\infty} \frac{G_{IIc} E_{II}'}{\tau_{IIc}^2} = M_{II}^{\infty} \, l_{chII} \tag{2.9}$$

where M_i^{∞} is a dimensionless constant, which depends on the fracture mode (i = I, II).

The different M_i^{∞} values found in the literature for different cohesive laws are summarized in Table 2.1.

Reference	M_i^{∞}	Cohesive Law	Mode
Irwin [82]	$1/\pi$	Constant	I
Dugdale [55] and others [24,57,84]	$\pi/8$	Constant	I
Palmer and Rice [124]	$\pi/8$	Constant	II
Planas and Elices [84], Bao and Suo [24]	0.731	Linear softening	I
Planas and Elices [84]	2.92	Quasi-exponential softening	I

Table 2.1: M_i^{∞} values (i = I, II) proposed in the literature for different cohesive laws in remotely loaded notched specimens.

The first author who estimated the size of the inelastic zone at the near field of an existing crack under pure mode I was Irwin [82]. Irwin obtained $M_I^{\infty} = \frac{1}{\pi}$ for a crack in an infinite sheet. Irwin's approach cuts the singularity off and introduces the yield strength. Then, it is imposed global equilibrium with the elastic stress distribution from Linear Elastic Fracture Mechanics (LEFM) on the perpendicular axis to the crack plane by extending the crack (i.e. effective crack). It does not represent the correct stress distribution at near tip field but it is an estimation.

Dugdale [55] also investigated plasticity at the front of an existing crack and the size of the plastic zone under pure mode I. Dugdale considered a constant cohesive law defined by the yield strength while assuming all plastic deformation to be lumped into the crack plane. No softening or failure criteria was originally included. Nevertheless, Dugdale's model becomes equivalent to consider a cohesive zone model with a constant law (Fig. 2.7a) if a cut-off is added so that the material completely breaks when a critical COD (δ_{ic}) is reached. As discussed in Bažant and Planas [25], the constant cohesive law does not usually give accurate results. However, it has traditionally been

of particular interest due to its analytic treatment. Dugdale [55] obtained $M_I^\infty = \frac{\pi}{8}$ under pure mode I loading by linear superposition of the stress intensity factors produced by the external loads and a constant cohesive force distribution along the CZL. The procedure correctly takes into account the stress field of a notched specimen subjected to a remote load with cohesive forces acting along the CZL.

Palmer and Rice [124] followed Dugdale's procedure to obtain $M_{II}^\infty = \frac{9\pi}{32}$ for the growth of slip surfaces in clays. It is straightforward to obtain $M_{II}^\infty = \frac{\pi}{8}$ for a constant cohesive law.

Smith [57] developed a closed-form expression for a range of constant piece-wise cohesive law shapes under pure mode I. It was also found $M_I^\infty = \frac{\pi}{8}$ for a constant cohesive law.

Planas and Elices [84] compared the CZL obtained from constant, linear and quasi-exponential cohesive laws under pure mode I loading. Dugdale's procedure complemented with an asymptotic analysis [130] previously developed by the same authors was used. The values obtained were $M_I^\infty = \frac{\pi}{8}$ for constant, $M_I^\infty = 0.731$ for linear, and $M_I^\infty = 2.92$ for quasi-exponential softening laws. Thus, the CZL is sensitive to the cohesive law shape. This finding is consistent with the previously obtained by Smith [57].

The CZL for remotely loaded infinite specimens is not generally applicable in the field of composites due to the slender nature of common laminate structures. For instance, in the commonly used Double Cantilever Beam (DCB) test [21] and the Calibrated End Load Split (C-ELS) test [83] in fracture mechanics, the CZL might be comparable or larger than the arm thickness.

Out of the infinite limit range, the CZL becomes fracture mode, material and structure dependent. Therefore, Eqs. (2.8) - (2.9) are not valid any more because the thickness effect is not taken into account.

Smith [149], using Euler-Bernoulli beam theory and assuming an initial crack size to be very large compared to the beam height, obtained the following analytic solution for the CZL of a homogeneous slender body under pure mode I:

$$l_{czI}^0 = (M_I^0\, l_{chI})^{1/4}\, h^{3/4} \tag{2.10}$$

where h is the arm thickness, M_I^0 is a dimensionless constant, which depends on the fracture mode (i = I,II). Table 2.2 shows the different M_I^0 values found in the literature for different cohesive laws.

Smith [149] obtained $M_I^0 = 1/3$ and $M_I^0 = 1$ for a constant and a linear softening law, respectively. The stress distribution due to the cohesive law considered was accurately taken into account by solving the boundary value problem. If a linearly decreasing stress distribution is assumed along the CZL, what implies that the cohesive law is not exactly linear, $M_I^0 = 2$. The assumption leads to slightly larger CZL predictions.

Bao and Suo [24] also obtained $M_I^0 = 1/3$ for the constant cohesive law

case. The equilibrium problem was not solved analytically. Instead, a numerical solution of the beam problem was used [152] to relate the critical energy release rate (G_{Ic}) with the CZL (l^0_{czI}).

The CZL of homogeneous slender bodies under mode II was studied by Massabò and Cox [107] when investigating mode II bridging mechanisms in delamination. Length scales for linear and power bridging laws were found. Assuming a cohesive crack in an isotropic material with a constant cohesive law for the ENF specimen Massabò and Cox obtained $M^0_{II} == 1/2$. If a linearly decreasing stress distribution is assumed, M^0_{II} becomes $M^0_{II} = 1$. The CZL for mode II scales as:

$$l^0_{czII} = \sqrt{M^0_{II}\, l_{chII}\, h} \tag{2.11}$$

Reference	$\mathbf{M}^0_i$	Cohesive Law	Mode
Smith [149] , Bao and Suo [24]	$\frac{1}{3}$	Constant	I
Smith [149]	1	Linear softening	I
Massabò and Cox [107]	$\frac{1}{2}$	Constant	II

Table 2.2: M^0_i values (i = I, II) proposed in the literature for different cohesive laws in pre-cracked slender specimens.

The analytic solutions for slender specimens assume a very large crack in comparison with the specimen height. The CZL changes during crack growth due to an increase of the structure compliance. Consequently, solutions assuming large crack length ensure a correct mesh discretization throughout the whole analysis.

To the author's knowledge only two studies in the literature [73,157] have compared the existent analytic formulas with the CZL obtained from numerical results. Both of them employed a linear softening cohesive law and the same baseline specimen geometry, laminate and interlaminar properties. In both studies the CZL was investigated under mode I (i.e. DCB test), mode II (i.e. ENF test) and Mixed Mode Bending loading (i.e. MMB test) for different arm thickness. Harper and Hallett [73] performed three-dimensional analyses while in Turon et al. [157] the analyses were two-dimensional under plane strain conditions. Both compared the numerical results with Eqs. (2.8) - (2.11).

Both studies concluded that Eqs. (2.8) - (2.11) significantly over-predict the numerically obtained CZL. Therefore, there is no clear and general expression to predict the CZL of composites undergoing delamination.

2.1.5 Element deletion criterion

Excessive element distortion issues, which can eventually abort the simulation, are common in explicit FEA that involve severe damage as LVI, CAI or crash simulations. This aspect can significantly compromise the accuracy and robustness of the numerical models even though it is often not discussed or clearly reported [2,36,45,61,109,126,132,134,150].

There is no clear agreement in the criterion to overcome element distortion issues in the literature. Some authors [3, 65, 80, 98, 99, 142, 154] delete the continuum elements when a certain value of the fiber damage variable is reached while others [59, 67, 87] limit the damage variable to a certain value without element deletion. Depending on the author, the fiber damage variable can grow up to 0.9 [87], 0.99 [59, 142, 154] or 0.999 [3, 65, 67, 98, 99] or even 1 [80]. However, this is not enough to avoid element distortion issues in UD laminates because the damaged matrix undergoes severe distortions. The transverse and shear damage variables are also limited in some studies to grow up to 0.99 [59,65,98] or 0.999 [3]. Tan et al. [154] deleted the elements when the shear strain reached 1% or when the fiber damage variable reached 0.99. Lately, Chiu et al. [41] in crash simulations proposed to delete the elements when the fiber damage variable reached 0.99 or when the determinant of the deformation gradient reached certain values, which were based on a sensitivity analysis.

2.2 LVI and CAI on thin ply laminates

Several studies on LVI and CAI of carbon/epoxy laminates at the coupon level have been reported in the literature during the last years. However, there exist new trends in terms of manufacturing and materials in the composite material community. In the recent years, a growing interest has been devoted towards thin ply composite materials. *Spread-tow thin-ply technology* [90] allowed to commercially produce UD and fabric thin ply laminae. The use of thinner laminae is aimed to produce thinner and lighter laminates but also with improved fiber orientation and uniformity, smoother ply drops and reduced crimp. It is also motivated by the enhancement of the damage resistance due to the *in situ* effect [34, 56], which gains importance when reducing the ply thickness in multidirectional laminates. The *in situ* effect on conventional UD ply laminates has been demonstrated experimentally [30,40,125,143] and numerically [11,14].

Comprehensive research work on the mechanical performance of UD thin-ply pre-preg based laminates [147,172,173] and UD non-crimp fabrics pre-preg have been carried out during the last decade [12,70]. Laminates with thinner plies generally have better damage resistance and fatigue life than conventional laminates because sub-critical damage mechanisms (e.g. matrix

cracking, delamination) occurrence prior to ultimate laminate failure are reduced or delayed in many situations [8, 10, 147, 172]. It is known that they exhibit a more brittle behaviour which can lead to earlier unstable failure in notched specimens under tensile loads (e.g. open hole tension) [10, 147]. However, there is no clear consensus on the LVI and CAI resistance of thin ply laminates [8, 64, 137, 144, 147, 173] but it could be said that thicker plies lead to larger delaminations while thinner plies lead to more fiber breakage during a LVI event. The aforementioned experimental studies reported that equal or improved CAI strength are achieved with thinner plies. In any case, experimental evidences [8, 137, 163, 164, 173] show that laminates with thinner plies behave differently than those with thicker ones under impact loads; fiber breakage becomes more relevant while matrix cracking is reduced and the consequent induced delamination is practically suppressed. It is thought that interlaminar stresses and fiber breakage induce delamination [137, 164]. These observations are reported either for UD [137] and fabric thin ply laminates [164].

Despite the existing interest and the comprehensive experimental research work done in the last years, less studies are found on the analysis of thin ply laminates which could bring some insight or support some thoughts based on experimental observation. A pioneering contribution was from from Olsson [115]. Olsson [115] presented an analytical model for damage prediction due to large mass impact in which the same thin-ply weave laminate used in the present thesis (see Chapter 5) was investigated (i.e. TeXtreme® 80 g/m^2). The model is applicable until fiber damage initiation. Olsson [115] concluded that compression fiber failure occurred before delamination and argues that delamination was likely to be induced by fiber fracture.

There exist two proceedings that report an attempt to model thin ply laminates computationally [116, 117] in order to overcome the limitations of analytical approaches. Olsson et al. [117] modeled TeXtreme® 100 g/m^2 cross - ply laminates as layered continuum shell elements, where each ply in the laminate was modeled as two perpendicular UD layers. The models under-predicted among 12.5 % to 25 % the energy dissipation. The authors attributed the disagreement with the experimental data to the fact that delamination was not considered in the model. Later, Olsson et al. [116] modeled the same quasi-isotropic laminate (i.e. TeXtreme® 80 g/m^2) from [115]. Olsson et al. [116] simulated the LVI and tensile after impact with the same previous approach [117]. However, some interfaces for delaminations were included (i.e. 2, 4 and 8). Nevertheless, the impact results still deviated with the consideration of some interfaces for delamination. Olsson et al. [116] concluded that both in-plane damage and delaminations needed to be included in the model and future work should focus on how this interaction can be accounted for in a sufficiently accurate and computationally efficient manner.

Therefore, thin ply laminates represent a modeling and computational

challenge due to the large number of plies and interfaces involved.

2.3 LVI and CAI on large composite structures

The literature on LVI and CAI simulation of large composite panels, which is certainly interesting from an industrial point of view, is much less extensive than at the coupon level. Probably, the computational effort is a limiting factor. Nevertheless, some peer reviewed works can be found on the LVI simulation of composite laminate structural components [59,87,134,150] but not on the sequential CAI. To the author's knowledge, there is only the reported work from Psarras et al. [131] on LVI and the sequential CAI simulation of large composite structures.

Johnson et al. [87] performed LVI on WR E-glass/Derakane 8084 vinyl - ester marine composite panels. The simulated impact energies ranged from 195 to 7200 J, which fall within the range of VID. Three different plates were simulated: $228.6 \times 177.8 \times 6.35$ mm^3, $1073.2 \times 768.4 \times 19$ mm^3 and $1370 \times 1370 \times 38$ mm^3. Solid elements were used with a CDM model inspired in the plane stress model from Williams et al. [167], which was extended to account for transverse shear damage. The damage model was fed with data obtained from cyclic tests. The damage variable was limited to 0.9 without element deletion and no mesh regularization algorithm was mentioned to be used. The element sizes employed were 1.6 and 3.2 mm for the smallest and the largest plates, respectively. Delamination was modeled by means of cohesive elements but not all the interfaces for delamination were considered for the medium and large panels. The stiffness and the dissipated energy were not well captured. However, it should be acknowledged the modeling challenge due to the panel dimensions and the impact energies, which involved large numerical models with a large amount of fiber breakage and delamination.

Faggiani and Falzon [59] simulated a LVI of 15 J on a 450 mm by 375 mm Carbon Fiber Reinforced Polymer (CFRP) panel with three I-stiffeners previously investigated by Greenhalgh et al. [69]. Fig. 2.9 sketches the modeling strategy used. The impact was located in between two stiffeners. A refined mesh region at the impact location with all the plies and interfaces for delamination was modeled with reduced integration 3-D solid elements and zero-thickness cohesive elements. The remaining of the panel was discretized with a single continuum shell element through the thickness (i.e. no delamination) which was coupled to the refined region through tie constraints. The element sizes used in the model were not reported. The CDM model from Donadon et al. [53] and the CZM from Camanho et al. [33] were used to model the intralaminar and interlaminar damage, respectively. A friction value of 0.5 was assumed for the ply-to-ply contact while 0.3 for the skin to impactor contact. The damage variables were limited to a maximum

value of 0.99 without element deletion to avoid excessive element distortion issues and the crack band model was used [26] for mesh regularization. Delamination was the main damage mechanism and only small amount of fiber breakage was predicted due to the low impact energy. The dissipated energy was under-predicted approximately about 12% but the projected delamination area and the overall force - time response were in good agreement with the experimental ones.

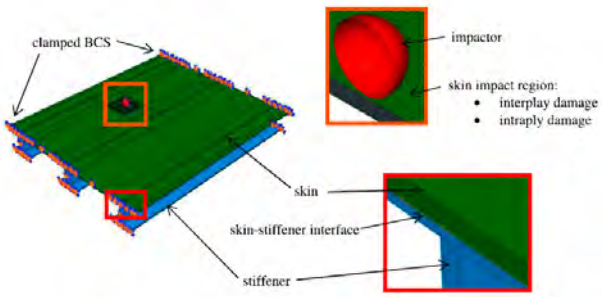

Fig. 2.9: Modeling strategy employed in Faggiani and Falzon [59] (source: Faggiani and Falzon [59]).

Riccio et al. [134] published a numerical study on a 246 mm by 368 mm stiffened composite panel with two omega shaped stringers together with experimental results. The impact was located close to a stiffener. The simulated impact energies were 15 J and 25 J. Continuum shell elements were used with Hashin CDM model [1] together with the crack band model [26]. The element size employed was not reported. Finite thickness (i.e. 0.01 mm) cohesive elements with quadratic nominal stress initiation criterion and a power law energy based propagation criterion were used to model delamination. The elements were deleted even though the criteria employed was not reported. A friction value of 0.5 was assumed for all contact pairs. The overall force - time response was captured. However, the energy dissipated was over-predicted by 20 % and 50 % in the 15 J and 25 J impact, respectively.

Psarras et al. [131] investigated the compressive residual strength of large curved stiffened panels after multi-site impacts. Two different laminate thicknesses and six multi-site impact scenarios were considered. The panel size was 1200 mm by 800 mm and the material used was T800/M21. The impact energies ranged from 25 to 58 J. Continuum shell elements with the plane stress intralaminar damage model proposed by Iannucci et al. [80] were used. Cohesive elements were placed among sublaminates to account for interlaminar damage. No more details on the model definitions such as the element size or element deletion were reported. The numerical predictions of the CAI strength were in good agreement for the thinnest panels (i.e. 1 - 3 %) while

the strength was over-predicted for the thickest ones (i.e. 19 - 32 %). The experiments demonstrated the influence of impact energy, location and number of multi-site impacts on the compressive residual strength.

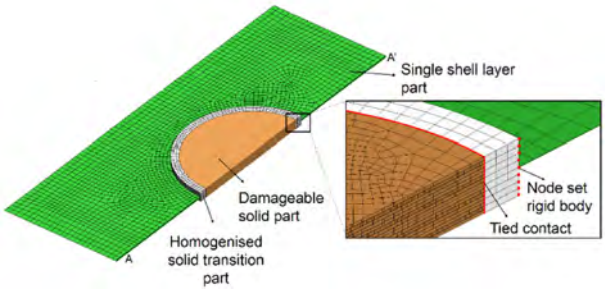

Fig. 2.10: Modeling strategy employed in Sun and Hallett [150] (source: Sun and Hallett [150]).

Recently, Sun and Hallett [150] performed a 15 J LVI simulation on a 450 mm by 375 mm stiffened panel made of HTA/6176C. The plies were modeled with reduced integration solid elements and cohesive elements were inserted vertically in each ply to model matrix cracking. Cohesive elements were also used to model delamination while fiber breakage was neglected. A shell to solid coupling, which is sketched in Fig. 2.10, was used to model the impact region in detail with all the plies and interfaces while single conventional shell elements through the thickness were used out of the impact region for the sake of computational efficiency. The element size was 0.2 mm in the refined region. The modeling approach was firstly validated with experimental data and compared with a full 3-D numerical model for ASTM standard specimens [16]. Computational time savings up to 50 % were reported with the shell to solid coupling approach in comparison with the full 3-D model even though the results yield to larger contact times and suffer more oscillations. However, the only reported output of the stiffened panel was the force-time response with the solid/shell approach, which was in agreement with experimental data.

2.4 Summary

Based on the literature review, it can be concluded that there exists an extensive number of investigations support the CDM and the CZM as frameworks to model LVI and the sequential CAI test. They mostly use explicit solvers to circumvent numerical difficulties due to the non-linear nature of the problem. In general, those studies have successfully reproduced experimental results at the coupon level by modeling the meso-scale of composite laminates.

Different modeling strategies with different finite element types and cohesive interaction technologies are present in the literature. However, it lacks a study that compares their accuracy and computational performance. Cohesive elements are preferred over cohesive surfaces to model the interlaminar behaviour due to their computational benefits. Nevertheless, it is not clear the definition of some numerical parameters that affect the model accuracy and computational performance such as the surface density and the penalty stiffness of zero-thickness cohesive elements. Solid elements are the prefered option over other finite element types. In fact, conventional shell elements have not been used to perform both LVI and the sequential CAI simulation of composite laminates.

The damage evolution of the intralaminar and interlaminar damage models is generally assumed. However, some studies highlight the importance of the shape evolution when the FPZ is not negligible.

There is agreement on the definition of the continuum finite elements discretization to accurately dissipate the intralaminar energy but less attention is paid on the interlaminar discretization. In fact, numerical investigations highlight that the existent formula over-predict the actual interlaminar FPZ of composites undergoing delamination.

Excessive element distortion issues are reported on LVI and CAI simulations. Nonetheless, different criterion are found in the literature without any clear consensus.

Finally, scarce studies have been found on the LVI and sequential CAI on thin ply laminates and large composite structures which are computationally challenging and certainly of clear interest.

Part II

Methodology

Chapter 3

Failure process zone in composites delamination

3.1 Introduction

Delamination is one of the damage mechanisms that might occur in polymer-based laminated composite materials. FPZ development occurs during delamination, where dissipation mechanisms take place. Within a numerical framework, a fine discretization is needed along the interlaminar FPZ (CZL) to accurately capture the non-linear stress distribution [155]. Knowing the CZL beforehand is important for an optimum mesh discretization. Numerical investigations [73, 157] showed that there is a wide range of situations in which the CZL cannot be predicted by the existent analytic bounding solutions from Eqs. (2.8) - (2.11). Consequently, it is of interest to determine their range of applicability.

This chapter studies the range of applicability of the bound solutions in a parametric manner, which is based on the two governing variables from Eqs. (2.8) - (2.11); the material characteristic length (l_{ch}) and arm thickness (h). Also, novel empirical formulas are proposed to predict the CZL of homogeneous orthotropic materials with a crack growing under pure mode I or pure mode II.

The material characteristic length (l_{chi}) for orthotropic materials defined by Eqs. (2.6) - (2.7) depends on the equivalent elastic modulus, the critical energy release rate and the strength. The material characteristic length is defined accordingly to the fracture mode (i = I, II). The equivalent elastic modulus (E_i') comes from the relation between the energy release rate and the stress intensity factor derived by Sih et al. [146] while investigating cracks in anisotropic bodies. For a crack such as the one in Fig. 2.1 with the principal

axis (1, 2) coinciding with the coordinate axis (x, y), the equivalent elastic modulus for mode I and mode II are respectively defined as:

$$E'_I = E_1 \lambda^{3/4} \sqrt{\frac{2}{1+\rho}} \tag{3.1}$$

$$E'_{II} = E_1 \lambda^{1/4} \sqrt{\frac{2}{1+\rho}} \tag{3.2}$$

where E_1 is the Young modulus in the principal direction of the material (see Fig.2.1), and λ and ρ are two dimensionless elastic parameters used by Suo [151]. The dimensionless parameters are used here to study the degree of orthotropy effect on the CZL in a parametric manner. The dimensionless parameters, λ and ρ, are defined in terms of the engineering elastic constants [151]:

$$\lambda = \frac{E_2}{E_1} \qquad \rho = \frac{\sqrt{E_1 E_2}}{2G_{12}} - \sqrt{\nu_{12}\nu_{21}} \tag{3.3}$$

The equivalent elastic modulus depends on the stress state. For plane strain problems, the elastic constants (i.e. E_1, E_2, ν_{12}, ν_{21}) should be replaced in Eqs. (3.1) - (3.3) by:

$$\begin{aligned} E'_1 &= \frac{E_1}{1-\nu_{13}\nu_{31}} & \nu'_{12} &= \frac{\nu_{12}+\nu_{13}\nu_{32}}{1-\nu_{13}\nu_{31}} \\ E'_2 &= \frac{E_2}{1-\nu_{23}\nu_{32}} & \nu'_{21} &= \frac{\nu_{21}+\nu_{23}\nu_{31}}{1-\nu_{23}\nu_{32}} \end{aligned} \tag{3.4}$$

3.2 Methodology

3.2.1 Description of the numerical analysis

A numerical investigation was carried out to determine the range of applicability of the CZL analytic bounds defined by Eqs. (2.8) - (2.11). The analytic Eqs. (2.8) - (2.11) demonstrate that the CZL is governed by the characteristic length of the material (l_{chi}) and the specimen thickness (h). Therefore, the numerical analyses were done in a parametric manner in order to investigate a wide range of scenarios. The CZL was normalized (l_{czi}/l_{chi}) and the scaling parameter to study was (h/l_{chi}). First of all, isotropic cases were studied. Finally, the degree of orthotropy was also studied parametrically to determine the applicability of the current formula to orthotropic materials. This was done through the dimensionless elastic parameters λ and ρ.

The numerical study is restricted to cohesive laws with linear softening such as in Fig. 2.7b. Its compromise among accuracy and computational efficiency [5] has made it widely used to model delamination in composites.

On the one hand, a total of 75 numerical DCB test were carried out to check the CZL under pure mode I loading (l_{czI}) and linear softening. A wide range of degrees of orthotropy ($0.08 < \lambda < 2$ and $1 < \rho < 20$), specimen thickness ($0.25 < h < 40$ mm), and characteristic length ($1.6 < l_{chI} < 44$ mm) were considered as Table 3.1 shows.

l_{chI}	λ	ρ	h [mm]
16.92	1	1	1, 2, 4, 7, 10, 25, 40
22.56	1	1	0.5, 1, 2, 5, 10, 15, 30
26.33	1	1	1, 4, 10
33.84	1	1	1, 2, 7, 15, 25, 40
43.43	1	10	0.25, 2, 5, 10, 40
3.13	1	20	0.5, 2, 5, 10, 40
14.64	0.1	1.86	0.5, 1, 2, 5, 10, 40
7.44	0.1	10	0.25, 0.5, 1, 2, 5, 10
5.48	0.1	20	0.5, 1, 2, 5, 10, 40
2.81	0.5	1	0.5, 2, 7, 15
3.19	0.5	10	0.5, 2, 7, 15
3.55	2	1	0.5, 2, 7, 15
2.9	2	10	2, 7, 15
11.42	1.22	0.782	0.25, 1, 10, 40
1.66	0.086	3.5	0.25, 1, 2, 5, 10

Table 3.1: Material properties and specimen thickness used in the parametric study for pure mode I.

On the other hand, 75 numerical C-ELS test were done to check the CZL under pure mode II loading (l_{czII}) and linear softening. Also, a wide range of degrees of orthotropy ($0.08 < \lambda < 2$ and $1 < \rho < 20$), specimen thickness ($0.1 < h < 40$ mm) and characteristic length ($2.2 < l_{chII} < 30$ mm) were considered as Table 3.2 shows.

The numerical analyses were carried out through the built-in cohesive surfaces from *Abaqus/Standard* [1]. They are based on the CZM approach and contact pair algorithm.

The cohesive surfaces use cohesive laws such as the ones shown in Fig.

l_{chII}	λ	ρ	h [mm]
16.97	1	1	0.1, 0.2, 0.3, 0.5, 1, 4, 7, 10, 15, 25, 40
29.71	1	1	0.25, 0.5, 1, 2, 8, 20
12.66	1	10	0.25, 0.5, 1, 2, 8, 20
9.16	1	20	0.25, 0.5, 1, 2, 8, 20
19.97	0.1	1	0.25, 0.5, 1, 2, 8, 20
6.28	0.1	10	0.25, 0.5, 1, 2, 8, 20
8.97	0.1	10	0.25, 0.5, 1, 2, 8, 20
6.61	0.1	20	0.25, 0.5, 1, 2, 8, 20
6.82	0.5	1	1, 2, 5, 10, 20
2.81	0.5	10	1, 2, 5, 10, 20
5.82	2	1	1, 2, 5
2.22	2	10	1, 2, 5, 10, 20
14.65	0.086	3.5	2, 4, 10, 20

Table 3.2: Material properties and specimen thickness used in the parametric study for pure mode II.

2.7. Damage onset is related to the onset COD (δ_{i0}), which depends on the interface strength (τ_{ic}) and the penalty stiffness (i.e. $\delta_{i0} = K_{coh}\tau_{ic}$). A new crack surface is created when the fracture toughness (G_{ic}) is reached. In other words, the surface does not transfer stresses any more when the critical COD (δ_{ic}) is reached. No damage is considered under compression.

The material is perfectly bonded before crack initiation. Thus, the penalty stiffness value should be as large as possible so as to not contribute to the global compliance of the structure. However, it should not be too large to avoid spurious oscillations [139]. The value adopted for all the analyses presented here was $K_{coh} = 10^6$ N/mm^3.

The built-in CPE4I element from Abaqus/Standard was used [1]. It is a plane strain element type with incompatible modes that allow to better capture bending. A fine discretization is needed to correctly obtain the CZL. A minimum of ten elements through-the-thickness and along the CZL were guaranteed for all the analyses presented here.

3.2.2 Cohesive zone length expression

The present work proposes to use an asymptotic function to interpolate the intermediate scenarios from the infinite limit Eq. (2.8) to the slender limit Eq. (2.10) for mode I as follows:

$$l_{czI} = \left({l_{czI}^{0}}^{-n_I} + {l_{czI}^{\infty}}^{-n_I} \right)^{-\frac{1}{n_I}} \tag{3.5}$$

where n_I is a fitting parameter for a given cohesive law type. The dimensionless M_I^j value (j = 0, ∞) for Eqs. (2.8) and (2.10) should be defined according to the cohesive law employed. For a linear cohesive law, M_I^0 = 1 and M_I^∞ = 0.731.

Similarly, an asymptotic function to interpolate the intermediate scenarios from the infinite limit Eq. (2.9) to the slender limit Eq. (2.11) for mode II is proposed:

$$l_{czII} = \left({l_{czII}^{0}}^{-n_{II}} + {l_{czII}^{\infty}}^{-n_{II}} \right)^{-\frac{1}{n_{II}}} \tag{3.6}$$

where n_{II} is a fitting parameter for a given cohesive law type. The dimensionless M_{II}^j value (j = 0, ∞) should be defined in Eqs. (2.9) and (2.11) according to the cohesive law employed. For a linear cohesive law, M_{II}^0 = 1 and M_{II}^∞ = $9\pi/32$.

3.2.3 Numerical cohesive zone length determination

The numerical CZL is defined as the length from the first node which has reached the interface strength to the first node with zero stress. Fig. 3.1a and Fig. 3.1b show the stress distribution along the crack path in a DCB and C-ELS test, respectively.

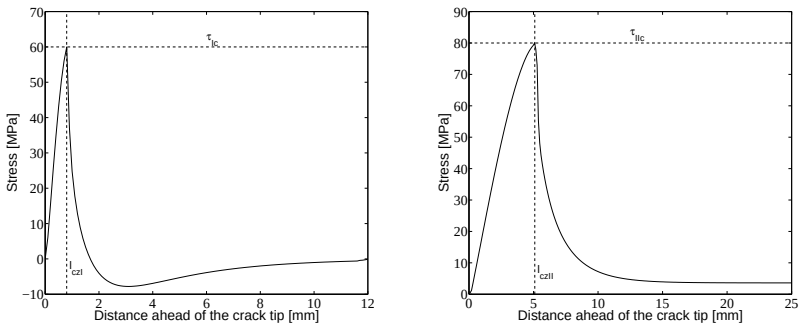

Fig. 3.1: (a) Normal and (b) shear stress distribution along the crack path of a DCB and C-ELS test, respectively.

The simulated material is T300/977-2 carbon fiber reinforced epoxy laminate [158]. The material properties are defined in Table 3.3 and the arm thickness (h) was 1.98 mm. The mesh size employed was 0.05 mm and 0.1 mm for the DCB and C-ELS, respectively. A linear cohesive law was used. The boundary conditions for the DCB and C-ELS are sketched in Figs. 3.2a - 3.2b , respectively. The predicted CZL by the DCB and C-ELS numerical model was 0.75 mm and 5.1 mm, respectively.

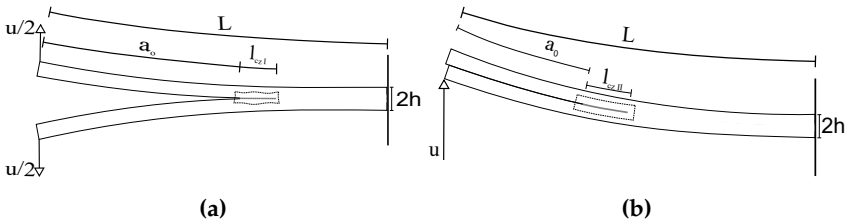

Fig. 3.2: (a) DCB and (b) C-ELS boundary conditions, respectively.

3.3 Results and discussion

3.3.1 Cohesive zone length under pure mode I loading

The solutions from Smith [149] and Planas and Elices [84] were used to feed Eq. (3.5). The exponent n_I from Eq. (3.5) was obtained by least-square fit from the 75 numerical simulations under pure mode I loading. For a linear cohesive law, $n_I = 0.9204$. Thus, Eq. (3.5) for pure mode I becomes:

$$\frac{l_{czI}}{l_{chI}} = \left(\left(\left(\frac{h}{l_{chI}} \right)^{3/4} \right)^{-0.9204} + 0.731^{-0.9204} \right)^{-\frac{1}{0.9204}} \tag{3.7}$$

The numerical results are compared in Fig. 3.3 with the proposed Eq. (3.7), the slender limit Eq. (2.10) from Smith [149] and the infinite limit Eq. (2.8) from Planas and Elices [84]. The results are presented in a dimensionless form l_{czI}/l_{chI} vs. h/l_{chI} for the sake of clarity. The CZL is mainly controlled by the ratio h/l_{chI}. The degree of orthotropy effect on the CZL is properly taken into account by the characteristic length Eq. (2.6) through the equivalent elastic modulus (E'_I) defined in Eq. (3.1).

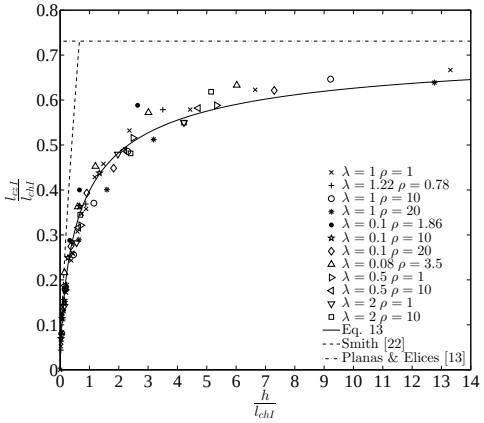

Fig. 3.3: Comparison of the numerical results for pure mode I with Eq. (3.7), Smith's expression [149] and Planas and Elices's expression [84].

As pointed out by previous numerical investigations [73, 157], both analytic bounds overestimate the numerical results. Furthermore, there is a wide range of cases which fall among the two analytic limits. Nevertheless, the proposed Eq. (3.7) is able to predict with good agreement the whole considered range. The relative errors of the normalized CZL from Smith's solution [149], Planas and Elices's solution [84] and Eq. (3.7) are shown in Fig. 3.4.

The relative errors of the analytic bounds are large and controlled by the ratio h/l_{chI} (Figs. 3.4a - 3.4b). For the studied cases, relative errors below 50 % are found when the ratio h/l_{chI} is larger than 2 and smaller than 0.15 for the infinite and slender case, respectively. Therefore, the existing analytic formulas for mode I (Eqs. (2.8) and (2.10)) have relative errors larger than 50 % for $0.15 < h/l_{chI} < 2$. The proposed Eq. (3.7) always keep the relative error below 23 %. The average relative error is 8.7 % with a standard deviation of 6.6 %. For the studied cases, the relative errors from Eq. (3.7) are always lower than those obtained from Smith's solution and Planas and Elices's solution. The degree of orthotropy effect does not show a clear influence on the relative error.

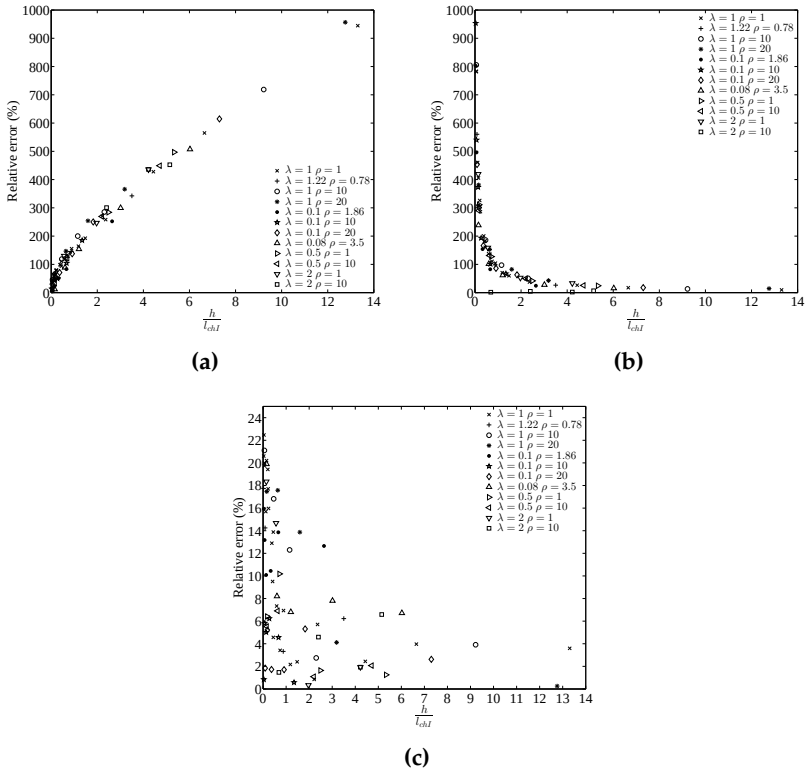

Fig. 3.4: Relative error on the CZL prediction for pure mode I with (a) Smith's expression [149], (b) Planas and Elices's expression [84] and (c) Eq. (3.7).

3.3.2 Cohesive zone length under pure mode II loading

The solutions from Massabò and Cox [107] and Palmer and Rice [124] are used in Eq. (3.6). The exponent n_{II} from Eq. (3.6) was obtained by least-square fit from the 75 numerical simulations under pure mode II loading. For a linear cohesive law, $n_{II} = 1.1587$. Thus, Eq. (3.6) can be written as:

$$\frac{l_{czII}}{l_{chII}} = \left(\left(\sqrt{\frac{h}{l_{chII}} \sqrt{\frac{1+\rho}{2\sqrt{\lambda}}}} \right)^{-1.1587} + \left(\frac{9\pi}{32} \right)^{-1.1587} \right)^{-\frac{1}{1.1587}} \tag{3.8}$$

Based on the numerical results, it has been observed that for orthotropic materials under mode II loading the normalized CZL (l_{czII}/l_{chII}) scales with ($h\sqrt{1+\rho}\,/\,l_{chII}\sqrt{2\lambda^{1/2}}$). This essentially means that the mode II equivalent elastic modulus (E'_{II}) in the slender limit is equal to the principal one (E_1) of the material (see Eq. (3.2)).

Fig. 3.5 compares the numerical results with the proposed Eq. (3.8), the slender limit Eq. (2.11) from Massabò and Cox [107] and the infinite limit Eq. (2.9) from Palmer and Rice [124]. As in the previous section, the results are presented in a dimensionless form l_{czII}/l_{chII} vs. $(h\sqrt{1+\rho}\,/\,l_{chII}\sqrt{2\lambda^{1/2}})$ for the sake of clarity. The degree of orthotropy effect is properly taken into account by the characteristic length Eq. (2.7) through the equivalent elastic modulus (E'_{II}) defined in Eq. (3.2).

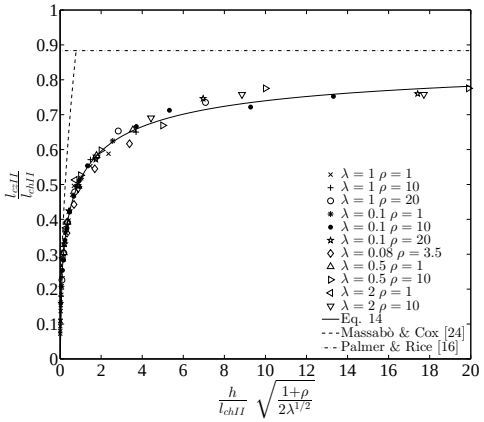

Fig. 3.5: Comparison of the numerical results for pure mode II with Eq. (3.8), Massabò and Cox's expression [107] and Palmer and Rice's expression [124].

The relative errors of the normalized CZL obtained from Massabò and Cox's solution [107], Palmer and Rice's solution [124] and Eq. (3.8) are shown in Fig. 3.6. Both analytic bounds overestimate the numerical results as found for mode I and by other authors [73,157].

The relative errors of the analytic limits are large and they are controlled by the ratio $(h\sqrt{1+\rho}\,/\,l_{chII}\sqrt{2\lambda^{1/2}})$. For the studied cases, relative errors below 50 % are found when the ratio $(h\sqrt{1+\rho}\,/\,l_{chII}\sqrt{2\lambda^{1/2}})$ is smaller than 0.35 and larger than 0.8 for the slender and the infinite case, respectively.

For the studied cases, the relative errors of the proposed Eq. (3.8) are always below 11 %. For the studied cases, the average relative error is 2.9 % with a standard deviation of 2.6 %. The relative errors from Eq. (3.8) are always lower than Massabò and Cox's [107] and Palmer and Rice's [124] solutions.

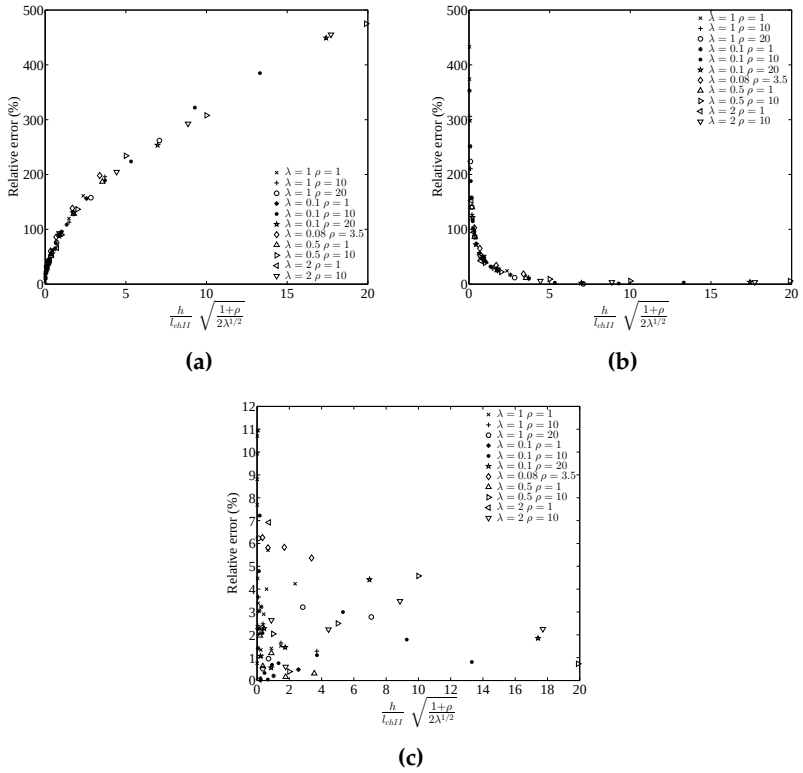

Fig. 3.6: Relative error on the CZL prediction for pure mode II with (a) Massabò and Cox's expression, (b) Palmer and Rice's expression [124] and (c) Eq. (3.8).

3.3.3 CZL and interface strength modification

The CZL of a crack propagating in a homogeneous specimen with a linear softening cohesive law under a pure fracture mode can be estimated by Eqs. (3.7) and (3.8). Under these hypothesis, it is possible to know beforehand an optimum mesh when using the CZM within the FEM framework.

An application case of the proposed Eqs. (3.7) - (3.8) is done through a DCB and C-ELS simulation tests. The simulated material is an unidirectional T300/977-2 carbon fibre reinforced epoxy laminate from Morais et al. [51], which was previously simulated by Turon et al. [158]. The DCB specimen was 150 mm long, with two 1.98 mm thick arms, and it had an initial crack length of 55 mm. While the C-ELS specimen had the same dimensions with an initial crack size of 85 mm. The material properties are in Table 3.3.

Based on Eq. (3.7), the CZL for the DCB test with material properties from Table 3.3 and 1.98 mm arm thickness is 0.681 mm. The CZL numerically obtained with a mesh size of 0.05 mm is 0.75 mm. In the case of mode

E_1	$E_2 = E_3$	$G_{12} = G_{13}$	G_{23}	$\nu_{12} = \nu_{13}$	ν_{23}	G_{Ic}	G_{IIc}	τ_{Ic}	τ_{IIc}
150 GPa	11 GPa	6 GPa	3.7 GPa	0.25	0.45	0.352 N/mm	1.45 N/mm	60 MPa	80 MPa

Table 3.3: Mechanical and interface material properties of T300/977-2 [51].

II, Eq. (3.8) predicts a CZL of 5.133 mm for a C-ELS test with material properties from Table 3.3 and 1.98 mm arm thickness, while the CZL numerically obtained with a mesh size of 0.1 mm is 5.1 mm.

The CZL scales with the material characteristic length. Based on this, Turon et al. [158] proposed an engineering solution for the use of coarse meshes on delamination which consists of reducing the material interface strength so as to enlarge the CZL. However, the interface strength only scales linearly at the infinite limit. Consequently, the scaled interface strength is overestimated out of the infinite limit range of applicability what leads to incorrect results and convergence issues.

As sketched in Fig. 3.7 for a C-ELS test, the CZL within a FEM framework is defined as:

$$l_{cz} = N_e l_e \tag{3.9}$$

where N_e and l_e are the number of damaging elements and their size, respectively.

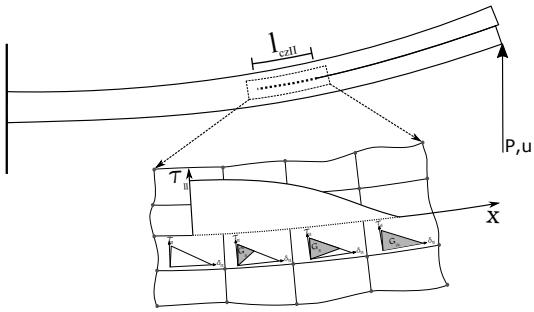

Fig. 3.7: C-ELS specimen. Detail of shear stress distribution along the CZL with damaging cohesive elements. Linear softening cohesive law.

To properly apply the engineering solution proposed by Turon et al. [158] for any specimen size and material characteristic length Eqs. (3.7) and (3.8) should be used. A modified cohesive zone length (l_{czim}) is defined according to the desired number and size of damaging elements. The modified interface strength (τ_{im}) is obtained according to Eqs. (3.7) and (3.8) iteratively. Alternatively, it can be used Fig. 3.8, where a strength reduction factor (τ_{im}/τ_{ic}) is given as a function of the ratio between the specimen thickness and the original characteristic length (h/l_{chi}) and the desired CZL factor (l_{czi}/l_{czim}).

Fig. 3.9a compares the load displacement curve from the analytic so-

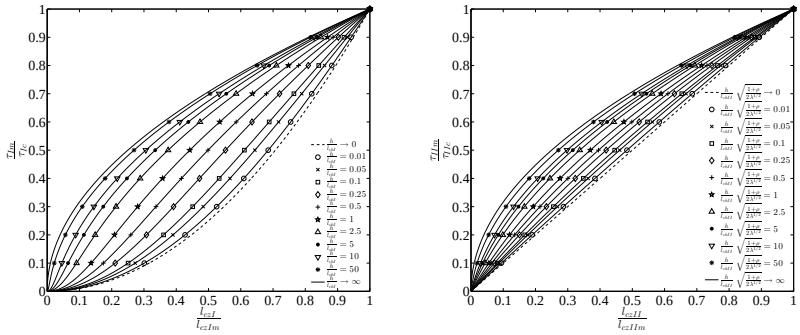

(a) **(b)**

Fig. 3.8: Strength reduction factor vs. CZL factor for different $\frac{h}{l_{chi}}$ under (a) pure mode I and (b) pure mode II.

lution (LEFM) with the numerically obtained using different element mesh sizes. The stress distribution at the vicinity of the crack tip is not correctly captured because there are less than three elements along the CZL what leads to incorrect damage onset and propagation. Furthermore, it is difficult to get a converged solution. The case with an element size of 5 mm converged because damping was included. Fig. 3.9b shows the load displacement curve from the analytic solution (LEFM) and the numerically obtained with modified interface strength (τ_{im}). The interface strength was modified in order to distribute the damage along three elements (N_e = 3) for different element sizes (l_e = 0.25, 0.5, 1, 2, 3, 5 mm).

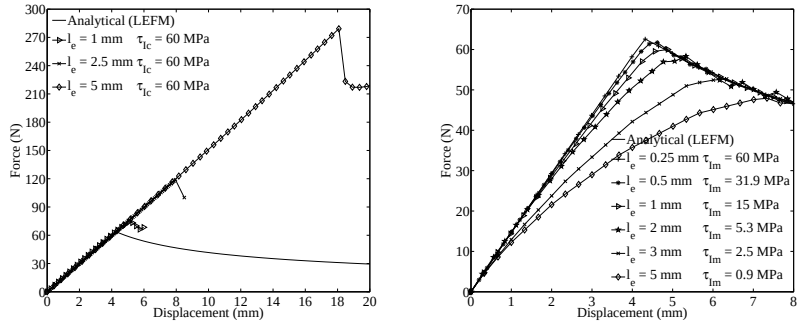

(a) **(b)**

Fig. 3.9: DCB test. Load-displacement curves for different element sizes (l_e) (a) without and (b) with interface strength modification according to the element size (l_e) and number of elements (N_e=3) within the CZL.

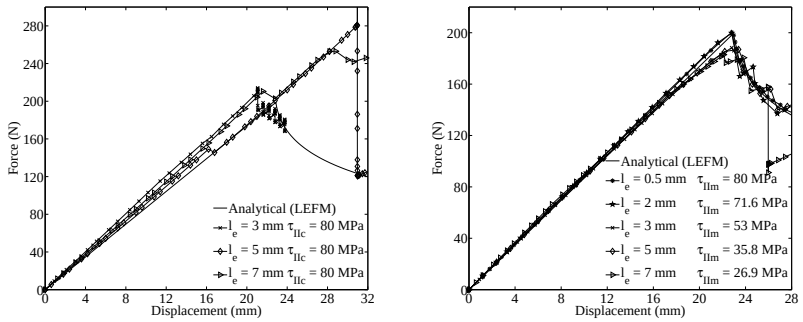

Fig. 3.10: C-ELS test. Load-displacement curves for different element sizes (l_e) (a) without and (b) with interface strength modification of interface strength according to the element size (l_e) and number of elements ($N_e = 3$) within the CZL.

As long as the increase of the CZL is not very large, the crack initiation can still be reasonably predicted. However, this strategy guarantees correct crack propagation as shown in Fig. 3.9b. The proposed Eq. (3.7) also ensures and appropriate use of the engineering solution from Turon et al. [155] without convergence issues.

The same was done for mode II loading. Fig. 3.10a compares the analytic (LEFM) load displacement response with the numerically obtained without interface strength modification. Fig. 3.10b compares the response when modified interface strength is used according to Eq. (3.8). The interface strength was modified in order to distribute the damage along three elements (N_e = 3) for different element sizes (l_e = 0.5, 2, 3, 5, 7 mm).

3.4 Conclusions

Numerical analyses were conducted to investigate the range of applicability of the existent analytic solutions for the CZL determination, which were found to be small. Based on the numerical investigation, novel empirical formulas have been proposed to predict the CZL of a delamination growing at the mid-plane of an homogeneous orthotropic laminate under pure fracture mode I and mode II for linear softening cohesive laws.

The cohesive zone length for delamination depends on the fracture mode, the specimen size and the cohesive law shape. The cohesive law shape modifies the dimensionless scalar M_i^j value. Therefore, an appropriate dimensionless M_i^j value as well as the exponent n_i should be used when considering other cohesive law shapes.

The conducted numerical study confirms that the structural response is affected if less than three elements along the CZL are used. The proposed expressions predict with accuracy the CZL for any characteristic length, specimen thickness, and a wide range of degrees of orthotropy. The estimation of the CZL allows an efficient mesh discretization within the FEM and CZM framework. Furthermore, the proposed expressions lead to accurate results without convergence issues when adopting strategies for the use of coarse meshes such as interface strength modification.

Chapter 4

LVI and CAI simulation methodology

4.1 Introduction

During an impact event both intralaminar (i.e. matrix cracking, fiber breakage) and interlaminar (i.e. delamination) damage mechanisms take place. Several studies from the literature support that the meso-scale provides enough detail of the stress field for LVI and CAI predictions of composite plates. The literature review done in Chapter 2 showed that there is agreement in using CDM and CZM as frameworks to model intralaminar and interlaminar, respectively. Explicit schemes are generally used in the literature to avoid some of the numerical difficulties from implicit solvers. However, impact numerical models require to define many other parameters that affect the robustness, efficiency, accuracy and objectivity of the numerical models, which sometimes are not clearly reported.

This chapter aims to propose a modeling methodology in which the relevant definitions are described concisely paying especial attention towards the computational efficiency. Furthermore, the chapter covers a gap found in the literature, which is the use of conventional shell elements for the simulation of LVI and CAI of composite laminates and the comparison among different finite element types and cohesive interaction technologies commonly used in the literature.

A numerical benchmark with the proposed methodology is applied in the UD pre-preg AS4/8552 carbon-epoxy previously studied by González et al. [65]. González et al. [65] used solid elements with finite thickness cohesive elements. Abaqus/ Explicit [1] is used to perform the simulations in the present work.

4.2 Virtual test set-up

The model reproduces the experimental drop weight impact test from González et al. [65] according to the ASTM D7136 standard [16] using a CEAST Fractovis Plus instrumented drop-weight tower with an automatic anti-rebound impactor system while the CAI tests were performed according to the standard ASTM D7137 [17] on a MTS Insight^{TM} Electromechanical tester with a 300 kN load cell.

4.2.1 Geometry and boundary conditions

The geometry and boundary conditions of the LVI model are shown in Fig. 4.1. The hemispherical impactor of 16 mm diameter and 5 kg is modeled with rigid elements (R3D4) with a minimum element size of 0.5 mm. An initial velocity in the out-of-plane direction is assigned to the impactor according to the impact energy tested. The remaining degrees of freedom are fixed. The rectangular specimens with a size of 100 $\times$ 150 mm^2 are placed over a flat support with a 125 $\times$ 75 mm^2 rectangular cut-out. The support, which have all the degrees of freedom fixed, is modeled with rigid elements (R3D4) that have a maximum element size of 2.5 mm. The specimen is restrained during the impact by means of four clamps which are cylinder-shaped with a diameter of 14 mm. They are modeled with rigid elements (R3D4) and all the degrees of freedom are fixed as in [65] . The maximum element size is of 1 mm.

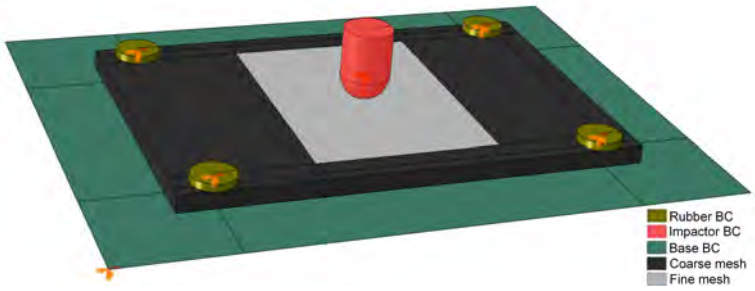

Fig. 4.1: Sketch of the LVI numerical model boundary conditions.

The geometry and boundary conditions of the CAI model are sketched in Fig. 4.2. The specimen fixture assembly was placed between plates and end-loaded under compression until specimen failure. A set of nodes are defined to represent the experimental set-up, which restrain the out-of plane and the lateral movement at the knife edges and side clamping zones of the specimen.

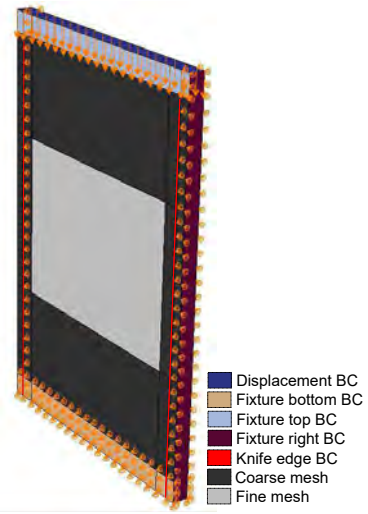

Fig. 4.2: Sketch of the CAI numerical model boundary conditions.

4.2.2 Contact and friction

Contact is simulated by means of the general contact algorithm from Abaqus/ Explicit [1]. Any possible new contact throughout the simulation is taken into account. The efficiency of the contact algorithm is improved by defining the contact pairs known beforehand (i.e. ply by ply). Cohesive elements are excluded from the contact algorithm because normal contact is already guaranteed by continuum elements that model the plies. The contact penalty method is used, where the contact stiffness value (K_n) is defined equal to the penalty stiffness of the cohesive elements (K_{coh}) in order to control the model STI. A sensitivity analysis is carried out to select the optimum penalty stiffness value in terms of accuracy (i.e. not affecting laminate compliance) and computational performance.

Normal pressures allow frictional forces to arise during an LVI event. Friction is introduced between all the contacting surfaces through the Abaqus/ Explicit [1] built-in Coulomb friction model. The same friction coefficients employed in [65] are used: 0.5 between plies and 0.3 between impactor and plies.

4.3 Plate modeling

The studied case is the 19.3 J impact on the $[45_4/0_4/-45_4/90_4]$s laminate with a cured thickness of 5.8 mm from [65]. The plate is modeled at the mesoscale level, which considers every ply as a homogenized material and all

the interfaces susceptible for delamination. However, ply clustering is modeled as one ply because experimental evidence shows that delamination does not occur within ply clusters [65]. The selected laminate with an unusual ply thickness due to ply clustering is an interesting scenario to assess possible limitations of plane stress based finite elements, which are recognized as less accurate due to neglecting out-of-plane stresses and poorer accuracy in the transverse shear stresses.

A mesh refined region with regular elements, which ensures correct energy dissipation, is only defined at the impact site to reduce the computational effort. The models used in the benchmark do not have the elements oriented according to the fiber direction because they were not sensitive to finite element mesh orientation (see Section 4.4.4). The refined region has a size of 84 $\times$ 90 mm^2 to allow the damage progression during the LVI and CAI simulation (see Figs. 4.1 - 4.2).

4.3.1 Modeling strategy

Different finite element and interaction technologies are possible in FEA. Solid elements with reduced integration finite elements are mostly used [32, 53, 59, 61, 65, 87, 98, 99, 132, 136, 154] while continuum shell elements have been used as an efficient alternative to solid elements [3, 36, 116, 117, 131, 134]. Conversely to solid elements, conventional shell elements do not accurately account for out-of-plane stresses and transverse damage mechanisms are neglected. On the other hand, the plane stress condition makes the constitutive model simpler than a full 3-D constitutive model required by solid elements.

It is important to take into account the effect of the modeling strategy on the model STI for the sake of computational efficiency. Conventional shell elements do not penalize the element STI (Eq. (2.1)) due their element thickness which is usually small in composite laminates in Abaqus/Explicit [1]. Similarly, zero-thickness cohesive elements or cohesive surfaces do not penalize the cohesive STI (Eq. (2.2)) due to element thickness while finite thickness cohesive elements do penalize it (Eq. (2.1)).

Despite the argued computational benefits from conventional shell elements, scarce studies are found in the literature to model LVI [86] and non on the sequential CAI simulation of composite laminates. One possible reason could stem in the reported contact related issues and poor kinematic description to account for delamination when stacking several conventional shell elements over each other [31, 48].

These issues can be circumvented by using tie constraints between shell and Surface Elements (SFM) (Fig. 4.3a) and between shell and cohesive elements (Fig. 4.3b) [67]. SFM from Abaqus/Explicit [1] allow to create a sheet of nodes without structural behaviour that allow to use conventional shell elements with cohesive surfaces. However, they require a mass definition (i.e.

density by unit surface) because in a dynamics system all the nodes need inertia and mass terms. In fact, its definition is analogous to zero-thickness cohesive elements.

Surface elements or zero-thickness cohesive elements are placed at the interface locations and then linked by means of tie constraints to the shell elements in order to ensure correct kinematic description at the interfaces for delamination. Surface to surface discretization is used for the tie constraints and the master surfaces always belong to the shell element surfaces. Shell elements are defined at the mid-plane, without offset. Both modeling strategies allow mismatching meshes which avoids mesh bias effects [63, 97] and they allow to account for friction effects by means of tangential contact from Abaqus/Explicit [1].

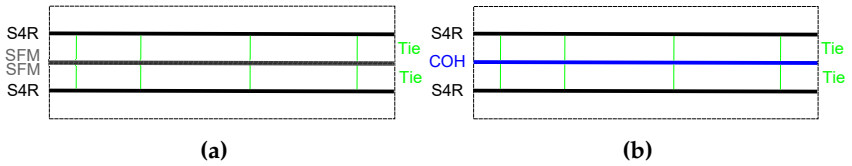

Fig. 4.3: (a) Modeling strategy with conventional shell elements (S4R) linked with surface elements (SFM) or (b) zero-thickness cohesive elements (COH3D8) through tie constraints for correct kinematic description of delamination.

Another aspect to consider when using conventional shell elements is the shell contact thickness. For instance, the general contact algorithm from Abaqus/Explicit [1] scales back the contact thickness automatically when a certain fraction of the surface facet edge length to thickness is exceeded. This fraction generally varies from 20 % to 60 % based on the geometry of the element [1]. This is not an issue for the case of Fig. 4.3a because SFM ensure contact (Fig. 4.4a). However, the reduction of the shell contact thickness might lead to interpenetration or inaccurate contacts in case of using cohesive elements when they are deleted (Fig. 4.3b). This can be avoided by using SFM as shown in Fig. 4.4b to ensure normal contact when the cohesive element are deleted.

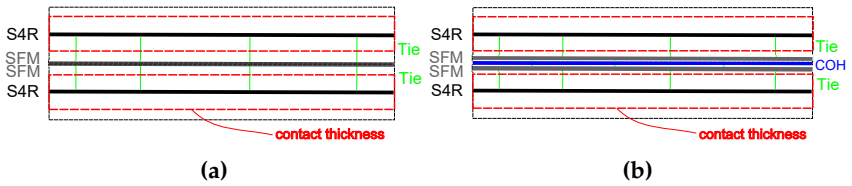

Fig. 4.4: (a) Sketch of modeling strategy with conventional shell elements (S4R) linked with surface elements (SFM) or (b) zero-thickness cohesive elements (COH3D8) through tie constraints for correct kinematic description of delamination when contact thickness reduction occurs.

The finite element type and the cohesive interaction technologies considered in the benchmark are summarized in Table 4.1. Abaqus built-in finite element (i.e. solid, continuum shell and conventional shell) and cohesive interaction technologies (i.e. zero-thickness cohesive elements and cohesive surfaces). SFM are used in the case *S4R CON* exactly as done in González et al. [67] in which it is recommended to leave a small gap (i.e. 1% of ply thickness) between SFM elements to allow better contact description. This is actually a recommendation that improves contact description to any contact problem, especially when using conforming meshes.

For the selected element size, which is discussed in Section 4.3.4, the general contact algorithm scales shell contact thickness due to the in-plane size (i.e. 0.5 mm) to thickness (i.e. 0.725 mm) ratio used. Thus, SFM are needed in the *S4R COH* case to guarantee correct contact when the cohesive elements are deleted.

Case	FE type	Interaction type	Strategy
SC8R CON	Continuum shell (SC8R)	Cohesive surfaces	Fig. 2.3c
SC8R COH	Continuum shell (SC8R)	Zero-thickness cohesive elements (COH3D8)	Fig. 2.3b
C3D8R CON	Solid (C3D8R)	Cohesive surfaces	Fig. 2.3c
C3D8R COH	Solid (C3D8R)	Zero-thickness cohesive elements (COH3D8)	Fig. 2.3b
S4R CON	Conventional shell (S4R)	Cohesive surfaces	Fig. 4.4a
S4R COH	Conventional shell (S4R)	Zero-thickness cohesive elements (COH3D8)	Fig. 4.4b

Table 4.1: Modeling strategies studied in the numerical benchmark.

4.3.2 Intralaminar damage modeling

The CDM model proposed by Maimí et al. [101, 102] is used to model the intralaminar damage. It is a thermodynamic consistent model with physically based damage activation functions [49] that is fed from experimental tests at the lamina level. The model assumes plane stress conditions and its predictive capability has been proved under different loading conditions [65, 98, 102]. In-plane isotropic plasticity with linear hardening has been included as shown in Fig. 4.5 to take into account the matrix dominant behaviour under shear loading. In addition, the fiber damage evolution can be defined based on the fiber traction or compression separation law (see Fig. 4.6).

The model is used through a user-written subroutine (VUMAT) in

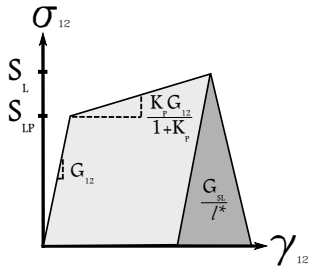

Fig. 4.5: In-plane shear stress - strain constitutive response with uncoupled linear hardening and linear softening damage. The parameters G_{12}, S_L, S_{LP}, K_P, G_{SL} and l^* are the shear elastic modulus, the shear strength, the yield stress, the hardening plastic parameter, the shear fracture toughness and the characteristic element length, respectively.

Abaqus/ Explicit [1]. Four surfaces for damage activation are defined as $F_N = \phi_N - r_N \leqslant 0$. Each damage activation function (F_N) accounts for one damage mechanism: longitudinal ($N = X_T$) and transverse ($N = Y_T$) tension, longitudinal ($N = X_C$) and transverse compression ($N = Y_C$). The loading functions (ϕ_N) depend on the effective stresses and material properties. The internal variables (r_N) set the maximum value that the loading functions can achieve before damage propagation. They are equal to one while the material is undamaged. When the loading functions are larger than one, damage begins and the internal variables are updated to the new damage threshold. Additionally, the yield function to account for plasticity under shear loading is defined by $F_P = |\gamma_{12}^e| - K_P\gamma_{12}^i - S_{LP}/G_{12} \leqslant 0$, where γ_{12}^e, S_{LP}, G_{12}, K_P, γ_{12}^i are the elastic shear strain, the yield stress, the shear elastic modulus, a plastic parameter and the isotropic hardening variable, respectively.

The damage activation functions are based on the LARC03 failure criteria [49] but neglecting the out-of-plane stresses, which are assumed small to induce damage. The *in situ* strengths for transverse tensile and compression are approximated by the analytical expressions from Camanho et al. [34] and Maimí et al. [103], respectively. The *in situ* shear strengths from [34] were adapted to the linear elasto-plastic behaviour considered in the constitutive model for the sake of consistency. Eqs. (4.1) - (4.3) are the *in situ* shear strength for a thick ply ($S^{is}_{L_{thick}}$), for a thin ply ($S^{is}_{L_{thin}}$) and for an outer thin ply ($S^{is}_{L_{out}}$), respectively.

$$S^{is}_{L_{thick}} = \frac{\sqrt{(K_P+1)(2S_L^2K_P + 2S_L^2 - S_{LP}^2)}}{K_P+1} \tag{4.1}$$

$$S^{is}_{L_{thin}} = \frac{\sqrt{h_{ply}(K_P+1)(\pi S_{LP}^2 h_{ply} + 8G_{12}G_{SL}K_P)}}{(K_P+1)h_{ply}\sqrt{\pi}} \tag{4.2}$$

$$S^{is}_{L_{out}} = \frac{\sqrt{h_{ply}(K_P+1)(\pi S^2_{LP} h_{ply} + 4G_{12}G_{SL}K_P)}}{(K_P+1)h_{ply}\sqrt{\pi}} \tag{4.3}$$

where h_{ply} is the ply thickness. The *in situ* strength of an embedded ply ($S^{is}_{L_{emb}}$) is the maximum of Eqs. (4.1) - (4.2).

A benchmark is done with different finite element and interaction technologies to compare their performance in which 3-D solid elements are used. The constitutive model is adapted to be used with 3-D solid elements through defining the damage variables d_3, d_4 and d_5 as a function of other damage variables as done in previous works [65,98,99]:

$$d_3(r_{XC}, r_{YC}) = 1 - [1 - d_1(r_{XC})][1 - d_2(r_{YC})] \tag{4.4}$$

$$d_4(r_{YT}) = d_6(r_{YT}) \tag{4.5}$$

$$d_5(r_{XT}) = d_1(r_{XT}) \tag{4.6}$$

The damage variables (d_N) depend on the elastic and fracture properties as well as on the traction separation law shape. Dávila et al. [50] found that a linear traction separation for fiber damage was insufficient to predict the initiation and propagation of damage in cross-ply Compact Tension (CT) specimens. Multiple damage mechanisms occur during the fracture of a composite laminate (e.g. fiber - bridging, fiber pull - out), which are embedded within the traction separation law at the macro-scale level. Matrix related damage mechanisms usually have a relatively small FPZ in comparison with the specimen size in conventional composite laminates, while the FPZ related to fiber damage mechanisms can span several millimeters [37,39]. For these reasons, the model assumes bi-linear softening for the longitudinal directions and linear softening for the transverse and shear directions (see Fig. 4.6). The damage evolution is controlled by the traction separation law shape parameters f_{X_M} and H_{X_M} (see Fig. 4.6) together with the strengths (i.e. X_M, Y_M, S_L) and fracture toughness (i.e. G_{X_M}, G_{Y_M}, G_{SL}). The traction separation law can be obtained from CT and Compact Compression (CC) tests according to the method from [121,122]. Alternatively, it can be approximated by fitting the shape to the load displacement curve of the CT and CC test through FEA.

The intralaminar properties of the AS4/8552 carbon-epoxy UD pre-preg used in González et al. [65] are summarized in Table 4.2. González et al. [65] tested the ply elastic properties (i.e. $E_1; E_2; G_{12}; \nu_{12}; \nu_{23}$) and ply strengths (i.e. $X_T; Y_T; S_L$) with the same pre-preg roll of the specimens used for the experimental LVI and CAI tests according to test standard from the ASTM [15,18,19]. The remaining strength properties (i.e. $Y_C; X_C$) were taken from Lopes et al. [98] in which the same material system was used. The fracture toughness properties (i.e. G_{X_T} ; G_{X_C} ;G_{Y_T} ; G_{Y_C} ; G_{S_L}) were not tested and they were taken from IM7/8552 data [35]. Camanho et al. [35] used interlaminar tests to determine mode I fracture toughness (G_{Y_T} =G_{Ic}) [21] and

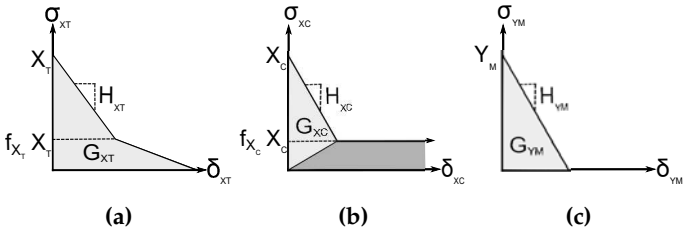

Fig. 4.6: Sketch of the bi-linear traction separation law shape used for (a) fiber tension, (b) fiber compression and (c) transverse and shear damage evolution where M = T, C. Stress vs. opening displacement.

mode II (G_{S_L} =G_{IIc}) [105] while the proposed test methods (i.e. CC and CT) by Pinho et al. [129] were used to obtain the fiber fracture toughness. The expoxy resin Hexply 8552 tested was the same in [35] but not the carbon fibers. The energy dissipated through fiber breakage in the considered LVI test should be small compared to other damage mechansims. Thus, the fact that the fiber fracture toughness was taken from another material system should have a small effect. No plasticity was considered as in González et al. [65]. No experimental data was available to feed the fiber traction separation law shape. Thus, the longitudinal tensile law was selected so as to resemble the linear-exponential damage evolution used in González et al. [65] while the longitudinal compression was a bi-linear law with a plateau that represents the experimentally observed crushing stress as proposed by other authors [53, 59, 77, 136]. The compression fracture toughness before crushing is G_{X_C} = 106.3 N/mm, which is the area beneath the first branch of Fig. 4.6b.

Density	1.59×10^{-9} t/mm^3
Elastic properties	E_1 = 128000 MPa ; $E_2 = E_3$ = 7630 MPa
	G_{12} = 4358 MPa ; ν_{12} = 0.35 ; ν_{23} = 0.45
Strength	X_T = 2300 MPa ; X_C = 1531 MPa
	Y_T = 26 MPa ; Y_C = 199.8 MPa
	S_L = 78.4 MPa
Fracture toughness	G_{X_T} = 81.5 N/mm ; G_{X_C} = 106.3 N/mm
	G_{Y_T} = 0.28 N/mm ; G_{Y_C} = 1.31 N/mm
	G_{S_L} = 0.79 N/mm
Traction separation law parameters	f_{X_T} = 0.1 ; f_{X_C} = 0.1
	H_{X_T} = 48681 N/mm^3; H_{X_C} = 9922.7 N/mm^3

Table 4.2: Material properties and model parameters of Hexply AS4/8552 used [65] for the intralaminar damage model.

The *in situ* strength are summarized in Table 4.3. They are defined according to [34, 103], Eqs. (4.1) - (4.3) and the material properties from Table 4.2. It

is worth noting that the formula are meant for lamina that are perpendicular to each other. A different mismatch angle between plies affects the actual *in situ* effect and the formulae do not account for that.

Ply location	h_{ply} [mm]	Y_T^{is} [MPa]	Y_C^{is} [MPa]	S_L^{is} [MPa]
Outer plies	0.725	38.75	199.8	78.4
Embedded plies	0.725	61.23	199.8	78.4
Embedded (symmetry) plies	1.45	43.32	199.8	78.4

Table 4.3: *In situ* strength for the intralaminar damage model.

4.3.3 Interlaminar damage modeling

The built-in CZM from Abaqus/Explicit [1] is used here as interlaminar damage model. It allows to compare the performance of both cohesive interaction technologies considered in the numerical benchmark using exactly the same CZM implementation. The model has an unilateral behaviour for mode I crack propagation in order to account for crack closure and a scalar damage variable is used to ensure irreversibility of the damage process. The damage evolution is controlled through the cohesive law shape which is assumed with linear softening. It is considered a quadratic traction criterion for damage initiation and the Benzeggagh-Kenane (B-K) criterion [27] for damage propagation, which are generally accepted criteria under mixed mode loading.

Turon et al. [156] demonstrated that changes in the local mode ratio during the evolution of damage under mixed-mode loading might cause errors in the energy dissipation calculation. To solve this issue, it was proposed a relationship between interlaminar strengths and fracture toughness. However, this relationship cannot be derived for the used CZM due to the lack of details on the employed formulation.

The interlaminar material properties used from González et al. [65] are summarized in Table 4.4.

G_{Ic} [N/mm]	G_{IIc} [N/mm]	τ_{Ic} [MPa]	τ_{IIc} [MPa]	η
0.28	0.79	26	78.4	1.45

Table 4.4: Interface material properties of Hexply AS4/8552 [65].

Penalty stiffness

Cohesive elements or cohesive surfaces are commonly used to model delamination. The thickness of the cohesive element should be fairly small

to represent the actual resin reach interface where delamination takes place among plies. In fact, it is typically assumed to be negligible. This assumption is very convenient for explicit analyses to avoid affecting the STI. However, zero-thickness cohesive element or cohesive surface lead to the definition of a penalty stiffness value. The penalty stiffness can affect the accuracy but also the computational performance through the STI (see Eq. (2.2)).

The penalty stiffness could be seen as spring series in which the equivalent stiffness of the system is:

$$\frac{1}{E_{eq}^{coh}} = \sum_{n=1}^{n_{plies}} \frac{h_i}{E_i} + \sum_{n=1}^{n_{int}} \frac{1}{K_i} \tag{4.7}$$

and E_{eq}^{coh} should approach to the equivalent stiffness of the system without cohesive elements E_{eq}:

$$\frac{1}{E_{eq}} = \sum_{n=1}^{n_{plies}} \frac{h_i}{E_i} \tag{4.8}$$

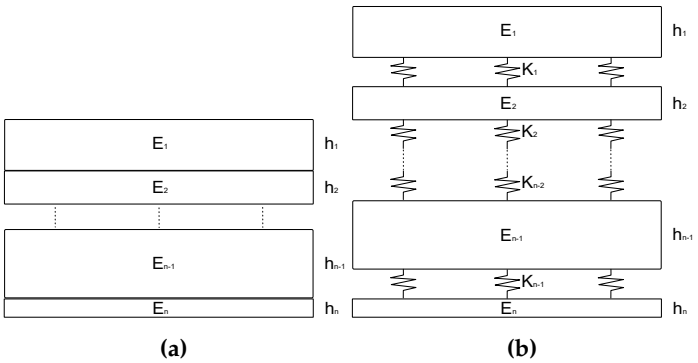

Fig. 4.7: a) System without cohesive elements and b) with cohesive elements.

The penalty stiffness value depends on the number of interfaces considered, the elastic properties of the surrounding plies but also on the loading conditions. The loading conditions make difficult to have a general closed-form expression for the penalty stiffness value. Instead, a sensitivity analysis can be done in the elastic regime to choose the minimum penalty stiffness value that converges to the same elastic response. Thus, compliance is not added into the model while the detrimental effect on the STI is mittigated. It is also worth noting that the penalty stiffness should have the same value for mode I and mode II to avoid changes in the local mode ratio under mixed-mode conditions unless a consistent formulation is used [159].

A sensitivity analysis on the effect of the penalty stiffness value was done to obtain an optimum value. Fig.4.8 shows little effect on the elastic response for penalty stiffness values larger than 2.5×10^4 N/mm^3.

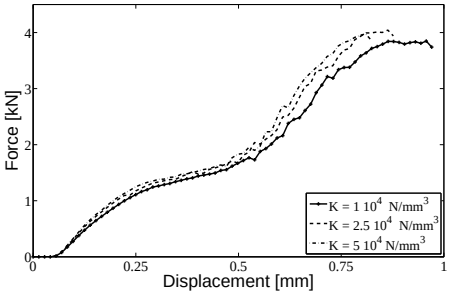

Fig. 4.8: Sensitivity analysis of the penalty stiffness ($K = K_n = K_{coh}$) value on the elastic response.

SFM surface density

The strategy described in Fig. 4.3a (Section 4.3.1) that combines conventional shell elements with cohesive surfaces by means of SFM requires the definition of a density by unit surface ($\bar{\rho}_{sfm}$). Their mass can not be zero within an explicit FEM framework because in a dynamics system all the nodes need inertia and mass terms. SFM surface density ($\bar{\rho}_{sfm}$) can be defined by distributing the mass of the laminate through the elements in order to maximize the STI of the model while keeping its mass.

The density by unit surface ($\bar{\rho}_{sfm}$) of SFM is defined as:

$$\bar{\rho}_{sfm} = \frac{f_{sfm}\rho h_{lam}}{2(n_{int}+1)} \tag{4.9}$$

where $0 < f_{sfm} < 1$, ρ is the actual material density, n_{int} is the number of interfaces for delamination modeled and h_{lam} is the laminate thickness.

The density of conventional shell elements is modified (ρ_{mod}) to keep the total mass of the system:

$$\rho_{mod} = \rho(1 - f_{sfm}) \tag{4.10}$$

The optimum mass distribution factor (f_{sfm}) in case of using continuum and SFM elements is obtained by equaling Eqs. (2.1) - (2.2):

$$\frac{\triangle t_{elem}}{\triangle t_{int}^{coh}} \simeq 1 \tag{4.11}$$

Nevertheless, contact can also occur between SFM and shell elements unless shell contact thickness is scaled down. Thus, the model STI can be also

controlled by the contact STI ($\triangle t_{int}^{con}$). In that case, the optimum mass distribution factor (f_{sfm}) should be obtained by equaling Eqs. (2.2) - (2.3):

$$\frac{\triangle t_{int}^{con}}{\triangle t_{int}^{coh}} \simeq 1 \tag{4.12}$$

The factor (f_{sfm}) which maximizes the STI using the same cohesive and contact penalty stiffness values ($K = K_{coh} = K_n$) is the lowest f_{sfm} obtained from Eqs. (4.11) - (4.12).

$$f_{sfm} = \min\left(\frac{2(n_{int}+1)K(l^*\alpha)^2}{2(n_{int}+1)K(l^*\alpha)^2 + Eh_{lam}}, \frac{2(n_{int}+1)h_{elem}^{min}}{2(n_{int}+1)h_{elem}^{min} + h_{lam}}\right) \tag{4.13}$$

where E is the maximum component of the constitutive tensor, and $\alpha = \sqrt{1+\zeta^2} - \zeta$ with ζ being the fraction of critical damping that prevent finite elements from ringing or even collapsing in the highest element frequency [1]. l^* is the characteristic element length, which is related to the shortest finite element length. n_{int} is the number of interfaces for delamination modeled, h_{elem}^{min} the minimum element thickness modeled and h_{lam} is the laminate thickness.

It is worth to keep in mind that SFM are not needed for volumetric elements. In case of using SFM in combination with zero-thickness cohesive elements due to shell contact thickness reduction see Eqs. (4.17) - (4.20).

Zero-thickness cohesive elements surface density

Similarly to SFM, zero-thickness cohesive elements have no volume but within an explicit FEM all the nodes need inertia and mass terms. Zero-thickness cohesive elements surface density ($\bar{\rho}$) is also defined by distributing the mass of the laminate through the elements (i.e. continuum and cohesive elements) in order to maximize the STI of the model while keeping its mass. It is worth noting that this can be applied to any kind of continuum element such as solid and continuum shell elements.

The density by unit surface ($\bar{\rho}_{coh}$) of the zero-thickness cohesive elements is defined as:

$$\bar{\rho}_{coh} = \frac{f_{coh}\rho h_{lam}}{n_{int}} \tag{4.14}$$

where $0 < f_{coh} < 1$, ρ is the actual material density, n_{int} is the number of interfaces for delamination modeled and h_{lam} is the laminate thickness.

The modified continuum element density (ρ_{mod}) is defined to keep the total mass of the system as:

$$\rho_{mod} = \rho(1 - f_{coh}) \tag{4.15}$$

The optimum mass distribution factor (f_{coh}) in case of using continuum and zero-thickness cohesive elements is obtained from Eq. (4.11).

Nevertheless, contact is also considered in LVI simulations to avoid interpenetration and to account for friction effects. Thus, the model STI can be controlled by the contact STI ($\triangle t_{int}^{con}$). In that case, the optimum mass distribution factor (f_{coh}) should be obtained from Eq. (4.12).

The factor (f_{coh}) which maximizes the STI with same penalty stiffness values ($K = K_{coh} = K_n$) is the lowest f_{coh} obtained from Eqs. (4.11) - (4.12).

$$f_{coh} = \min\left(\frac{n_{int}K(l^*\alpha)^2}{n_{int}K(l^*\alpha)^2 + Eh_{lam}}, \frac{n_{int}h_{elem}^{min}}{n_{int}h_{elem}^{min} + h_{lam}}\right) \tag{4.16}$$

elements from ringing or even collapsing in the highest element frequency [1]. l^* is the characteristic element length, which is related to the shortest finite element length. n_{int} is the number of interfaces for delamination modeled, h_{elem}^{min} the minimum element thickness modeled and h_{lam} is the laminate thickness.

In the strategy from Fig. 4.4b the mass distribution is among cohesive elements, SFM and continuum elements. The modified continuum element density (ρ_{mod}) is defined to keep the total mass of the system as:

$$\rho_{mod} = \rho(1 - f_{coh} - f_{sfm}) \tag{4.17}$$

$$f_{sfm} = \frac{2(n_{inter} + 1)(1 - f_{s4r})}{3n_{inter} + 2} \tag{4.18}$$

$$f_{s4r} = \frac{Eh_{lam}}{2K(l^*\alpha)^2(n_{inter} + 1) + Kn_{inter}(l^*\alpha)^2 + Eh_{lam}} \tag{4.19}$$

$$f_{coh} = \frac{n_{int}f_{sfm}}{2(n_{int} + 1)} \tag{4.20}$$

The density by unit surface of the cohesive elements ($\bar{\rho}_{coh}$) and SFM ($\bar{\rho}_{sfm}$) are defined by Eq. (4.14) and Eq. (4.9), respectively.

Table 4.5 summarizes the densities employed for all the cases considered in the numerical benchmark.

4.3.4 Element size

The element size of the model is important to ensure correct intralaminar and interlaminar energy dissipation.

CDM should avoid snap-back at the element level for correct intralaminar energy dissipation even though a mesh regularization algorithm is used as previously done by some authors [65,67,98,99,154]. In fact, snap-back should

Case	ρ_{mod} [t/mm^3]	$\bar{\rho}_{sfm}$ [t/mm^2]	$\bar{\rho}_{coh}$ [t/mm^2]
SC8R CON	1.59×10^{-9}	-	-
SC8R COH	1.52×10^{-9}	-	6.42×10^{-11}
C3D8R CON	1.59×10^{-9}	-	-
C3D8R COH	1.52×10^{-9}	-	6.42×10^{-11}
S4R CON	1.44×10^{-9}	6.08×10^{-11}	-
S4R COH	1.38×10^{-9}	5.85×10^{-11}	5.85×10^{-11}

Table 4.5: Optimized densities employed in the numerical benchmark.

be avoided within the first branch of the traction separation law because of its importance on the structural strength [88,89,104]. The maximum element size is assessed for each damage mechanism (N) to avoid snap-back within the first branch of the traction separation law by Eq. (4.21) [106].

$$l^* \leqslant \frac{E_N}{H_N} \tag{4.21}$$

where l^*, E_N and H_N are the characteristic element length, the elastic modulus, and the first branch slope of the traction separation law for a given damage mechanism (N), respectively. In the case of a linear softening law $H_N = X_N^2/2G_N$.

The interlaminar mesh discretization has to be chosen according to the interlaminar FPZ size. In Chapter 3 was shown that the damage initiation and propagation are not correctly computed if the FPZ is not properly discretized. It was confirmed that 3 elements along the FPZ are enough for correct interlaminar damage predictions. Some LVI studies [65,87,154] used the formula proposed by Rice [135] to estimate the interlaminar FPZ. Nevertheless, the expression was derived for infinite specimens under mode II fracture mode. Thus, it can provide an over-prediction of the actual FPZ. A conservative estimation of the interlaminar FPZ can be obtained by using the Eqs. (3.7) - (3.8) from Chapter 3 and considering the smallest ply thickness modeled.

Table 4.6 shows the maximum element size for each damage mechanism based on Eq. (4.21). Based on the properties from Table 4.4 and considering a ply thickness of 0.725 mm the interlaminar FPZ for pure fracture mode I and mode II are 0.73 mm and 2.06 mm according to Eqs. (3.7) - (3.8), respectively. The actual interlaminar FPZ measured in the LVI and CAI models were approximately 2 mm and 1.5 mm, respectively. LVI is mainly governed by mode II delamination while CAI has mode mixity what reduces the interlaminar FPZ in comparison of LVI.

Damage mechanism	Maximum element size [mm]
X_T	2.63
X_C	12.9
Y_T	1.14
Y_C	0.5
S_L	1.1

Table 4.6: Maximum intralaminar element size for each damage mechanism.

The chosen element size for the coarse region is 5 mm while 0.5 mm for the refined region was 0.5 mm. Thus, correct intralaminar and interlaminar energy dissipation is ensured.

4.3.5 Element deletion criterion

Excessive element distortion issues, which can eventually abort the simulation, are common in FEA that involve severe damage as LVI, CAI or crash simulations. This aspect can compromise the accuracy and robustness of the numerical models.

The damage variable usually depends on the material properties, the traction separation law shape and the element size in case of using a regularization procedure such as the crack band model [26]. Therefore, special attention must be paid on the selected damage variable for element deletion because the energy dissipated could be far from the actual material fracture toughness. If the element is not deleted but the damage variable is limited to grow to a too low value the global response can be affected because the remaining element stiffness absorbs elastic energy. Furthermore, the residual stresses actually translate into a permanent bridging mechanism behind the crack tip which affects the crack progression.

In the numerical benchmark, the continuum elements are deleted when the fiber damage variable is equal to one in order to dissipate the total fracture energy. The cohesive elements are also deleted when the damage variable is equal to one. However, matrix degradation has to be controlled to avoid element distortion issues. Different approaches were considered without success (i.e. maximum strains, strain rate, strain gradient). Finally, the criterion adopted is to define a residual stiffness for the matrix (E_r). The matrix damage variables are limited (i.e. d_2=0.987 , d_6=0.977) so that the matrix never has a stiffness lower than 100 MPa (e.g. $E_r = (1 - d_2)E_2$ = 100 MPa).

4.4 Results and discussion

The most relevant numerical results from the LVI and CAI numerical benchmark are presented in this section. They are presented together with the experimental data. Furthermore, sensitivity analyses are presented to study the effect of the mass distribution for STI optimization and the matrix damage variable threshold.

4.4.1 LVI and CAI results

The force - displacement and the energy absorbed by the plate is compared among the different finite element types and cohesive interaction technologies with the experimental results in Figs. 4.9 - 4.10, respectively. Table 4.7 compares the numerical results with the experimental ones in terms of delamination threshold (F_d), maximum force (F_{max}), maximum displacement (U_{max}), energy dissipated (E_{dis}), projected delamination area (A_d) and CAI strength (F_{CAI}).

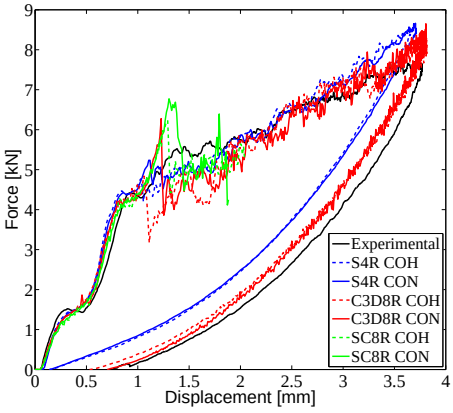

Fig. 4.9: Comparison of the force - displacement response for different finite element types and cohesive interaction technologies.

The elastic regime and delamination threshold is well predicted by all the cases with relative differences below 5 %. However, conventional shell elements show a stiffer response when compared with solid and continuum shell elements because they do not account for out-of-plane compliance. The maximum displacement is close to the experimental one for all the cases with differences below 3 %. However, larger differences in the prediction of the maximum force are found. All the models tend to over-predict the maximum force about 10 %. Differences among modeling strategies are found

for the predicted dissipated energy and projected delamination area. These predictions are more influenced for the chosen element type rather than the cohesive interaction technology. For instance, conventional shell elements under-predict the dissipated energy about 27.3 % while solid elements 15.8 %. This could be due to the fact that conventional shell elements do not account for out-of-plane stresses, which is more relevant for thick plies than in standard ply thickness. The continuum shell element suffered from numerical issues which stopped prematurely the simulations regardless the interaction technology. Only for large residual stiffness values (i.e. $E_r = (1 - d_2)E_2$ = 400 MPa) the simulations could be finished.

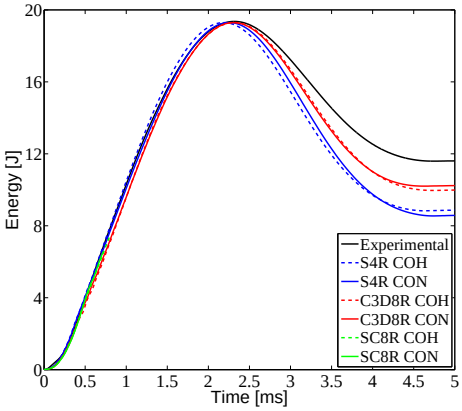

Fig. 4.10: Comparison of the energy absorbed among different finite element types and cohesive interaction technologies.

The projected delamination area obtained using zero-thickness cohesive elements and cohesive surfaces are shown in Figs. 4.11 - 4.12, respectively. Conventional shell elements over-predict the projected delamination area by 25 % (i.e. *S4R CON*) and 14 % (i.e. *S4R COH*) while solid elements are in better agreement with the experimentally obtained (i.e. 3 %). However, it is worth noting that the *S4R CON* was able to predict the largest delamination that occurred in the 45º direction at the back - face. This could be explained by the fact that conventional shell elements correctly capture bending with only one element per ply and cohesive surfaces are able to better capture large displacements than cohesive elements.

The CAI experimental test used the displacement measurement from the machine. Thus, the CAI set-up added some compliance, which was corrected as done in [50]. The CAI force - displacement response is shown in Fig. 4.13. All the modeling strategies considered predict rather accurately the experimental CAI strength. Relative errors of -3.6 %, 2.2 %, -3.6 % and -1.9

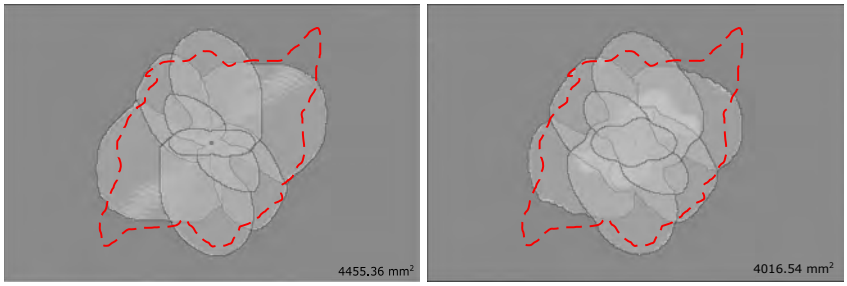

Fig. 4.11: (a) Projected delamination area of conventional shells and (b) solid elements with zero-thickness cohesive elements. The experimental projected delamination area is the dashed line.

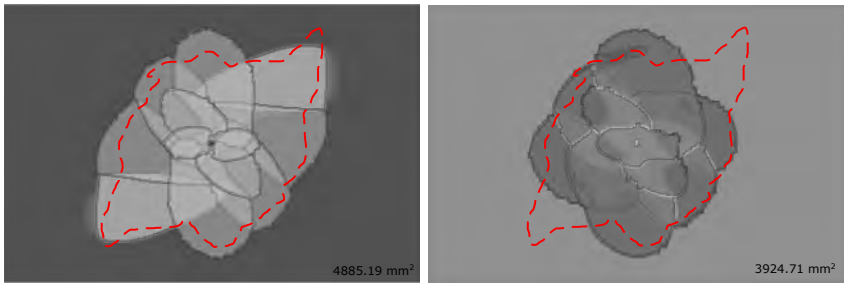

Fig. 4.12: (a) Projected delamination area of conventional shells and (b) solid elements with cohesive contact surfaces. The experimental projected delamination area is the dashed line

% were obtained for *S4R COH*, *S4R CON*, *C3D8R COH* and *C3D8R CON*, respectively. The initial stiffness is well captured for all the cases. However, solid elements show a loss of stiffness before failure due to delamination propagation.

The computational times for each finite element type and cohesive interaction technology during the LVI and CAI simulation are summarized in Table 4.8. The theoretical STI and the actually computed STI by Abaqus are very close. However, it can be seen that there is a small knock-down factor used by the software. The features of the computer used are: two socket work station (ASUS Z10PE-D16WS Motherboard), with two CPU Intel Xeon Processor E5-2687Wv3 with 3.1 GHz CPU frequency (10 cores, 160W power, and 2133 DDR4 type memory); solid-state disc of 512 GB and 32 GB RAM for each CPU. All the simulations were computed using 20 CPU's.

The LVI simulation time of conventional shell elements with zero-thickness cohesive elements were 1.54 times faster than using them with cohe-

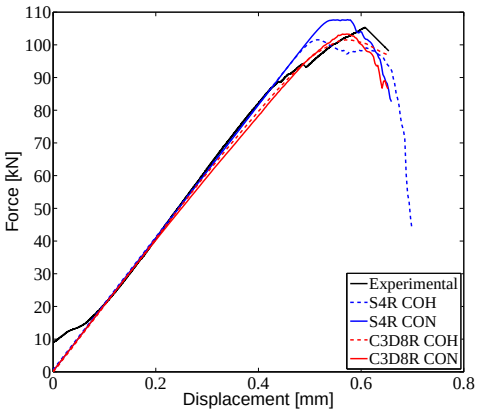

Fig. 4.13: Comparison of the force - displacement CAI results for different finite element types and interaction technologies.

Case	F_d [kN]	F_{max} [kN]	U_{max} [mm]	E_{dis} [J]	A_d [mm^2]	F_{CAI} [kN]
Experimental	4.41	7.74	3.72	12.03	3898.3	105.32
S4R CON	4.41	8.66	3.66	8.58	4885.19	107.7
S4R COH	4.46	8.65	3.64	8.87	4455.36	101.54
C3D8R CON	4.2	8.65	3.81	10.23	3924.71	103.29
C3D8R COH	4.2	8.34	3.81	9.99	4016.54	101.51
SC8R CON	4.15	-	-	-	-	-
SC8R COH	4.25	-	-	-	-	-

Table 4.7: Comparison of experimental and numerical results in terms of delamination threshold (F_d), maximum force (F_{max}), maximum displacement (U_{max}), energy dissipated (E_{dis}), projected delamination area (A_d) and CAI strength (F_{CAI}) for the studied cases.

sive surfaces. Similarly, solid elements with zero-thickness cohesive elements were 1.3 times faster than using them with cohesive surfaces. Nevertheless, larger differences in the computational time are found depending on the element type. Conventional shell elements were up 3.3 times faster than solid elements in the case of using zero-thickness cohesive elements. In fact, the simulation time difference between solid elements and conventional shells should be larger because selective element mass scaling was applied for STI lower than 1×10^{-8} s in order to finish the simulations of solid elements in a reasonable time (see Fig. 4.14).

Table 4.8 shows that solid and continuum shell elements have a larger initial STI than conventional shell elements. However, the computational time of conventional shell elements is the lowest. Conventional shell elements

Case	Theoretical initial STI [s]	Computed initial STI [s]	LVI CPU time [h]	CAI CPU time [h]
S4R COH	4.79×10^{-8}	4.51×10^{-8}	13	5.5
S4R CON	4.9×10^{-8}	4.75×10^{-8}	20	13
C3D8R COH	5.07×10^{-8}	4.73×10^{-8}	43	23
C3D8R CON	5.18×10^{-8}	5.01×10^{-8}	56	28
SC8R COH	5.07×10^{-8}	4.73×10^{-8}	Not finished	Not done
SC8R CON	5.18×10^{-8}	4.99×10^{-8}	Not finished	Not done

Table 4.8: Comparison of the initial STI and computational time required for the LVI and CAI numerical simulation for different finite element types and cohesive interaction technologies.

were also faster than continuum shell elements before the simulation aborted. This happens because they have a simpler constitutive behaviour but also because their STI is less affected during the simulation. Volumetric finite elements suffer more element distortion than plane elements as shown in Fig. 4.14. It is worth noting that in the studied case the element STI was controlled by the in-plane finite element size while for standard ply thickness the STI is often controlled by the ply thickness. Thus, the computational benefit of using conventional shell elements in situations where the element thickness is controlling the model STI will be larger.

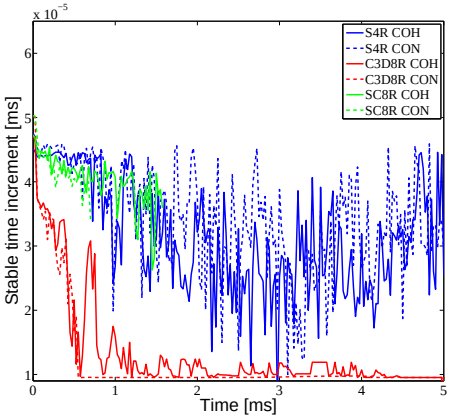

Fig. 4.14: Comparison of the STI evolution during the LVI among different finite element types and cohesive interaction technologies.

4.4.2 Effect of mass distribution for STI optimization

The effect of the mass distribution effect for STI optimization is analyzed in terms of accuracy and computational effort. Different mass distributions could affect the inertia of the system. However, the results are not affected because the actual mass of the system is always kept and composite thickness is usually small. The *S4R CON* case is analyzed for three different mass distribution factors (f_{sfm}); the optimum one (i.e. 0.094), 0.5 and 0.9. Fig. 4.15 compares the force-displacement and the force-time response.

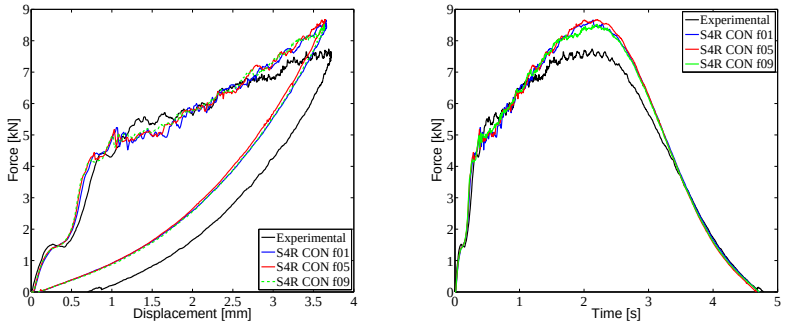

(a) **(b)**

Fig. 4.15: (a) Mass distribution effect on the force-displacement and b) force-time response prediction. *S4R CON*.

Table 4.9 compares the initial STI and the computational time for the different studied cases.

Case	f_{sfm}	ρ_{mod} [t/mm^3]	$\bar{\rho}_{sfm}$ [t/mm^2]	Computed initial STI [s]	LVI CPU time [h]
S4R CON 01	0.094	1.44 10^{-9}	6.08 10^{-11}	4.51 10^{-8}	29
S4R CON 05	0.5	7.95 10^{-10}	2.88 10^{-10}	3.52 10^{-8}	41.5
S4R CON 09	0.9	1.59 10^{-10}	5.19 10^{-10}	1.58 10^{-8}	157.5

Table 4.9: Comparison of the initial STI, modified density and computational time required for the case *S4R CON* depending on the mass distribution factor (f_{sfm}).

4.4.3 Effect of element deletion criterion

Fig. 4.16 shows the effect of the residual stiffness for the matrix value (E_r) on the LVI and CAI response.

The results from Figs. 4.16 - 4.17 are for the *S4R COH* case. It can be seen that for a residual stiffness for the matrix lower than 200 MPa the LVI and CAI results converge to similar results. Fig. 4.17 shows the STI evolution

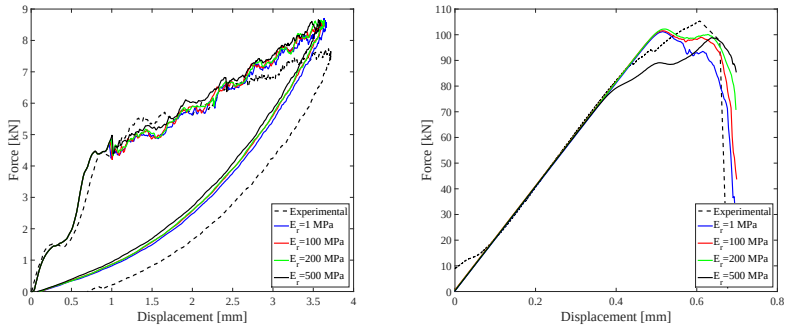

Fig. 4.16: (a) Effect of the residual stiffness for the matrix on the LVI and b) CAI force - displacement response. *S4R COH*.

during the LVI simulation depending on the matrix residual stiffness. The lower the residual stiffness the lower the STI during the LVI due to element distortion. In fact, the STI for E_r = 500 MPa is fairly constant throughout the LVI simulation due to the low element distortion allowed.

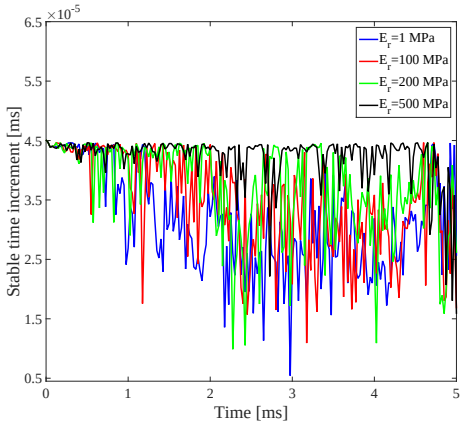

Fig. 4.17: Effect of the residual stiffness for the matrix on the STI evolution during the LVI simulation. *S4R COH*.

4.4.4 Effect of mesh orientation

As mentioned before, the models were not sensitive to finite element mesh orientation. Fig. 4.18 shows that there is no effect due to mesh orientation on the force-displacement response. Delamination is the main damage mech-

anism here. Probably, mesh orientation effect would be more noticeable if fiber breakage was present. Fiber damage ususally involves more energy dissipation than matrix cracking or delamination. Thus, it could be expected that little differences due to mesh orientation could have a larger impact on the results.

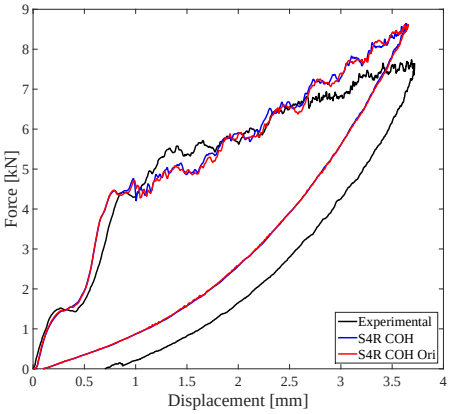

Fig. 4.18: Mesh orientation effect on the force-displacement prediction.

4.5 Conclusions

A methodology to perform LVI and the sequential CAI was proposed. Numerical impact models require the definition of several parameters that affect their efficiency, accuracy, robustness and objectivity. The key parameters were described concisely and the selected values have been well justified as well as their sensitivity discussed. Especial attention has been devoted towards definitions that affect the computational performance such as the penalty stiffness, the surface density of cohesive interactions, the finite element type, and the cohesive interaction technology.

The methodology was applied at the coupon level for an impact energy that falls within the range of BVID with the aim to systematically study the computational performance and numerical predictions among different finite element types and cohesive interaction technologies. A laminate with unusually thick plies was selected to highlight possible limitations of plane stress based finite elements. The use of conventional shell elements together with zero-thickness cohesive elements proved to be the fastest approach with relative errors on the CAI strength below 4 %. However, conventional shell elements were less accurate in the LVI energy dissipation prediction than solid elements. They neglect the of out-of-plane stress, which are important for

damage predictions in thick ply laminates, and they have poorer transverse shear description.

Furthermore, it was discussed the importance of the element deletion criterion. It is an aspect that can affect the accuracy, computational performance and robustness of the models. Element distortions are mainly controlled by matrix damage which easily lead to large element distortion during impact simulations. For this reason, the criterion adopted is based on leaving a residual stiffness for the matrix to avoid undesired matrix excessive deformations that eventually abort the simulations. Indeed, conventional shell elements proved to be the most robust finite element for the studied case allowing residual matrix stifness of 1 MPa. This is related to the fact that they suffer less element distortions.

Part III

Application, Results and Discussions

Chapter 5

LVI and CAI of thin ply laminates

5.1 Introduction

Spread-tow thin-ply technology [90] allows to commercially produce unidirectional and fabric thin ply laminae. The use of thinner laminae is aimed to produce thinner and lighter laminates but also with improved fiber orientation and uniformity, smoother ply drops and reduced crimp. It is also motivated by the enhancement of the damage resistance due to the *in situ* effect [34,56], which gains importance when reducing the ply thickness in multidirectional laminates. The *in situ* effect on conventional UD ply laminates has been demonstrated experimentally [30,40,125,143] and numerically [11,14].

A disadvantage of traditional fabric reinforced composites is the waviness of the fibers and resin rich pockets in the crimps, which results in lower in-plane stiffness and strength [28,165]. Spread-tow fabrics plies can have thinner and wider fiber bundles. These lead to a flatter fabric with lower crimp frequency and significantly smaller crimp angles. Thus, the void content and resin rich areas are considerably reduced and the mechanical properties improved in comparison with traditional fabric reinforced composites [58]. Textile based fiber reinforcements possess important features for their application in the aerospace and automotive industry. They have excellent drape that allows faster manufacturing process as liquid molding techniques and they offer cheaper manufacturing than UD conventional pre-impregnated plies because of their simpler handling and storage [10]. Furthermore, some authors recognizes textile fabrics with better impact [23,91] and delamination growth than conventional UD composites [6,91].

Thin ply laminates generally have better damage resistance and fatigue

life than conventional laminates because sub-critical damage mechanisms (e.g. matrix cracking, delamination) occurrence prior to ultimate laminate failure are reduced or delayed in many situations [8, 10, 147, 172]. However, it is known that they have a more brittle failure which can lead to earlier unstable failure in notched specimens under tensile loads (e.g. open hole tension) [10, 147]. Experimental evidence shows that laminates with thinner plies behave differently than those with thicker ones under impact loads [8, 137, 173] and indentation tests [163, 164]. In thin ply laminates, fiber breakage becomes more relevant while matrix cracking is reduced. It is thought that interlaminar stresses and fiber breakage induce delamination [137,164]. These observations are reported either for UD [137] and fabric thin ply laminates [164].

Numerical simulations can help in the understanding of the damage sequence of polymer based composite laminates during an impact event, which is a difficult experimental task when dealing with a large number of plies. Some works attempted to model thin ply laminates computationally [116,117]. However, they did not succeed in capturing the damage mechanisms to reproduce the experimental data. Olsson et al. [116,117] attributed the disagreement to the fact that only few interfaces for delamination were considered in the models. Olsson et al. [116,117] concluded that further work should focus on how the interaction between intralaminar and interlaminar damage can be accounted for in a sufficiently accurate and computationally efficient manner.

The aim of this chapter is to develop an efficient numerical model based on the methodology described in Chapter 4 to better understand the damage mechanisms and their sequence during the LVI and the CAI test of the experimentally tested spread-tow fabric composite material trademarked as TeXtreme® produced by Oxeon. Besides the impact and CAI tests, an extensive experimental campaign was conducted to characterize the material at the ply level.

5.2 Virtual test set-up

The models aim to reproduce the performed experimental LVI and CAI tests on TeXtreme® 80 g/m^2. The experimental drop weight impact tests were according to ASTM D7136 standard [16]. The tests were performed using a CEAST Fractovis Plus instrumented drop-weight tower, with a hemispherical impactor of 16 mm diameter and 5 kg, equipped with an automatic anti-rebound impactor system. The CAI tests were performed according to the standard ASTM D7137 [17] on a MTS Insight^{TM} Electromechanical tester with a 300 kN load cell. All the impacted specimens failed successfully during the CAI tests because they collapsed at the impacted zone.

5.2.1 Geometry and boundary conditions

The geometry and boundary conditions of the LVI model were previously sketched in Fig. 4.1. All the plies and interfaces were needed to be modeled for accurate results. Double symmetry boundary conditions could be considered to reduce the computational effort because the plies are modeled as homogeneous ply weave. However, some vibration and buckling modes would be omitted what was found to especially affect the CAI predictions.

The hemispherical impactor of 16 mm diameter and 5 kg is modeled with rigid elements (R3D4) with a maximum element size of 0.75 mm. An initial velocity in the out-of-plane direction is assigned to the impactor according to the impact energy tested. All the degrees of freedom are fixed with the exception of the out-of-plane displacement.

The specimen, which measures 150 x 100 mm^2, is placed over a flat support with a 125 mm by 75 mm rectangular cut-out. The support, which has all the degrees of freedom fixed, is modeled with rigid elements (R3D4) with a maximum element size of 2.5 mm.

The LVI clamping system is based on ASTM D7136 [16]. The specimen is restrained during the impact by means of four rubber-tipped clamps, which are placed outside of the rectangular cut-out (see Fig. 4.1). They are modeled with rigid elements (R3D4) as in [65] with a maximum element size of 1 mm. No model sensitivity was found due to the element type used for the rubbers. The rubbers are cylinder-shaped with a diameter of 14 mm and they have all the degrees of freedom fixed.

The geometry and boundary conditions of the CAI model were previously sketched in Fig. 4.2. Sets of nodes are defined to apply the boundary conditions of the CAI test, which mimic the experimental ones (e.g. knife edges, clamping).

5.2.2 Contact and friction

As described in Section 4.2.2, the general contact algorithm from Abaqus/Explicit [1] is used. The contact pairs known beforehand (i.e. ply by ply) are defined and the cohesive elements are excluded from the contact algorithm. The contact stiffness value (K_n) is defined equal to the penalty stiffness of the cohesive elements (K_{coh}) in order to control the STI and a sensitivity analysis is carried out to select the optimum penalty stiffness value.

Friction is introduced between all the contacting surfaces through the Abaqus/Explicit [1] built-in Coulomb friction model. The friction coefficient depends on the materials in contact and on the surface quality [93, 140] but also on the interface angle [140]. A friction coefficient of 0.1 for all contacts was chosen based on the sensitivity analysis from Section 5.4.5.

5.3 Plate modeling

Fiber breakage and, especially, delamination might spread over the specimen width during the CAI test. A mesh refined region at the impact area was used to reduce the computational effort. The size of the refined region was 42 x 60 mm^2, which was sufficient to allow delamination growth during the LVI and CAI tests.

Significant fiber breakage was observed experimentally. Thus, the continuum finite elements of the numerical models are regular and oriented according to the fiber orientation at the refined region to accurately compute the characteristic element length used for mesh regularization of the smeared damage model while avoiding mesh orientation bias effect during crack propagation [63, 97].

5.3.1 Modeling strategy

In Chapter 4 was shown that conventional shell elements were less accurate in the prediction of the energy dissipated during the LVI. It was attributed to the fact in thick ply laminates matrix cracking is dominant which requires accurate transverse stress fields that plane stress based elements cannot fully capture because they neglect out-of-plane stresses. However, matrix cracking is delayed or even suppressed in thin ply laminates. On the other hand, the least computational demanding finite element were conventional shells. Furthermore, within an explicit FEA framework, conventional shell elements do not penalize the element STI ($\triangle t_{elem}$) due their element thickness which can be very small in thin ply laminates.

The Abaqus/Explicit [1] built-in conventional shell elements with reduced integration (S4R) and zero-thickness cohesive elements (COH3D8) are used in the present work. In Chapter 4 was shown that the use of conventional shell elements with zero-thickness cohesive elements correspond to a good balance between accuracy and computational efficiency. The zero-thickness cohesive elements are placed at the interface location while the conventional shell elements with middle surface reference are placed at the mid-ply location. Cohesive elements are tied with shell elements to ensure correct kinematic description for delamination as sketched in Fig. 5.1. The use of tie constraints allows non-conforming meshes to orient the finite elements along the fiber direction. Surface to surface discretization is used for the tie constraints in which the shell surfaces are always the master ones.

An element size of 0.5 and 5 mm are used for the refined and the coarse region, respectively. The element size criterion to ensure correct energy dissipation in the refined region is described in Section 4.3.4. In this case shell contact thickness reduction does not occur because of the in-plane element size (i.e. 0.5 mm) to thickness (i.e. 0.08 mm) ratio used. Therefore, SFM are

not needed to ensure normal contact.

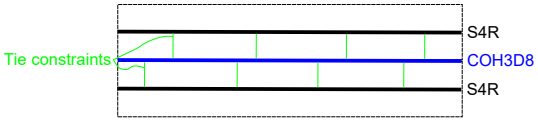

Fig. 5.1: Sketch of the modeling strategy with conventional shell elements (S4R) with zero-thickness cohesive elements (COH3D8) through tie constraints for correct kinematic description of delamination.

5.3.2 Intralaminar damage modeling

TeXtreme® is modeled as a homogeneous fabric-reinforced ply with the potential to sustain progressive stiffness degradation due to fiber breakage and in-plane plastic deformation under shear loading.

The continuum damage model proposed by Martin-Santos et al. [106] is used to model the mechanical behaviour of the plies. It was implemented through a user-written (i.e. VUMAT) subroutine for Abaqus/Explicit [1].

The model considers plane-stress conditions and four damage mechanisms. The surfaces for damage activation are generally defined as $F_N = \phi_N - r_N \leqslant 0$. Each damage activation function (F_N) accounts for one damage mechanism: longitudinal ($N = 1T$) and transverse ($N = 2T$) tension, longitudinal ($N = 1C$) and transverse compression ($N = 2C$). The loading functions (ϕ_N) depend on the effective stresses and material properties. The internal variables (r_N) set the maximum value that the loading functions can achieve before damage propagation, which are equal to unity while the material is undamaged. The internal variables are updated to the new damage threshold when the loading functions are larger than one.

The damage variables (d_N) are adjusted to smear a bi-linear traction separation law (see Fig. 4.6) for each damage mechanism in the continuum element following the crack band model [26]. For tension damage (Fig. 4.6a), a bi-linear law with a large drop of stresses due to fiber breakage is followed by a large tail that is related to fiber pull-out. For compression damage (Fig. 4.6b), a first drop of stresses defines the kink-band onset that is followed by a constant residual stresses related to kink-band broadening [122]. Details on the implementation of the model can be found in Ref. [106].

A maximum stress criterion is adopted for damage initiation criterion based on the mechanical characterization of TeXtreme® 160 g/m^2 and 240 g/m^2 performed by Arteiro et al. [13]. It was found that a maximum stress failure criterion was suitable to approximate the failure envelopes.

The carbon fiber type used in this study was Tenax® HTS45 with 12K filament yarn. The matrix was HexFlow® RTM 6 mono-component epoxy system, supplied by Hexcel®. The plies were 80 g/m^2 plain weave with 20

mm wide yarn fabrics produced by Oxeon and trademarked as TeXtreme® with a ply weave thickness of 0.08 mm. The sudied stacking sequence is $[(45/-45)/(0/90)]_{14S}$ with a nominal thickness of 4.48 mm. The measured fiber volume fraction according to EN2564 [160] was 56.1 %. The plies were manufactured with spread-tow technology [90] in which conventional filament tows are thinned by increasing the tow width. The laminates were manufactured through Resin Transfer Molding (RTM) process. The repeatability for each impact configuration was quite good despite the difficulties found on the RTM manufacturing process. The high fiber volume fraction of the plies, together with the specimen thickness with a large amount of plies at different orientations, lead to difficulties in the selection of the injection pressure of the resin which should be admissibly low to avoid fiber wash-out, but high enough to fill the mould before the resin starts curing. After some trials, a good compromise was found but some fiber wash-out and manufacturing voids appeared in the specimens. This could explain some experimental scatter, which was larger for the 30 J impact than the 20 J.

The fabric - reinforced material was characterized through an extensive experimental campaign. The material properties and parameters to feed the intralaminar damage model are summarized in Table 5.1. Most of them were obtained from tests at the ply level. The values taken to feed the material models from Table 5.1 are the average values obtained from each test. Five specimens were used for every test. The standard deviation values were below 10% with the exception of the interlaminar mode II fracture toughness, the fiber fracture toughness and compression strength. The compression strength was found to be large (i.e. 728 MPa). The scatter on the compression strength data lead to calibrate the fiber compression strength with the pristine test. In fact, the employed compression strength value is closer to reported values by other authors [13]. The density was measured according to UNE-EN ISO 1183-1 [161]. The tensile elastic and strength properties were obtained through tensile tests according to ASTM D3039M [18] while the compression elastic and strength properties were obtained from compression tests according to EN 2850 [52].

The shear response of fabric-reinforced composites is dominated by the non-linear behavior of the matrix, which includes both plasticity and stiffness degradation due to matrix micro-cracking. Plasticity with non-linear isotropic hardening is accounted for in the model under in-plane shear loading. Also, a maximum shear stress (S_L) in which the material eventually fails. The shear strength (S_L) is the average failure stress of the in-plane shear tests performed on 6 samples according to ASTM D3518-13 [19]. The plastic model parameters S_{LP}, ζ_E, ζ_E^T and ζ_L were obtained through least squares fit from the averaged in-plane shear experimental response as shown in Fig. 5.2. The shear strength was a key parameter to define for successful LVI simulations.

Wagih et al. [164] observed little matrix cracking in TeXtreme® 80 g/m^2

Density	1.5 x 10^{-9} t/mm^3
Elastic properties	$E_1 = E_2$ = 61400 MPa ; G_{12} = 3782 MPa ; ν_{12} = 0.042
Strength	$X_{1T} = X_{2T}$ = 975.4 MPa ; $X_{1C} = X_{2C}$ = 550 MPa ; S_L = 85.9 MPa
Plastic model parameters	S_{LP} = 30 MPa ; ζ_E = 34.5 MPa ; ζ_E^T = 141.5 ; ζ_L = 335.1 MPa
Fracture toughness	$G_{1T} = G_{2T}$ = 65.4 N/mm ; $G_{1C} = G_{2C}$ = 34.9 N/mm
Traction separation law parameters	$f_{X_{1T}} = f_{X_{2T}}$ = 0.1 ; $f_{X_{1C}} = f_{X_{2C}}$ = 0.1 ; $H_{X_{1T}} = H_{X_{2T}}$ = 14435 N/mm^3 ; $H_{X_{1C}} = H_{X_{2C}}$ = 3903 N/mm^3

Table 5.1: TeXtreme® 80 g/m^2 material properties and parameters used for the continuum damage model.

during quasi-static indentation tests while delamination and fiber breakage were the governing damage mechanisms of the laminate. The small ply thickness together with the fabric structure of the laminate could explain the small amount of matrix cracking. For this reason, matrix cracking was assumed negligible in the model. Thus, fiber fracture was the only intralaminar damage mechanism accounted for in the longitudinal and transverse direction of the model. The fiber fracture toughness under compression before crushing and tensile were obtained through CC and CT tests [129], respectively.

Fig. 5.3 shows that an intralaminar traction separation law with linear softening is insufficient to reproduce the experimental CT test response, which is in agreement with the findings from Dávila et al. [50] and Ortega et al. [122]. The intralaminar model parameters (f_{X_N} and H_N) that define the fiber traction separation law shape for tensile and compression loading should be adjusted to the best fit of the CT and CC load displacement curve on cross-ply laminates through FEA, respectively. It is worth noting that a bilinear law with a plateau that represents the constant residual stresses related to kink-band broadening [122] is again considered. The compression fracture toughness before crushing is G_{X_C} = 34.9 N/mm, which is the measured fiber compression fracture toughness of the ply weave. The fiber traction separation laws were of paramount importance to successfully reproduce the LVI simulations.

The model does not consider strain rate effects. It is generally accepted that in LVI the velocity is low enough to assume a static response of the structure [145, 148, 171]. Furthermore, in the studied case indentation tests and LVI tests could be compared and the difference among them is attributed to the dynamic loading (Fig. 5.4).

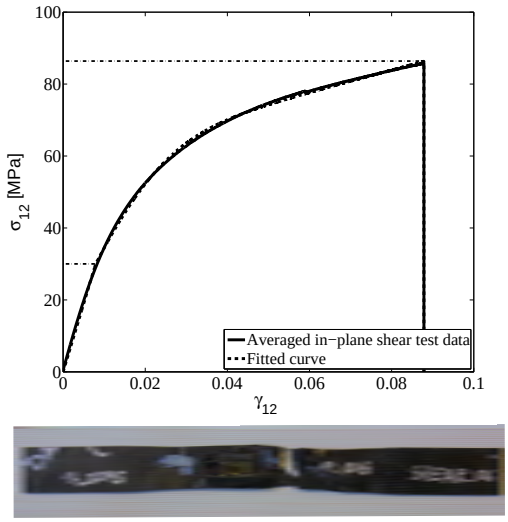

Fig. 5.2: Least squares fit of the plastic parameters for the in-plane shear behaviour of the constitutive model and a failed sample at the end of the test.

5.3.3 Interlaminar damage modeling

All the interfaces for delamination were considered for accurate predictions because the damage propagation can be altered by allowing delamination to occur only at a pre-defined number and location of interfaces as already reported in [116, 117]. Delamination was modeled by means of zero-thickness cohesive elements with the thermodynamically consistent CZM from González et al. [66]. It was implemented in a VUMAT user-written subroutine for Abaqus/ Explicit [1].

A scalar damage variable is used to ensure irreversibility of the damage process. The model has an unilateral behaviour for mode I crack propagation in order to account for crack closure and symmetric behaviour for shear propagation modes. The damage initiation and propagation criteria are based on the B-K criterion [27] while the damage evolution is controlled through the cohesive law shape, which is assumed linear.

The input parameters required to define the CZM are summarized in Table 5.2: τ_{Ic} and τ_{IIc}, interface strengths for pure mode I and for pure shear modes (II and III), respectively; G_{Ic} and G_{IIc}, interface fracture toughness for pure mode I and for pure shear modes (II and III) respectively; η, is the mixed-mode interaction parameter used in the B-K criterion [27], which is obtained through least squares fit from interlaminar mixed mode tests.

The interlaminar mode I and mode II fracture toughness were obtained through DCB [21] and C-ELS [83], respectively. MMB tests [22] for 25 %, 50

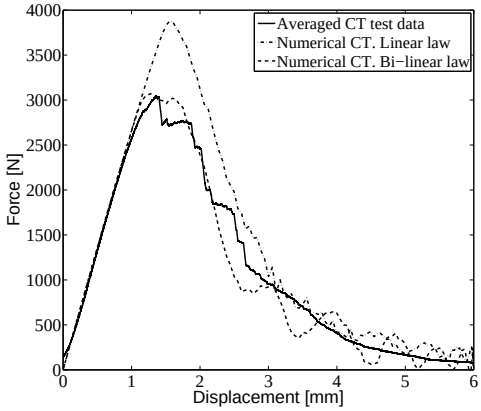

Fig. 5.3: Effect of the tensile constitutive law shape on the force - displacement response of a cross-ply CT test.

% and 75 % mixed mode ratios were performed to adjust the mixed-mode interaction parameter (η). The mode II interface strength was obtained from the in-plane shear test.

G_{Ic} [N/mm]	G_{IIc} [N/mm]	τ_{Ic} [MPa]	τ_{IIc} [MPa]	η
0.59	1.08	58.76	76.5	3.1

Table 5.2: TeXtreme® 80 g/m^2 interface material properties used for the CZM.

The mode I interface strength was not characterized. However, Turon et al. [156] demonstrated that changes in the local mode ratio during the evolution of damage under mixed-mode loading might cause errors in the energy dissipation, which can lead to inaccurate predictions of the global response. To solve this issue a relationship was proposed between interlaminar strengths and fracture toughness. The mode I interlaminar strength is obtained based on Eq. (5.1) [156], which is close to the experimentally obtained in [67] for the same resin.

$$\tau_{Ic} = \tau_{IIc}\sqrt{\frac{G_{Ic}}{G_{IIc}}} \tag{5.1}$$

In addition, the CZM requires two numerical parameters: the penalty stiffness and the surface density ($\bar{\rho}_{coh}$) of the zero-thickness cohesive elements.

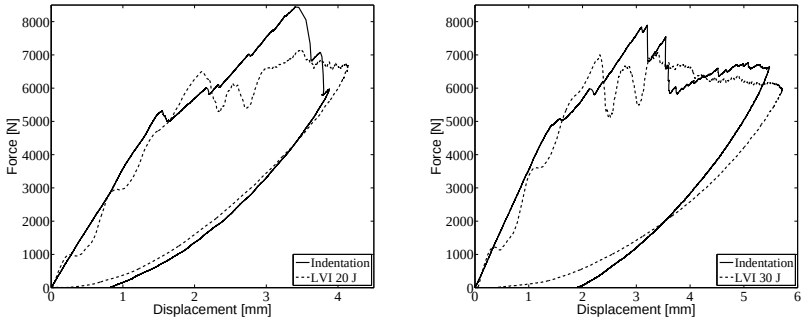

(a) **(b)**

Fig. 5.4: Comparison of indentation tests from Wagih et al. 2016 [164] and the LVI tests at a) 20 J and b) 30 J.

Penalty stiffness

The penalty stiffness should not be neither too large to avoid spurious oscillations [139] and detrimentally affect the STI (see Eq. (2.2)) nor too low to add compliance at the system.

A sensitivity analysis on the effect of the penalty stiffness value was done to obtain the optimum value in terms of accuracy and computational performance as Fig. 5.5 and Table 5.3 show.

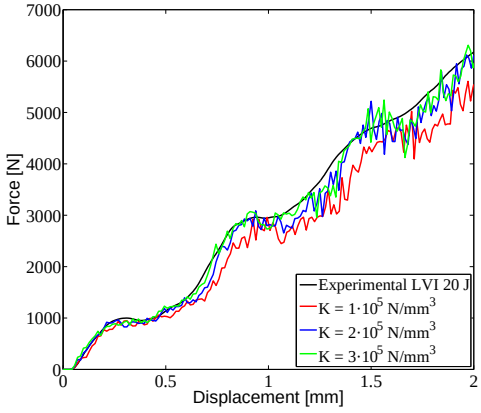

Fig. 5.5: Penalty stiffness effect (K) on the elastic force - displacement response of the 20 J LVI.

The same penalty stiffness value (K) was considered for the normal contact (K_n) and the cohesive elements (K_{coh}). The selected penalty stiffness value $K = 2$ x 10^5 N/mm^3 converged the numerical elastic regime to the experimen-

tal one.

K [N/mm^3]	Computed initial STI [s]	Computational time [h]	Step [ms]
1 x 10^5	2.46 x 10^{-8}	9.8	0.75
2 x 10^5	1.73 x 10^{-8}	14	0.75
3 x 10^5	1.42 x 10^{-8}	15.3	0.75

Table 5.3: Effect of the penalty stiffness value on the initial STI and computational time during the elastic regime of the 20 J LVI.

Zero-thickness cohesive elements surface density

The zero-thickness cohesive elements surface density is defined by distributing the mass of the laminate through the elements (i.e. continuum and cohesive elements) in order to maximize the STI of the model while keeping its mass. The factor (f_{coh}) which maximizes the STI with same penalty stiffness values ($K = K_{coh} = K_n$) is obtained from Eq. (4.16).

Table 5.4 shows the density values used for the simulations presented in Section 5.4.

ρ_{mod} [t/mm^3]	ρ_{coh}^{-} [t/mm^2]	n_{int}	h_{lam} [mm]	K [N/mm^3]
7.57 x 10 $^{-10}$	6.05 x 10 $^{-11}$	55	4.48	2 x 10^5

Table 5.4: Optimum density for the continuum elements (ρ_{mod}) and the zero-thickness cohesive elements ($\bar{\rho}$).

5.3.4 Element size

The maximum element size to avoid snap-back at the element level within the first branch of the intralaminar traction separation law is determined by Eq. (4.21) [106]. Accordingly, the maximum element size with the properties from Table 5.1 is 4.25 mm.

A conservative estimation of the interlaminar FPZ can be obtained by using the expressions from Chapter 3 and considering the smallest ply thickness modeled (i.e. 0.08 mm). The estimated interlaminar FPZ for pure fracture mode I and mode II are 0.21 mm and 0.8 mm in the studied material, respectively. Nevertheless, the actual interlaminar FPZ was measured in preliminary simulations in order to use a coarser element size. The actual interlaminar FPZ in the LVI simulation was about 2 mm and delamination was growing predominantly under mode II. The difference between the predicted and the actual interlaminar FPZ is due to the fact that only some interfaces

delaminated. The actual interlaminar FPZ of the CAI simulation was not possible to measure due to sudden damage growth (e.g. failure).

The chosen element size for both continuum and cohesive elements was 0.5 x 0.5 mm^2 at the mesh refined region for all the numerical models presented in Section 5.4. It ensured more than three elements along the interlaminar FPZ and no snap-back at the element level within the first branch of the intralaminar traction separation law. The element size at the coarse mesh region was 5 mm.

5.3.5 Element deletion criterion

In Chapter 4 was shown that special attention should be paid on the selected damage variable value. For the simulation of TeXtreme® both cohesive and continuum elements were initially deleted when the damage variable was equal to one or the shear strength was reached. Despite obtaining good agreement with the experimental tests, the simulations aborted due to contact issues (see Fig. 5.16). It is thought that the large number of plies modeled together with a significant number of elements deleted during the simulation (e.g. delamination and fiber breakage) led to the generation of many new contacts causing numerical difficulties.

Finally, the cohesive elements were deleted when the damage variable was equal to one while the continuum elements were not deleted to avoid the contact issues. The continuum elements were degraded up to a damage variable value (i.e. 0.99998371) that left a residual stiffness of 1 MPa. Also, the elastic properties were set equal to 1 MPa when the shear strength (S_L) was reached (see Fig. 5.2). The selected value allowed the simulations to be finished with correct dissipation of most fracture energy without adding stiffness into the model. Fig. 5.6 shows the effect of the selected maximum fiber damage variable value (d_1, d_2) or residual stiffness (E_r) without element deletion on the stress - strain response (Fig. 5.6a) and on the energy dissipated (Fig. 5.6b) for the studied material.

5.4 Results and discussion

The most relevant numerical results from the LVI and CAI simulations are presented in this section. They are presented together with the experimental data. Furthermore, sensitivity analyses are presented to study the effect of the mesh orientation, friction coefficient value, the effect of the fiber constitutive law shape and the number of interfaces for delamination.

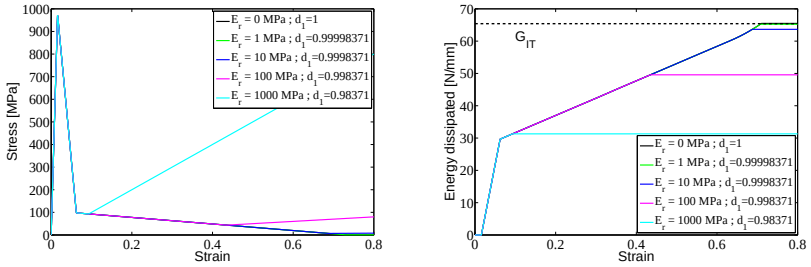

Fig. 5.6: Effect of the maximum fiber damage variable value (d_1) on (a) the stress-strain response and on (b) the energy dissipated. Tensile loading on a 1 x 1 mm^2 finite element with 1 mm thickness and the material properties from Table 5.1.

5.4.1 Low velocity impact results

Figs. 5.7 - 5.8 show the force - time and force - displacement response of the plate for a 20 J impact. The numerical results fall within the experimental scatter. The dynamic response and the damage initiation are perfectly captured. Also, the maximum force and displacement as well as the two load drops in the force - displacement curve (Fig. 5.8) are predicted.

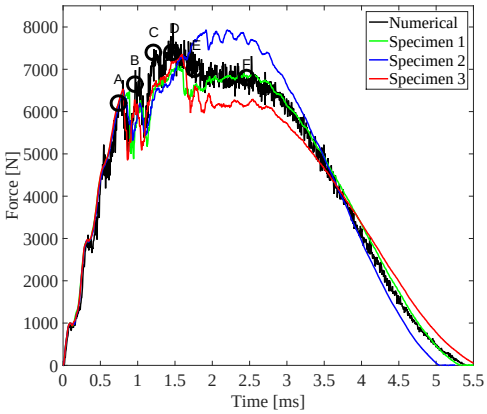

Fig. 5.7: Comparison of experimental and numerical force - time response for a 20 J impact. The circles are selected points to show the laminate damage state in Fig. 5.10.

Table 5.5 compares the numerical data with the experimental ones for the 20 J case.

Case	F_{max} [kN]	U_{max} [mm]	E_{dis} [J]	A_d [mm^2]	F_{CAI} [kN]
Numerical	8.17	4.13	10.64	926.38	122.78
Specimen 1	7.08	4.16	10.65	959.13	115.58
Specimen 2	7.93	4.10	9.39	851.36	119.26
Specimen 3	7.36	4.19	11.67	1194.39	115.41

Table 5.5: Comparison of experimental and numerical results for the 20 J case in terms of maximum force (F_{max}), maximum displacement (U_{max}), energy dissipated (E_{dis}), projected delamination area (A_d) and CAI strength (F_{CAI}) for the studied cases.

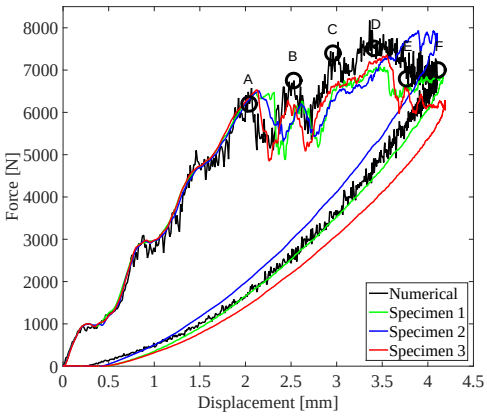

Fig. 5.8: Comparison of experimental and numerical force - displacement response for a 20 J impact. The circles are selected points to show the laminate damage state in Fig. 5.10.

Based on the dissipated energy evolution for the intralaminar and interlaminar failure mechanisms shown in Fig. 5.9, the first drop (after point A) observed in Fig. 5.8 is associated with delamination while the second one (after point B) is related to fiber damage and delamination.

Fig. 5.10 shows the interlaminar and intralaminar damage at every interface and ply of the laminate at some impact instants in which changes in the force - displacement (Fig. 5.8) and dissipated energy evolution are observed (Fig. 5.9).

There is no damage up to 4.5 kN. Then, some damage in the form of delamination and fiber breakage is initiated until 6.5 kN (point A). Fig. 5.10 shows that fiber damage is located at the top and the back-face plies due to compressive and tensile stresses, respectively. Point A and B are followed by two clear load drops in Fig. 5.8. The first load drop (A - B) is mainly due to delamination which is in agreement with Wagih's observations [164] even though fiber breakage is also present as Fig. 5.9 indicates. Fig. 5.10 shows

that in the first load drop delamination occurs at interfaces 5, 10, 16, 22, 26, 30, 31, 35, 41, 45, 47 and 49 while fiber breakage mainly occurs at the bottom half of the laminate. The damage initiation before point A seems to occur from the impacted side to the back - face while the propagation after point A occurs in the following sequence: 22, 16, 35, 41, 10, 26, 47,45, 49, 30, 31 and 5. Nevertheless, delaminations grow suddenly which makes it difficult to judge the sequence even with the numerical model. Fiber damage occurs above delamination in some plies (i.e. 11, 17, 23, 27, 36, 42 and 48). Thus, it seems that fiber damage could reduced in case of improving delamination resistance. In fact, delamination splits the laminate into sublaminates. More fiber damage is present at the bottom plies of these sublaminates due to larger bending stresses. The second load drop (B - C) is mainly due to damaged plies from the bottom half laminate as shown in Fig. 5.10 even though damage growth of existing delaminations also occurs. Finally, from point D to F, the existent delaminations grow a bit more but significant fiber breakage occurs throughout all the laminate thickness during this stage. It is worth noting that plies oriented at 45/-45 suffer more damage than those oriented in 0/90.

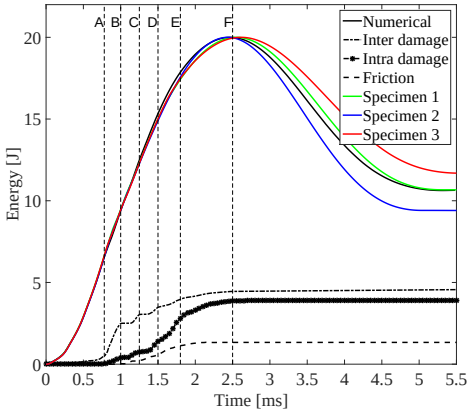

Fig. 5.9: Comparison of the experimental and numerical absorbed energy evolution of the plate for a 20 J impact.

Olsson et al. [116] mapped the fiber crack lengths through the thickness of the same laminate and material considered in the present study. An uniform damage width with an increase towards the back - face is reported. Olsson et al. [116] attributed this damage pattern to fiber failure due to membrane stresses and delamination preceding fiber fracture. The current model is able to reproduce the aforementioned experimentally observed damage pattern while confirming Olsson's arguments.

Wagih et al. [164] performed indentation tests to the same impacted ma-

terial with the same configuration. Under the equivalent displacement indentation (i.e. 4 mm) of the 20 J LVI, 7 delaminations were observed through C-scan inspections. Nevertheless, it was reported that smaller delamination could be hidden by larger ones. Wagih et al. [164] observed several delaminations to appear without shear matrix cracks what leaded to the interpretation that bending loads were the source of those delaminations.

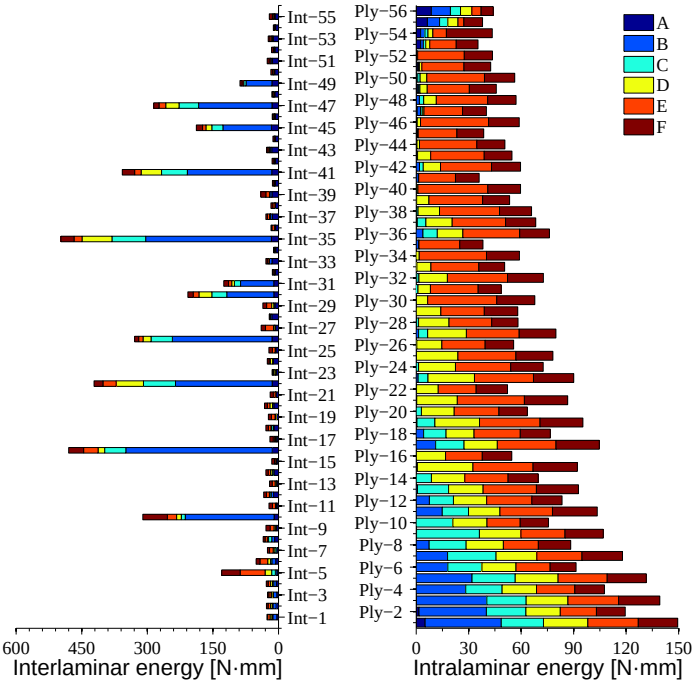

Fig. 5.10: Through the thickness (left) interlaminar (right) and intralaminar damage growth for the 20 J impact simulation at different impact times. Ply-56 is at the impacted side.

Fig. 5.11 shows the numerically obtained projected delamination area and the experimental ones. The numerical projected delamination area is fairly well captured. It under-predicts the average experimental projected delamination area ($\bar{A}_d$) but it falls within the experimental scatter. Despite being deleted and not considered in the calculations, they are still visible which allows to obtain the projected delamination area from d = 0.9 to d = 1 during the post-process.

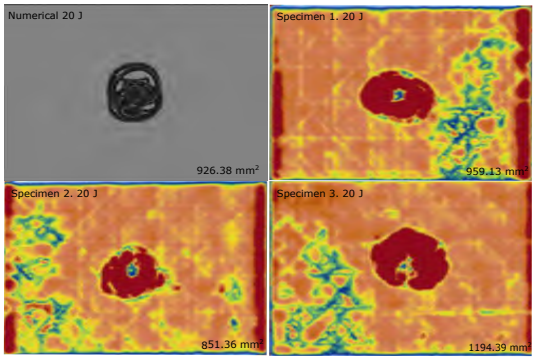

Fig. 5.11: Comparison of average experimental ($\bar{A}_d$ = 1001.72 mm^2) and numerical (A_d = 926.38 mm^2) projected delamination area for the 20 J impact. The projected delamination area from the numerical model takes the cohesive elements with d = 0.9 up to fully damage.

Fig. 5.12 shows a cross - section with the fiber damage variable field output at 2.5 ms of the 20 J LVI. Fiber breakage is present through the thickness but especially at the back - face of the specimen where elements are rather distortioned. Delaminations from Fig. 5.10 can be well identified.

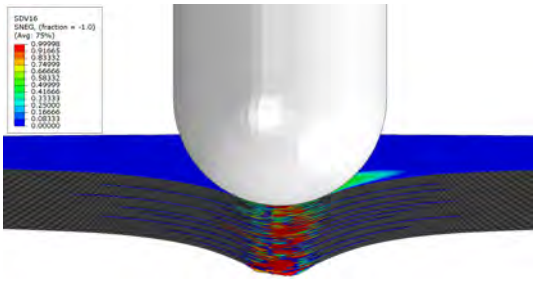

Fig. 5.12: Cross - section along the specimen length of the 20 J LVI at 2.5 ms. Fiber damage variable field output (SDV16).

The force - time and force - displacement response for the 30 J impact simulation are shown in Figs. 5.13 - 5.14, respectively. Fig. 5.15 depicts the absorbed energy evolution of the plate and the dissipated energy through friction, interlaminar and intralaminar damage. The force - displacement response and the absorbed energy evolution are in good agreement with the experimental results. The elastic regime and the two load drops in Fig. 5.14 are well captured. The first drop of the numerical model occurs around 6.5 kN as in the 20 J impact case, which is a slightly lower force than the experimentally obtained. However, it is accepted that this load threshold is independent of the impact energy [63]. The predicted maximum force and displacement fall within the experimental scatter.

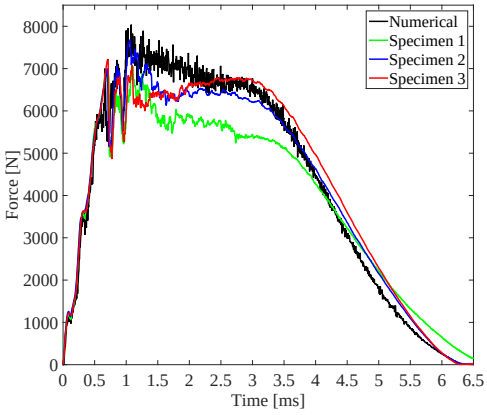

Fig. 5.13: Comparison of experimental and numerical force - time response for a 30 J impact.

Table 5.6 compares the numerical data with the experimental ones.

Case	F_{max} [kN]	U_{max} [mm]	E_{dis} [J]	A_d [mm^2]	F_{CAI} [kN]
Numerical	8.21	5.58	18.83	1396.40	93.79
Specimen 1	7.05	5.92	22.74	1879.83	96.2
Specimen 2	7.68	5.61	19.30	1938.65	80.29
Specimen 3	7.23	5.73	17.94	1083.65	89.76

Table 5.6: Comparison of experimental and numerical results for the 30 J case in terms of maximum force (F_{max}), maximum displacement (U_{max}), energy dissipated (E_{dis}), projected delamination area (A_d) and CAI strength (F_{CAI}) for the studied cases.

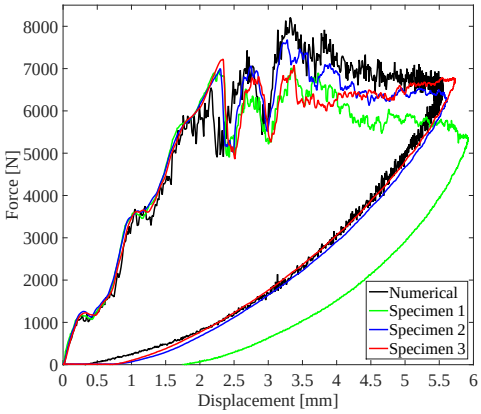

Fig. 5.14: Comparison of experimental and numerical force - displacement response for a 30 J impact.

The damage mechanism which dissipated more energy in the 20 J impact was delamination (Fig. 5.9) while fiber breakage became the most important one in the 30 J case (Fig. 5.15).

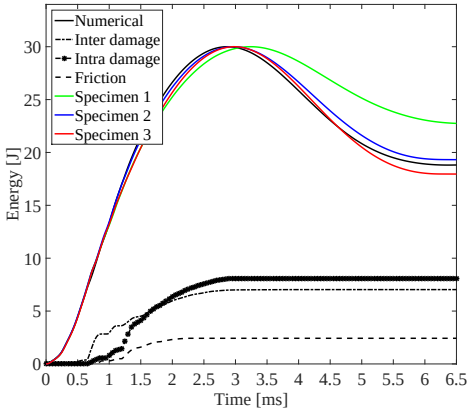

Fig. 5.15: Comparison of the experimental and numerical absorbed energy evolution of the plate for a 30 J impact.

The damage sequence in the 30 J LVI is similar to the 20 J impact case. There is an almost elastic regime up to the first load drop from Fig. 5.14 in which damage propagates mainly due to delamination (i.e. 6.5 kN) and fiber damage occurs at the top and bottom plies because of compressive and tensile loads, respectively. The predicted delamination are due to interlaminar shear stresses which splits the laminate within sublaminates, which suffer larger

fiber damage at the bottom plies due to larger bending stresses. The second load drop is due to a sudden growth of exiting delamination and especially fiber damage at the bottom plies of the laminate. Finally, there is a stage mainly governed by fiber breakage. The third load drop, which is associated with fiber breakage, is not so well captured as the two previous ones.

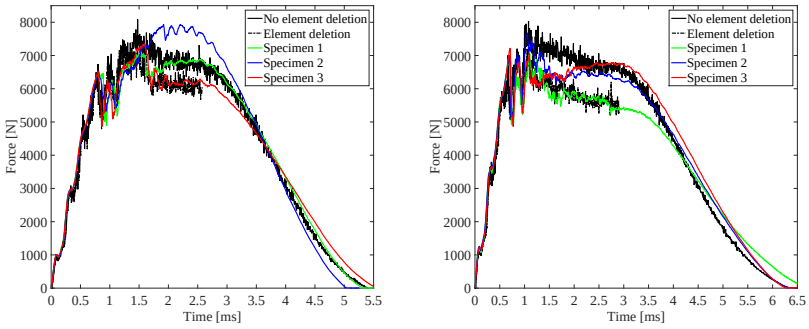

Fig. 5.16: Effect of continuum element deletion on the force - time response for the a) 20 J LVI and b) 30 J LVI.

Fig. 5.17 shows the numerically obtained projected delamination area and the experimental ones. The projected delamination area of the numerical model is smaller than the averaged experimental one ($\bar{A}_d$) but it falls within the experimental scatter as it happened for the 20 J impact. The models tend to under-estimate the projected delamination area which could stem in the fact that matrix cracking is neglected. The continuum elements were not deleted in order to finish the simulation and a remaining stiffness of 1 MPa was left. Despite the remaining stiffness being very low, it affects the interaction between intralaminar and interlaminar damage as shown in Fig. 5.16. This effect is more noticeable for the case of 30 J in Fig. 5.16b, which partially explains the under-estimation of the predicted projected delamination area in the 30 J case.

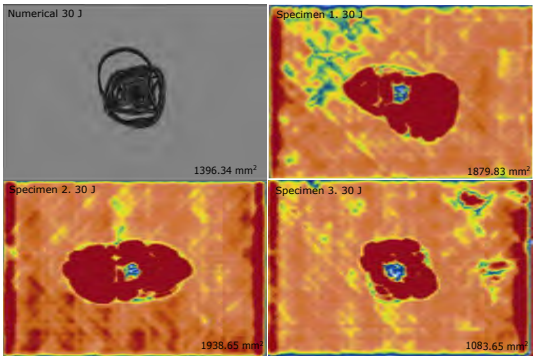

Fig. 5.17: Comparison of average experimental ($\bar{A}_d$ = 1634.04 mm^2) and numerical (A_d = 1396.34 mm^2) projected delamination area for the 30 J impact. The projected delamination area from the numerical model takes the cohesive elements with d = 0.9 up to fully damage.

The maximum fiber damage variable (i.e. 0.99998371) was reached in the 30 J LVI numerical model. Figs. 5.18 - 5.19 compares the experimental observations with the numerical results. Indentation and fiber breakage was observed at the impacted side and back - face of the specimens, respectively. The model predicts some fiber damage due to compression stresses at the impacted side and fully damaged fiber at the back-face.

(a) **(b)**

Fig. 5.18: Front - face view (30 J) at (a) specimen and (b) numerical model. Field output of fiber damage variable (SDV16) with applied translucency.

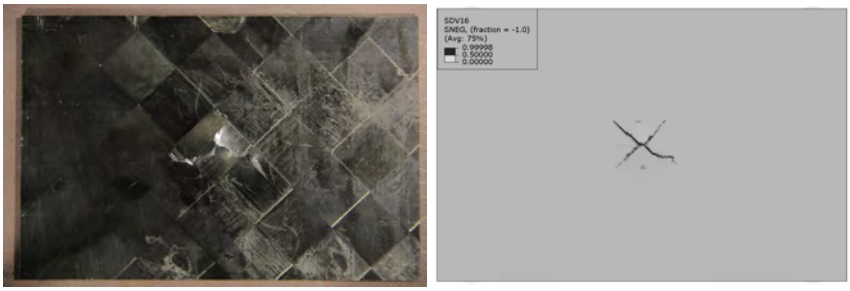

(a) **(b)**

Fig. 5.19: Back - face view (30 J) at (a) specimen and (b) numerical model. Field output of fiber damage variable (SDV16) with applied translucency.

Table 5.7 shows the computational time together with the maximum and minimum STI achieved during the simulation for each numerical model. The maximum STI is very close to the estimated one in Table 5.8 with the calculated optimum densities from Table 5.4. The minimum STI for the 30 J impact is much lower than for the 20 J because the larger impact energy the larger finite element distortion, which detrimentally affects the STI. The simulations were computed using 20 CPU's with the same computer described in Section 4.4.

Impact energy [J]	Step [ms]	Computational time [h]	Max. STI [s]	Min. STI [s]
20	5.5	121	1.71×10^{-8}	1.16×10^{-8}
30	6.6	144	1.71×10^{-8}	8.46×10^{-9}

Table 5.7: Computational time and STI achieved during the LVI simulations.

The large number of plies and interfaces modeled together with significant element distortion due to damage led to a large computational time. Table 5.8 shows the initial STI and the optimum densities which would require a simulation with volumetric finite elements and zero-thickness cohesive elements. The small ply thickness modeled (i.e. 0.08 mm) would have led to an initial STI 44 % smaller if volumetric finite elements (i.e. continuum shells or solid elements) had been used. Furthermore, volumetric elements suffer more element distortion than conventional shell elements as shown in Chapter 4.

Finite element type	Initial STI [s]	n_{inter}	h_{lam} [mm]	K [N/mm^3]	h_{elem} [mm]	L_e [mm]
Conventional shell	1.73×10^{-8}	55	4.48	2×10^5	0.08	0.5
Volumetric	9.66×10^{-9}	55	4.48	2×10^5	0.08	0.08

Table 5.8: Initial STI as a function of the finite element type chosen.

5.4.2 Compression after impact results

The force - displacement response of the CAI simulation for the 20 J and 30 J impact cases are shown in Figs. 5.20 and 5.23, respectively. The displacements during the CAI tests were only measured with the cross-head tester and the set-up was adding compliance into the system. The actual specimen compliance was obtained from the pristine test data and a numerical model as similarly done in [50]. The compliance obtained (4 x 10^{-6} mm/N) was subtracted to the displacements of all CAI experimental results (i.e. 20 J and 30 J).

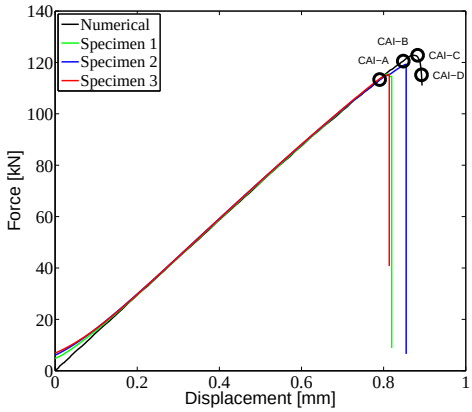

Fig. 5.20: Comparison of experimental and numerical CAI force - displacement response for the 20 J case. The circles are selected displacements to show the laminate damage state in Fig. 5.25.

Fig. 5.21 shows the front - face and back - face of the CAI simulation at 20 J. A crack crossing the whole specimen width can be seen at the front - face.

(a) **(b)**

Fig. 5.21: a) Front - face and b) back - face view of the CAI simulation at 20 J. Field output of fiber damage variable (SDV16) with applied translucency.

Fig. 5.22 shows a cross - section along the specimen length of the CAI 20 J. Existent delaminations created during the impact (see Figs. 5.10 and 5.12) further progressed during the CAI simulation. Only interface 9 and 21 propagated during CAI and not during the LVI.

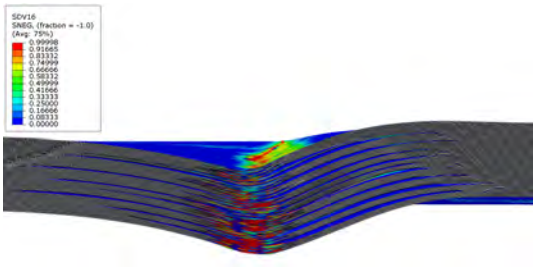

(a)

Fig. 5.22: Cross - section along the specimen length of the CAI 20 J just after failure. Fiber damage variable field output (SDV16).

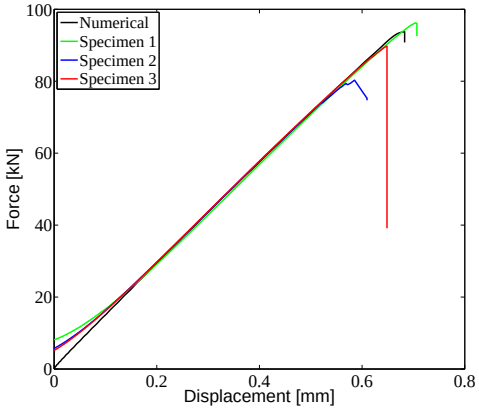

Fig. 5.23: Comparison of experimental and numerical CAI force - displacement response for the 30 J case.

The models predicted the CAI stiffness correctly for both studied cases. In fact, the damage due to impact hardly influenced the global in-plane stiffness of the panel as shown in Fig. 5.24.

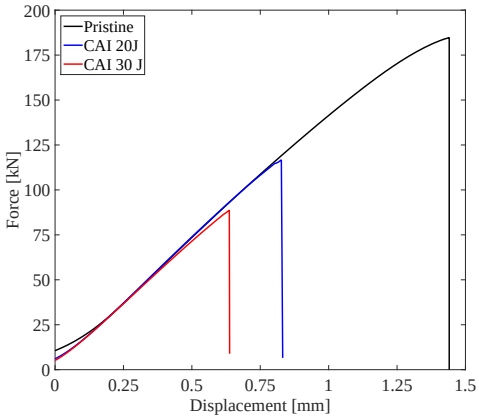

Fig. 5.24: Averaged force - displacement response comparison of pristine and CAI experimental tests.

The CAI strength were fairly well predicted. The averaged experimental CAI strength were over-predicted by 5.16 % and 5.68 % for the 20 J case and 30 J case, respectively. The model did not account for any kind of defect from the manufacturing process or residual deflections. The projected delamination area were under-predicted for both cases which could explain the slight over-prediction of the CAI strength.

Fig. 5.25 shows the energy dissipated at every ply and interface of the 20 J impacted laminate during the CAI simulation. Four different instants of the force - displacement curve from Fig. 5.20 are plotted in Fig. 5.25. The CAI tests of thin ply laminates show a more brittle behaviour than the results from thick plies (Chapter 4). Based on the numerical predictions, there is small damage growth during stage A for the amount of applied displacement. An increase of damage growth is predicted from point B up to reaching the CAI strength at point C, which only occurs at the larger existent delaminations from the LVI and the plies close to the impacted side. Finally, sudden damage growth occurs at point D due to specimen collapse. The predicted damage sequence for the 20 J CAI was similar for the 30 J CAI simulation.

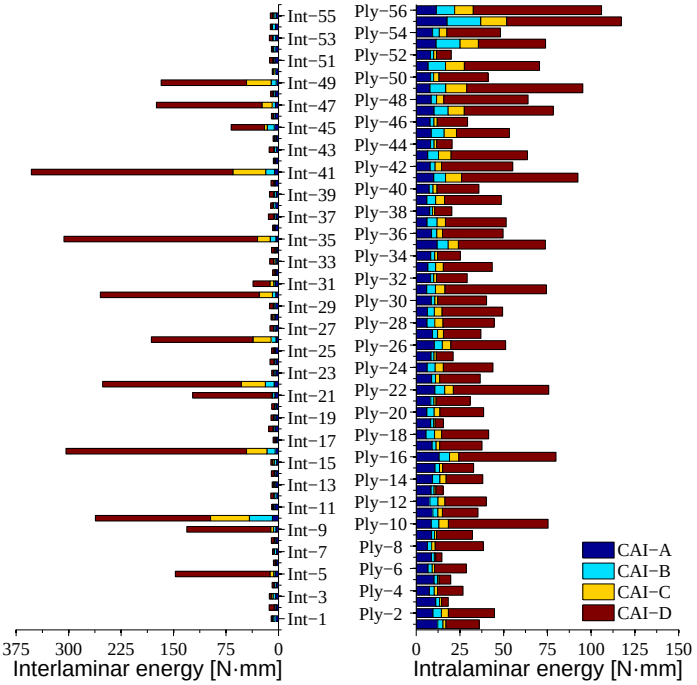

Fig. 5.25: Through the thickness (left) interlaminar and (right) intralaminar damage growth during the CAI (20 J) simulation at different displacements. Ply-56 is at the impacted side.

5.4.3 Mesh orientation effect

As mentioned, the continuum finite elements were regular and oriented according to the fiber orientation at the refined region to accurately compute the characteristic element length used in the crack band model [26] while avoiding mesh bias effects during crack propagation [63, 97].

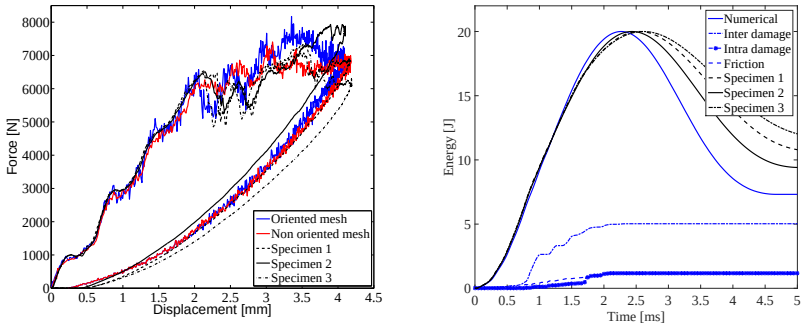

(a) **(b)**

Fig. 5.26: a) Effect of orienting the mesh along the fiber direction on on the force - displacement and b) energy absorbed prediction for the 20 J LVI.

The effect of whether orienting or not the mesh according to the fiber direction is shown in Fig. 5.26. Fig. 5.26 does not show big difference in terms of global force - displacement response and plate energy dissipated due to orienting the mesh along the fiber direction. However, less fiber breakage and more delamination is predicted by the non-oriented mesh, which is translated in a less accurate capture of the two load drops from Fig. 5.26a. The impact of orienting the finite elements along the fiber direction depends on the amount of damage and the element size. For impacts with BVID the effect of orienting the mesh will be lower than for cases with VID. Also, fine meshes will allow easier orientation of crack localization than in coarser meshes.

5.4.4 Effect of the number of interfaces for delamination

The effect of the number of interfaces considered in the model was studied for the 20 J case. It was considered a case with 6, 13 and 55 interfaces for delamination. The interfaces for delamination were equally spaced through the laminate thickness. The three models had the same mesh refinement for the sake of comparison.

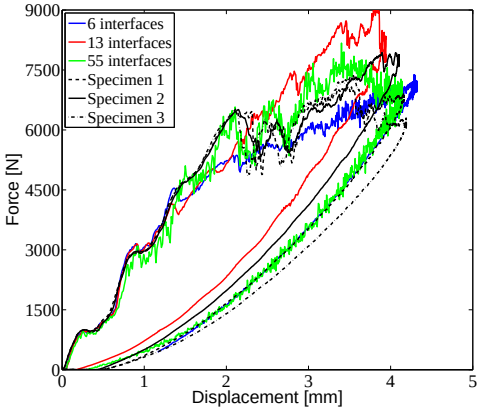

Fig. 5.27: Effect of the interface for delamination considered on the predicted force - displacement response for the 20 J LVI.

Fig. 5.27 shows that the structural response is rather affected by the number and location of the interfaces for delamination. The damage initiates similarly at 4.5 kN but the propagation is rather different in every case. Consequently, the projected delamination area is affected as shown in Fig. 5.28.

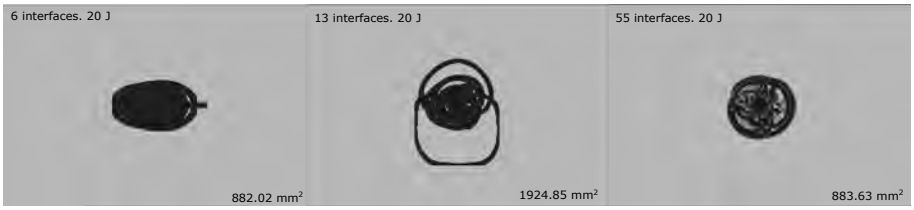

Fig. 5.28: Effect of the number of interfaces considered for delamination on the projected delamination area for the 20 J impact. Contour plot of the cohesive elements with d = 0.9 up to fully damage.

Fig. 5.29 shows the evolution of the interlaminar and intralaminar dissipated energy of the models. It highlights the need of considering all the interfaces for accurate impact predictions because the damage evolution is modified due to the number and location of the interfaces.

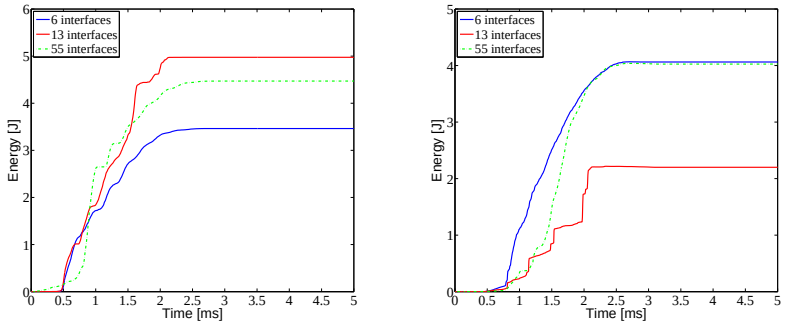

Fig. 5.29: Effect of the interface for delaminaton considered on the predicted (a) interlaminar and (b) intralaminar dissipated energy evolution for the 20 J LVI.

The CAI strength showed to be also dependent on the number and location of the interfaces for delamination as shown in Fig. 5.30. The case with 13 interfaces has the lowest CAI strength which could be related to the fact that larger delamination was predicted while the case with 6 interfaces has the largest CAI strength due to a lower amount of fiber damage.

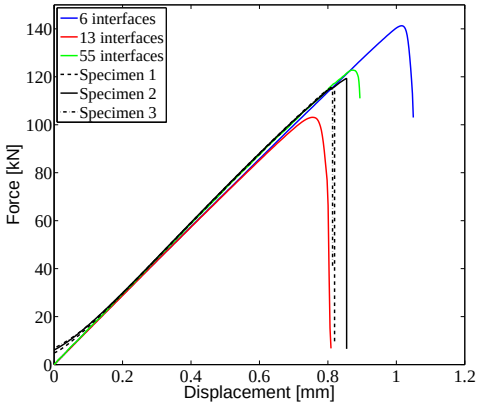

Fig. 5.30: Effect of the interface for delamination considered on the predicted force - displacement on the CAI response of the 20 J impact case.

5.4.5 Effect of the friction coefficient

A sensitivity analysis was carried out on the friction coefficient of TeXtreme® 80 g/m^2 due to the lack of information of this material property.

Through the thickness compressive stresses increases the mode II interlaminar strength and fracture toughness as Catalanotti et al. [38] investigated. The friction coefficient can play a role for LVI simulations. Fig. 5.31 shows the effect of the friction coefficient on the LVI response for a 20 J impact energy. The larger the friction coefficient, the larger the damage initiation force and the lower the maximum displacement. However, the results were not very sensitive unless friction-less contact was considered. Thus, the friction coefficient adopted was 0.1 which yielded good results either in the damage initiation and the damage propagation.

It is a low value in comparison with reported experimental values [93,140] and previous LVI numerical studies [61, 65, 98, 99, 154]. Schön et al. [140] discussed that the effective friction coefficient depends on the amount of load being carried in matrix/matrix, fiber/matrix and fiber/fiber contacts. Fiber/fiber contacts have a lower coefficient of friction. TeXtreme® 80 g/m^2 is a thin ply weave where more fiber/fiber contacts are likely to occur than in conventional UD pre-preg [61, 65, 98, 99, 154]. This could explain a lower coefficient of friction. Furthermore, in the recent experimental and numerical investigation from Catalanotti et al. [38] a friction coefficient of 0.1 was also adopted for the IM7/8552.

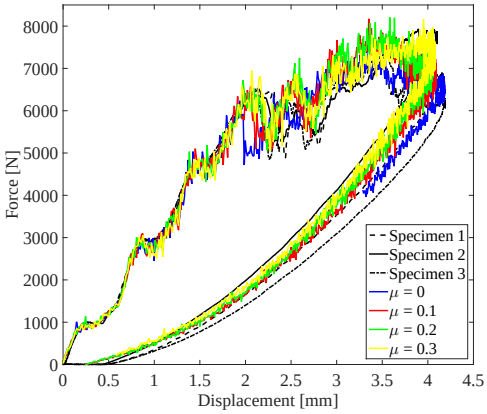

Fig. 5.31: Effect of the coefficient of friction value (μ) on the force - displacement response for a 20 J impact.

5.4.6 Effect of the fiber tensile traction separation law

The numerical predictions shown in Sections 5.4.1 - 5.4.2 were in good agreement with the experimental data. The previous results for the 20 J impact case are compared with those obtained using a linear tensile traction separation law. Fig. 5.32a compares the force - displacement response of the experimental data with the numerical predictions obtained with the two constitutive law shapes. The damage initiation is similar in both cases because it is mainly controlled by delamination as was previously discussed. However, the response clearly differs when fiber breakage becomes important after the two load drops.

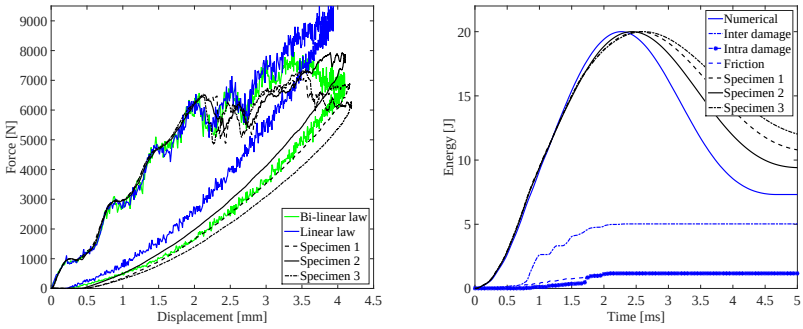

(a) **(b)**

Fig. 5.32: a) Effect of the fiber tensile traction separation law shape on the predicted force - displacement and b) on absorbed energy evolution for the 20 J impact.

In fact, the damage evolution is modified as Fig. 5.32b shows in comparison with Fig. 5.9. More energy is dissipated through delamination and much less through fiber damage. As a consequence, the dissipated energy is under-predicted.

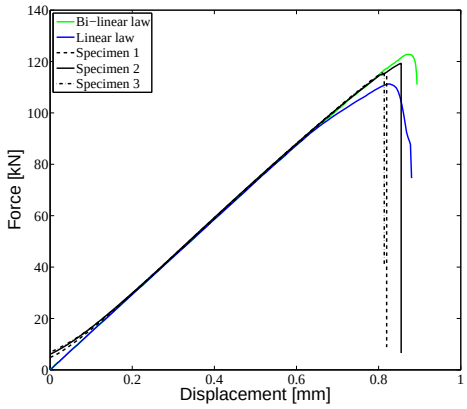

Fig. 5.33: Effect of the fiber tensile traction separation law shape on the CAI (20 J) force - displacement response.

The obtained projected delamination area is 1509.1 mm^2, which is much larger than the obtained experimentally (i.e. 1001.72 mm^2) and numerically (i.e. 926.38 mm^2) with the bi-linear law.

Fig. 5.33 shows that the CAI response is also affected. The model with the intralaminar linear softening shows a less brittle behaviour. The CAI strength is under-predicted and a loss of stiffness before reaching the CAI strength takes place due to propagation of delamination. Conversely, there was almost no loss of stiffness prior to failure in the experimental and numerical model with an intralaminar bi-linear law.

5.5 Conclusions

The methodology described in Chapter 3, which uses conventional shell elements together with zero-thickness cohesive elements, proved to be a feasible strategy for the simulation of LVI and CAI of the large number of plies and interfaces of the thin ply laminate TeXtreme ® 80 g/m^2. It has been demonstrated that all the interfaces for delamination must be modeled to accurately predict the coupling between intralaminar and interlaminar damage.

All the material properties to feed the constitutive models were obtained from experimental coupon tests at the ply level with the exception of the friction coefficient, which is difficult to characterize. A sensitivity analysis was performed to choose a suitable value. Some material properties such as interlaminar mode II fracture toughness and fiber fracture properties are of paramount importance to predict LVI and CAI tests. It is recommended to check the test data and to make sure that the deviations on the measured

data are not big enough to influence the model results. It is also a good exercise to reproduce the available tests at the laminate level before performing the LVI and CAI simulation (i.e. shear, pristine, CT and CC). The numerical study indicates that matrix cracking effects can be assumed negligible for the studied thin ply laminate. However, it has been highlighted the importance of the fiber traction separation law for accurate predictions. The fiber traction separation law shape was obtained from CT and CC tests on cross-ply laminates as proposed by some authors in the literature.

The predicted damage sequence during the LVI was similar for the two impact energies simulated. There was an initial elastic response until delamination started at about 4.5 kN. Delamination slightly progressed until 6.5 kN when a load drop, which was perfectly captured, occurred due to delamination propagation. A second load drop took place due to fiber breakage at the vicinity of delaminated interfaces. Afterwards, delamination and especially fiber breakage propagated in a steady state manner. The CAI showed a brittle behaviour. There was almost no damage propagation until final failure. Damage was initiated at the plies located close to the impact side as well as some progression of existent delamination occurred before final collapse. The predicted CAI strength was over-predicted by less than 6 % for both studied impact energies.

The presented model was efficient and accurate in the predictions but it lacked of robustness when the finite elements were deleted. It was not possible to finish the simulations despite obtaining good predictions. This is attributed to the large number of plies and interfaces modeled which led to contact numerical issues. The problem was circumvented by not deleting the elements but leaving them with a very small stiffness (i.e. 1 MPa). However, it would be desirable to delete them in some scenarios such as impactor perforation.

Chapter 6

LVI and CAI of composite stiffened panels

6.1 Introduction

LVI events are a major concern in the design of aerospace structures made of composite laminates because they might cause BVID while the residual strength of a structural component and its buckling load limit can be significantly reduced.

Physical testing of components requires extensive experimental campaigns that are time-consuming and costly. Numerical approaches are available in the literature to address coupon-level LVI and CAI that are computationally expensive and not practical for larger structures. For this reason, only few studies are found in the literature dealing with LVI simulation of structural components [59,87,134,150]. To the author's knowledge, Psarras et al. [131] is the only reported work on LVI and the sequential CAI simulation of large composite structures.

The present thesis aims to define an efficient methodology that enables analyses at larger scales than the coupon level, hence allowing industrial scalability. In this chapter, it is investigated the predictive capabilities of the methodology described in Chapter 4 when applied to structural components. The most relevant experimental and numerical results from the LVI and the sequential CAI test of a composite laminate sub-component are presented.

6.2 Geometry and boundary conditions

The geometry of the composite panel is shown in Fig. 6.1. All the plies and interfaces for delamination were modeled in order to avoid affecting the

damage sequence due to pre-definied potential interfaces for delamination as shown in Section 5.4.4. Also, all the plies and interfaces were modeled in the stringers because they could especially play a role in the CAI simulation. The ply clustering at the mid-plane was modeled with one element through the thickness as done in other studies [65, 98, 154].

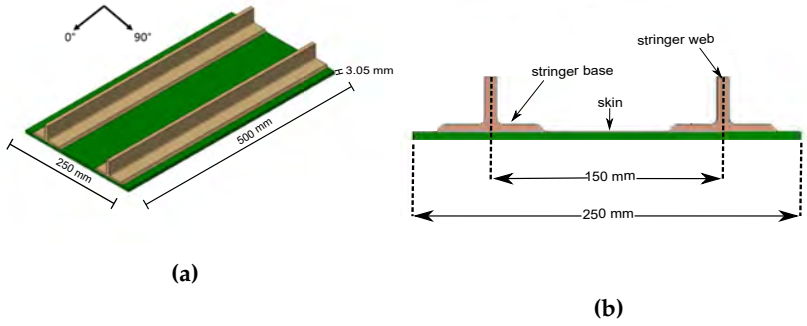

Fig. 6.1: (a) Dimension of the stiffened panel and (b) its section.

The clamping system used aluminium blocks bonded to the specimen ends by means of the Hysol® EA 9394 (epoxy paste) structural adhesive from Henkel®. The aluminium blocks were joined to the high stiffness steel frame of the impact tester using two bolts at each end. Each aluminium block covered the whole width and 40 mm length of the panel (i.e. potting). The specimen was impacted after the aluminium blocks were bonded and cured. No damage before testing was observed by visual inspection, neither at the interface between the aluminium blocks and the specimen nor inside the specimen.

Neither the structural adhesive nor the aluminium blocks were considered in the model for the sake of simplicity. The boundary conditions were applied through node sets at the panel instead of modeling the whole set-up and taking into account contacts. Fully clamped boundary conditions were considered at the edges of the panel while the rest of the pottings had all the degrees of freedom fixed with the exception of the longitudinal one in order to account for some compliance added by the adhesive in a simple manner.

The bonded aluminium blocks used for clamping the specimens during the LVI tests were also used for the CAI tests. Once the blocks were installed, the specimens were milled to achieve a tolerance of 0.1 mm in parallelism between faces. Additionally, anti-buckling side clamps were applied along the lateral edges to avoid global instability which could trigger compression failure as shown in Fig. 6.3.

Fig. 6.4 shows the CAI boundary conditions, which were introduced

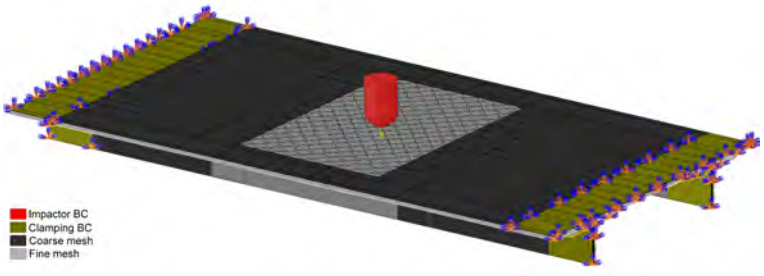

Fig. 6.2: Panel model assembly and boundary conditions for the LVI.

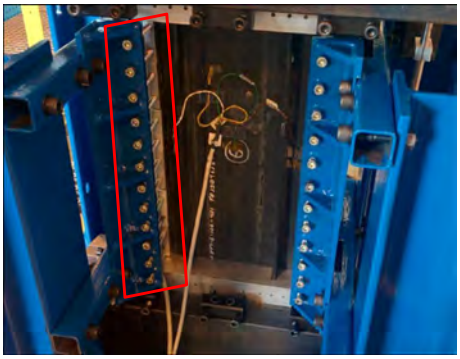

Fig. 6.3: View of the CAI set-up with the anti-buckling clamps highlighted in red.

through node sets that represent the anti-buckling side clamps.

Table 6.1 shows the impact test configuration. The panel was impacted at the center as shown in Fig. 6.2.

Impact side	Impactor mass [kg]	Impactor diameter [mm]	Impact energy [J]
Panel center	12.5	25.4	136

Table 6.1: Impact test configuration.

6.2.1 Contact and friction

As described in Section 4.2.2, the general contact algorithm from Abaqus/Explicit [1] is used and contact pairs known beforehand are defined (i.e. ply by ply) while cohesive elements are excluded from the contact algorithm. The contact stiffness value (K_n) is defined equal to the penalty stiffness of the cohesive elements (K_{coh}) in order to control the STI and a sensitivity analysis is carried out to select the optimum penalty stiffness value.

Friction is introduced between all the contacting surfaces through the

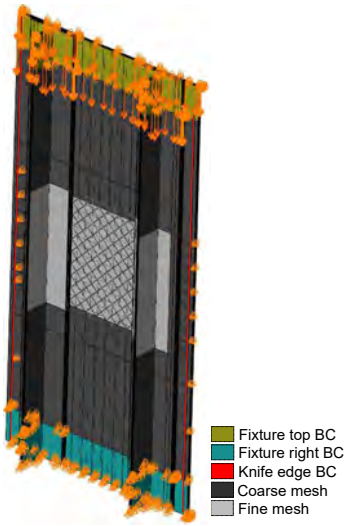

Fig. 6.4: Sketch of the CAI model and boundary conditions.

Abaqus/Explicit [1] built-in Coulomb friction model. A friction coefficient value of 0.3 was used. The model was not sensitive for friction coefficients larger than 0.1 prior impactor penetration.

6.3 Modeling strategy

Conventional shell elements with zero-thickness cohesive elements is the modeling strategy employed as in Chapter 5 because it proved to be the least computationally demanding in Chapter 4. In this case, surface elements are not needed to ensure contact because the in-plane finite element size (i.e. 1 mm) to thickness (i.e. 0.1905 mm) ratio was not scaling the shell contact thickness. Contact is guaranteed by conventional shell elements.

Fig. 6.2 shows the boundary conditions of the LVI model. Two element sizes were considered in the model: a finer mesh region (i.e. 1 mm) and a coarser mesh region (i.e. 5 mm). The refined mesh region had a size of 50 $\times$ 240 mm^2 to correctly capture the damage resulting from the LVI and CAI. The panel was meshed with regular finite elements. The results from Chapter 5, which involved significant amount of damage, were not very sensitive to the finite element orientation but the intralaminar and interlaminar interaction was better captured when the finite elements were oriented according to the fiber direction. The considered impact energy in this chapter also lead to a large amount of damage with impactor penetration. Thus, the finite elements were aligned along the fiber direction to avoid any mesh bias effect.

6.4 Intralaminar damage modeling

The composite material used is an intermediate modulus carbon/epoxy prepreg typically used in aerospace applications, with a nominal ply thickness of 0.1905 mm. The continuum damage model described in Section 4.3.2 is used to model the UD plies. Unfortunately, the experimental test campaign was limited at the sub-component level. A detailed material characterization as the one performed in Chapter 5 was not done. Thus, the material properties to feed the models were taken from previous experimental campaigns and similar material systems.

Table 6.2 shows the panel stacking sequence. The skin stacking sequence is according to the reference system from Fig. 6.1a while the web stacking sequence is sketched in Fig. 6.5a. The manufacturing process assured the stacking sequence symmetry in the web. It is worth noting that the filler plies were not modeled.

Part	Stacking sequence
Skin	$[45/90/-45/0/45/90/-45/0]$s
Web	$[45/0/-45/90/45/90/-45/0/0/-45/90/45]$s
Base right	$[45/0/-45/90/45/90/-45/0/0/-45/90/45/90/-45/0/45]$
Base left	$[45/0/-45/90/-45/90/45/0/0/45/90/-45/90/45/0/-45]$

Table 6.2: Panel stacking sequence.

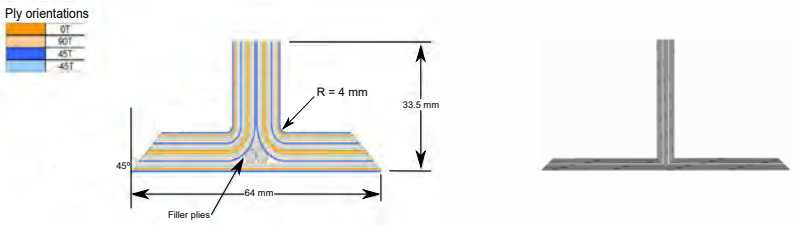

Fig. 6.5: a) Sketch of stringer lay-up and b) FE model cross-section.

The corresponding UD ply material properties used to feed the intralaminar damage model are listed in Table 6.3 in a dimensionless form for confidential reasons.

Fig. 6.6 shows a graphical respresentation of the *in situ* effect with the material properties from Table 6.3. The *in situ* properties were calculated according to [34, 103] and Eqs. (4.1) - (4.3).

Density	1.59×10^{-9} t/mm^3
Elastic properties	$E_1/E_2 = 15.78$; $E_2 = E_3$
	$G_{12}/E_2 = 0.478$; $\nu_{12}/\nu_{23} = 0.88$
Strength	$X_T/X_C = 1.6$
	$Y_T/Y_C = 0.2$
	$Y_T/S_L = 0.59$
Fracture toughness	$G_{X_T}/G_{X_C} = 1.33$
	$G_{Y_T}/G_{Y_C} = 0.1$
	$G_{Y_T}/G_{S_L} = 0.17$
Traction separation law parameters	$f_{X_T} = 0.4$; $f_{X_C} = 0.2$
	$H_{X_T}/H_{X_C} = 1.6$

Table 6.3: Dimensionless material properties and parameters used for the intralaminar damage model.

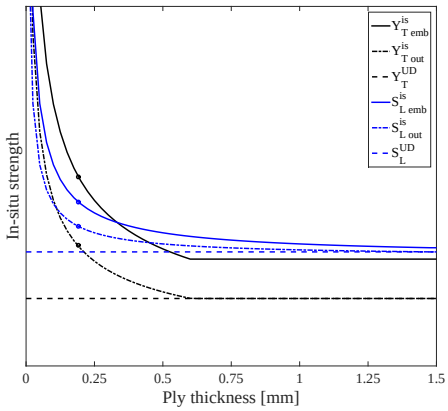

Fig. 6.6: Graphical representation of the tensile and shear *in situ* strength of the material. Circles are located at the studied ply thickness.

6.5 Interlaminar damage modeling

The CZM described in Section 4.3.3 is used to model delamination. The corresponding material properties used to feed the interlaminar damage model are also listed in Table 6.3 in a dimensionless form due to confidential reasons.

A penalty stiffness value of 5 x 10^4 N/mm^3 was enough to avoid adding compliance in the system as shown in Fig. 6.7.

G_{Ic}/G_{IIc}	τ_{Ic}/τ_{IIc}	η	K [N/mm^3]
0.17	0.59	1.9	5×10^4

Table 6.4: Dimensionless material properties and parameters used for the interlaminar damage model.

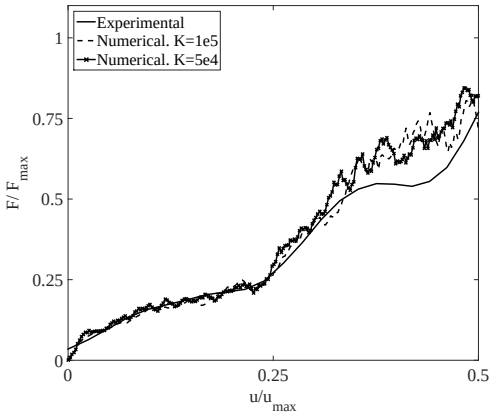

Fig. 6.7: Penalty stiffness effect (K) on the elastic force - displacement response of the panel.

6.6 Element size

Table 6.5 summarizes the maximum intralaminar element size for each damage mechanism according to Eq. (4.21). The interlaminar FPZ using the expressions from Chapter 3 and considering the smallest ply thickness modeled (i.e. 0.1905 mm) are 0.25 and 2.3 mm for pure mode I and mode II, respectively. However, the actual interlaminar FPZ was measured in preliminary simulations in order to use a less conservative element size, which was about 3 mm. An element size of 1 mm was selected and Eq. 2.5 was applied at Y_T to ensure correct energy dissipation.

6.7 Element deletion criterion

The element deletion criteria used here is the same described in Section 4.3.5. The elements are deleted when the fiber damage variable reaches a value equal to unity while matrix degradation is limited (i.e. d_2, d_6) to leave a minimum stiffness in order to avoid element distortion issues. The cohesive elements are also deleted when the damage variable is equal to unity too.

Damage mechanisms	Maximum element size [mm]
X_T	10.9
X_C	17.2
Y_T	0.3
Y_C	0.95
S_L	1.12

Table 6.5: Maximum intralaminar element size for each damage mechanism to avoid snap-back at element level.

6.8 Low velocity impact results

The machine used for the calculation of the composite panel LVI was the same as for the numerical benchmark from Chapter 4. The model had 11.45 million degrees of freedom and the computational time was of 69 hours using 20 CPU's. The impact time was 7 milliseconds.

The force - displacement response from the numerical model is compared with the experimental one in Fig. 6.8. The overall response is well predicted taking into account the complexity of the test and the large impact energy, which lead to a large amount of damage (VID). In fact, there was skin perforation.

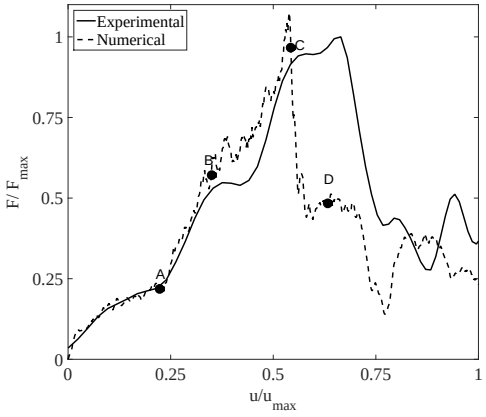

Fig. 6.8: Comparison of the numerical force - displacement impact response with the experimental one.

The elastic response (point A) and damage initiation (point B) are fairly well captured. The maximum force is reasonably well captured but the numerical model predicts the load drop at a much lower displacement (Point

C). It is worth noting that there was only one panel tested so it is not known the possible experimental scatter. Furthermore, the material properties were taken from similar materials systems because an experimental characterization at the ply level was not performed. The numerical model predicts a load drop that it is mainly due to fiber breakage rather than delamination. Afterwards, there is a stage of damage growth in which the model significantly under-predicts the force. The model has lower energy dissipation.

The residual stiffness for the matrix (E_r) should be the lowest possible but element distortion issues aborted the simulation for E_r < 50 MPa. Initially, E_r = 100 MPa was taken. However, an important effect on the force prediction was observed after the load drop as Fig. 6.9 highlights. Finally, a residual stiffness for the matrix of 50 MPa was used which allowed to finish the LVI simulation and to perform the sequential CAI simulation.

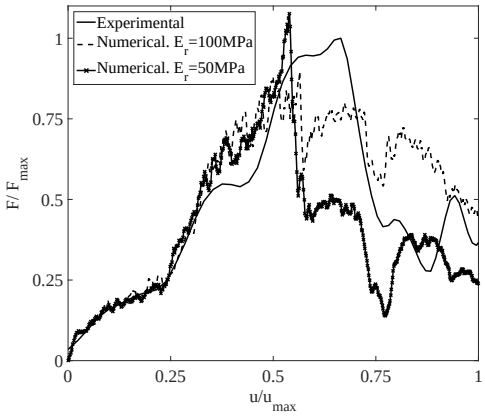

Fig. 6.9: Effect of the residual stiffness for the matrix (E_r) on the LVI simulation.

The complexity of LVI simulations with VID [87] is larger than with BVID [59, 131, 134] because they suffer much more damage, especially in the form of fiber breakage. It becomes very important to capture the interaction among damage mechanisms for accurate results. For instance, the fiber traction separation law shape is an important property to account for as discussed in Chapter 5. Unfortunately, the sub-component experimental test campaign was not accompained with a material characterization what makes difficult to indentify the discrepancies between the model and the experimental test. Furthermore, LVI simulations with VID are numerically challenging because they suffer severe element distortion that can abort the analysis. The model accuracy and robustness can be sensitive to the element deletion criterion. In Chapter 5 was reported a sensitivity of the results even for very low values of the residual stiffness when there was extensive damage. Some

authors [32, 150] use cohesive elements to model matrix cracking. This approach could circumvent numerical issues related to element distortion even though other aspects arise (e.g. mesh bias effects, discretization criterion and computational time).

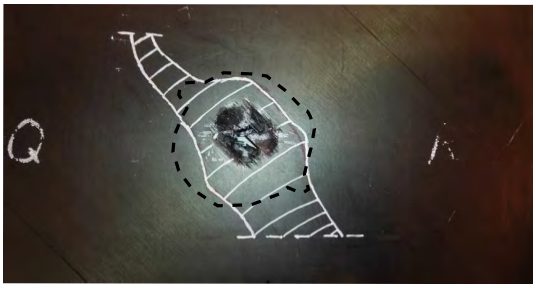

Fig. 6.10: Zoomed view from the impacted side after the LVI. The white dashed area is the experimental projected delamination area (A_d = 1575 mm^2) while the dark dashed line is the contour of the numerical projected delamination area (A_d = 1246 mm^2).

Fig. 6.10 shows the experimental projected delamination area of the panel (A_d = 1575 mm^2) together with the numerical one (A_d =1246 mm^2). The projected delamination area is under-predicted by 20.9 %. The model predicts that the largest delamination appears at the back - face. However, the model is not able to capture the extension of the delamination that appear diagonally at the back-face of the tested panel.

In Chapter 4 was already seen that it is difficult to capture the back-face delaminations. Only the *S4R CON* case was able to predict the largest delamination, which occurred at the back - face in the 45^o direction. Thus, the under-prediction of the stripes and delamination could be due to the modeling strategy that affects the interaction between interlaminar and intralaminar damage mechanisms. However, the fiber traction separation law, which was not characterized, can also affect the interaction between interlaminar and intralaminar damage but the discrepancies seem to be large to only attribute them to the modeling approach. The material properties should be tested, especially those material properties related to fracture propagation.

Fig. 6.11 shows the contour area of deleted elements due to fiber damage with the perforated skin region. The perforated area is smaller to the area with deleted elements due to fiber damage.

Fig. 6.12 shows a view of the LVI simulation with the fiber damage field output where it can be seen impactor penetration through the skin of the composite panel.

Fig. 6.11: Zoomed view from the impacted side. The dark line represents the contour area of deleted elements due to fiber breakage (d_1 =1).

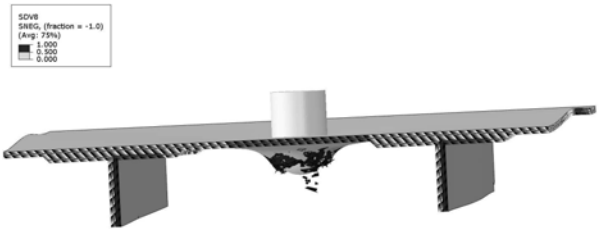

Fig. 6.12: View of impactor penetration through composite skin at instant u/u_{max} = 0.8. Field output of the fiber damage variable (SDV8).

6.9 Compression after impact results

In this section, the CAI test is shown together with a pristine test that was performed to a panel with the same configuration. Fig. 6.13 compares the numerical results with the experimental ones from both pristine and CAI tests. The displacements in the CAI test were measured through LVDT. Thus, no compliance calibration is needed as in Chapters 4 and 5 in which the displacements were measured from the machine.

The pristine panel failed at the middle down section as shown in Fig. 6.14. The pristine model had the same model definitions described for the CAI model but the mesh refined region was located at middle down section to capture the experimentally observed failure location.

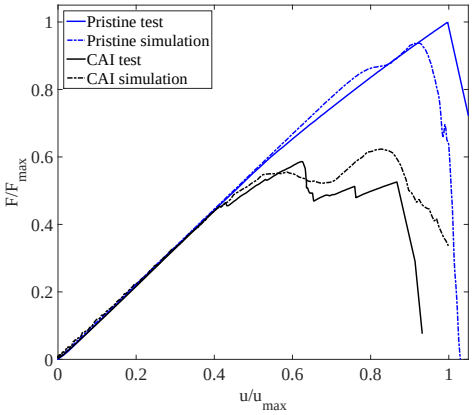

Fig. 6.13: Comparison among experimental and numerical results of the force - displacement response of the pristine and CAI tests.

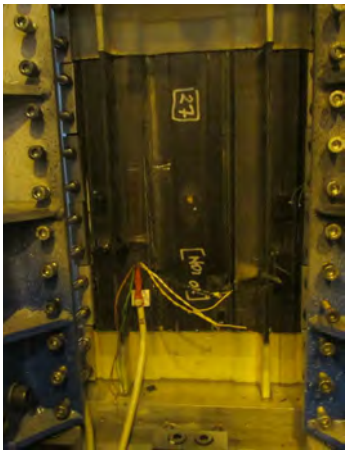

Fig. 6.14: Front view of failed pristine specimen.

The pristine simulation captures the stiffness up to $F/F_{max} = 0.6$. Afterwards, the pristine test shows a loss of stiffness, which could be attributed to damage propagation from some defects, that the model does not capture. However, the pristine model only under-predicts the strength by 6.2 %. On the other hand, the CAI test failed successfully at the impacted region. Fig. 6.15 shows the experimental and numerical failed CAI specimens, respectively. Fiber failure can be observed across the stringers width of the numerical model as well as in the tested panel. A fracture that crosses the whole width is not seen in the numerical model. Nervertheless, it is worth mentioning that the CAI model eventually aborts.

Fig. 6.15: a) Back - face image of the experimentally tested CAI panel and b) the numerical model.

The CAI numerical model is able to predict the stiffness even the damage progression prior to failure with fairly good agremeent. The numerical model under-predicts the CAI strengt by 5.36 % in the first load drop (i.e. u/u_{max}=0.6). Both pristine and CAI strength under-predictions are of similar magnitude what it could be attributed to some discrepancy on the used fiber compression properties. Despite having important differences in the predicted projected delamination area during the impact, the CAI strength is fairly well predicted. The final failure was governed by compression fiber breakage at the stringers which could explain that the results were less dependent on the damage produced by the impact.

6.10 Conclusions

In this chapter the methodology described in Chapter 4 was applied for the prediction of the LVI and the sequential CAI of a composite stiffened panel.

Conventional shell elements together with cohesive elements were used in order to make feasibly the simulation of the LVI and CAI of the subcomponent. It represented a challenging case not only by the structure size and complexity but also for the impact energy considered, which involved impactor penetration and severe damage (VID). The fracture material properties should be characterized to identify the sources of discrepancies between the numerical and experimental data. The relative error in the compression strength prediction of the undamaged and damaged panel were -6.2 % and -5.36 % (i.e. first load drop), respectively. From the modeling point of view, the element deletion criterion proved to be a limitation in terms of model robustness when there is extensive damage. Nonetheless, it was shown the potential of the employed techniques and modeling methodology to address problems of industrial interest such as the compression strength prediction of both undamaged and damaged stiffened panels.

Further work is required to improve the FEA robustness of LVI and CAI simulations when there is VID. It is thought that discrete approaches (e.g.

smoothed particle hydrodynamics) could circumvent the reported limitations related to element distortion. Improvements on the model efficiency are feasible. For instance, it could be done by embedding the finer region within a single shell element region tied through pure shell to shell coupling or the use of sub-cycling tecniques.

Part IV

Concluding remarks

Chapter 7

Conclusions

An efficient methodology that allowed to study the damage initiation and the damage propagation during LVI and the sequential CAI of challenging cases with scientific and industrial interest was proposed. The methodology was applied under different scenarios and it was always compared with experimental data. Numerical models require definition of several parameters that affect their efficiency, accuracy, robustness and objectivity. The key parameters have been described concisely and the selected values have been well justified and their sensitivity discussed.

At the coupon level, modeling strategies with different finite element types (i.e. conventional shells, continuum shells, solid elements) and cohesive interaction technologies (i.e. cohesive elements and cohesive surfaces) were systematically assessed in a numerical benchamrk. From the pre-processing point of view, strategies involving conventional shell elements are more tedious due to tie constraint definitions that ensure correct contact and kinematic description at the interfaces. Similarly, cohesive elements definitions are more tedious than cohesive surfaces for pre-processing. Conventional shell elements proved to suffer less element distortion than volumetric finite elements (i.e. solid and continuum shell elements). Cohesive surfaces do not suffer element distortion as it can happen with cohesive elements because they are not a topological entity. Element distortions are not desired because they detrimentally affect the simulation time through the model stable time increment. Furthermore, element distortions have an impact on the model robustness because they can eventually abort the simulation. Conventional shell elements were the least computationally demanding finite elements (i.e. about three times faster than solid elements) because of their simpler constitutive behaviour while zero-thickness cohesive elements were about 1.5 times faster than cohesive surfaces. Cohesive surfaces need a contact tracking algorithm that penalizes their efficiency. A laminate with an unusually thick

plies was selected to highlight possible limitations of plane stress based finite elements. The use of conventional shell elements together with cohesive elements proved to be the fastest approach with relative errors on the CAI strength below 4%. In fact, all the assessed modeling strategies that finished the simulations tend to under-predict the CAI strength with relative errors below 4%. However, conventional shell elements were less accurate than solid elements in the predicted energy dissipated during the LVI because of a poorer transverse shear description and they neglect of out-of-plane stress, which are important for damage predictions in thick ply laminates. Small differences between cohesive surfaces and zero-thickness cohesive elements in terms of accuracy were found. However, cohesive surfaces could be more appropiate to predict large delaminations than cohesive elements.

The adopted finite element size criterion that guarantees no snap-back within the first branch of the traction separation law as well as three elements along the interlaminar failure process zone proved to yield good results. Novel empirical formulas have been proposed to predict the interlaminar FPZ of a delamination growing at the mid-plane of an homogeneous orthotropic laminate under pure fracture mode I and mode II for linear softening cohesive laws. The formulae were used to estimate the interlaminar FPZ of the studied impact cases. A conservative estimation of the interlaminar FPZ is obtained by using the formulae from Chapter 3 and considering the smallest ply thickness modeled. However, some limitations are worth to remark. The number of delaminated interfaces due to a LVI is not known beforehand and the use of the proposed formula assuming that all the interfaces can delaminate lead to conservative element sizes as in Chapter 5 where 12 out of 55 interfaces actually delaminate. Also, the geometry and boundary conditions can be far from a crack growing at the mid-plane of a laminate under pure fracture mode as in Chapter 6. A recommendation on this regard, which was actually used here, is to choose the element size in order to have three elements along the interlaminar FPZ according to the formula for mode II. Then, to perform the simulation and measure of the actual interlaminar FPZ in the impact model to use an optimum mesh size that ensures correct energy dissipation (i.e. three elements along the interlaminar FPZ and avoid snap-back at the element level).

The penalty stiffness and surface density of cohesive interactions have an important impact in the simulation time through the model STI. They are both numerical parameters that have been defined for the sake of computational efficiency while not affecting the results. The optimum penalty stiffness was obtained by performing sensitivity analyses of the elastic regime to ensure no effect on the system compliance. The surface density of cohesive interactions was obtained by equaling the STI definition of continuum and cohesive interactions.

The sensitivity to the finite element orientation was low for the studied

cases. However, it is thought that this effect was of minor importance in the studied cases because the element sizes were fairly small. For larger element sizes the role of mesh orientation could be more important.

The element deletion criterion proved to control the model robustness but it can also affect the results when there is extensive damage. It is important to ensure the dissipation of the fracture toughness. Element distortion issues mainly come from matrix damage which easily lead to large element distortion during impact simulations. The employed modeling strategy was not sensitive in the BVID regime but no general criterion that perfectly works was found for VID.

The techniques and methodology proposed were applied to novel applications such as the prediction of the LVI and sequential CAI test of thin ply laminates at the coupon-level and to a sub-component composite stiffened panel. An extensive experimental campaign was conducted on the thin-ply weave laminate TeXtreme® 80 g/m^2 while it was not possible to characterize the fracture properties of the material used for the sub-component composite stiffened panel. Some material properties such as interlaminar mode II fracture toughness and fiber fracture properties are of paramount importance to accurately predict LVI and CAI tests. Therefore, it is strongly recommended to have reliable material test data. Otherwise, it is difficult to indentify possible limitations of the models. Also, it is recommended to check the test data and to make sure that the deviations on the measured data are not big enough to influence the model results. A good exercise is to reproduce the available tests at the laminate level before performing the LVI and CAI simulation (i.e. shear, pristine, CT and CC).

The use of conventional shell elements together with zero-thickness cohesive elements was a feasible strategy to model the large number of plies and interfaces for delamination of the thin-ply weave laminate TeXtreme® 80 g/m^2. An experimental campaign was carried out on TeXtreme® 80 g/m^2 from which all the material properties to feed the constitutive models were characterized with the exception of the friction coefficient. A sensitivity analysis was performed to choose a suitable value. The numerical study highlighted the importance of having reliable material data. Otherwise, it is difficult to judge and identify the limitations of the model. Also, it was highlighted the importance to account for the actual fiber traction separation law and all the interfaces for delamination to accurately predict the coupling between intralaminar and interlaminar damage. Conversely, matrix cracking coulb be neglected in the models. The numerical models over-predicted the CAI strength with relative errors below 6%. The fiber traction separation law shape was obtained from CT and CC tests on cross-ply laminates as proposed by some authors in the literature. All the remaining material properties were characterized at the ply level.

Finally, the same methodology was applied at the sub-compoenent level.

Unfortunately, the experimental test campaign was limited at the sub-component level and the material was not characterized at the ply level. This made difficult to judge whether the discrepancies of the impact model such as the smaller predicted projected delamination area were coming from the material properties used or some modeling limitation. It represented a challenging scenario not only by the structure size and complexity but also for the impact energy considered, which involved impactor penetration and severe damage. The element deletion criterion and the associated element distortion issues compromised the robustness of the model. However, the potential of the employed numerical tools and material models to address the strength prediction of both undamaged and damaged stiffened panels was shown. The relative error in the compression strength prediction of the undamaged and damaged panel were -6.2 % and -5.4 % (i.e. first load drop), respectively.

Chapter 8

Suggestions for future work

The methodology proposed with the employed tecniques in this thesis enables LVI and CAI analyses at larger scales with immediate applicability, hence allowing industrial scalability. However, there exist limitations yet to be solved.

The projected delamination pattern has not been generally captured with the selected modeling approach. Further research on simpler and more controlled cases should be done to understand the causes of it. This should allow to identify whether it is due to the modeling methodology or due to scatter on material properties that do not allow an accurate interaction between interlaminar and intralaminar damage. On the one hand, it should be assessed the effect of the employed cohesive interaction technology with further cases. Also, it should be assessed if modeling matrix cracking with discrete approaches, which actually models a discontinuity, lead to better delamination predictions. On the other hand, numerical models rely on material properties. Experimental testing always involves certain scatter and some tests more than others due to limitations on testing procedures and data reduction methods (i.e. interlaminar mode II fracture toughness, fiber compression fracture toughness, traction separation law shape determination). For instance, interlaminar mode II fracture properties certainly controls delamination during an impact. In the present work, all the interfaces were fed with the same material properties obtained from $0^o/0^o$ interlaminar tests. Also, it should be assessed the predictions sensitivity to certain material properties and, if necessary, to include this uncertainity in the models. Design of experiments methods could help to systematically treat and identify the most sensitive material properties in LVI and CAI tests. In this line, parametric optimization could also help in determining what material properties and how much should be improved to improve the damage resistance and damage tolerance of composite laminates.

The selected modeling approach proved to be robust for LVI with BVID. In fact, the use of conventional shell elements perform better than volumetric elements in terms of model robustness. However, model robustness issues were found due to element distortion in situations with extensive damage (VID). Different element deletion criteria were used without success. It is thought that the use of discrete approaches (e.g. smoothed particle hydrodynamics) should be explored becaue they could circumvent the reported limitations.

Further improvements on the models efficiency at the sub-component level can be done by means of sub-cycling and by embedding the finer region within a single shell element region tied through pure shell to shell coupling. However, it should be studied the dynamic effects derived from the use of this coupling.

If it is unfeasible the mesh size criteria described in 4.3.4 for engineering applications. Snap-back at the element level can be avoided by reducing the corresponding strength by means of Eq. 2.5 [26]. In fact, the subroutines used for the intralaminar damage models automatically reduces the strength if Eq. (4.21) is not fulfilled. Similarly, as proposed by Turon et al. [158] and done in Section 3.3.3, it can be done if the mesh size prescribed by Eqs. (3.7) - (3.8) is unfeasible. Despite ensuring correct energy dissipation, the damage initiation predictions are affected. Thus, this should be carefully studied.

References

[1] "Abaqus Analysis User's Manual," in *Abaqus documentation 6.12*. Providence, RI 02909 2499, USA: Simulia World Headquarters, 2012.

[2] H. Abdulhamid, C. Bouvet, L. Michel, J. Aboissiere, and C. Minot, "Numerical simulation of impact and compression after impact of asymmetrically tapered laminated CFRP," *International Journal of Impact Engineering*, vol. 95, no. Supplement C, pp. 154–164, 2016.

[3] M. R. Abir, T. E. Tay, M. Ridha, and H. P. Lee, "Modelling damage growth in composites subjected to impact and compression after impact," *Composite Structures*, vol. 168, no. Supplement C, pp. 13–25, 2017.

[4] S. Abrate, "Modeling of impacts on composite structures," *Composite Structures*, vol. 51, no. 2, pp. 129–138, 2001.

[5] G. Alfano, "On the influence of the shape of the interface law on the application of cohesive-zone models," *Composites Science and Technology*, vol. 66, no. 6, pp. 723–730, 2006.

[6] N. Alif, L. A. Carlsson, and L. Boogh, "The effect of weave pattern and crack propagation direction on mode I delamination resistance of woven glass and carbon composites," *Composites Part B: Engineering*, vol. 29, no. 5, pp. 603–611, 1998.

[7] O. Allix, "A composite damage meso-model for impact problems," *Composites Science and Technology*, vol. 61, no. 15, pp. 2193–2205, 2001.

[8] R. Amacher, J. Cugnoni, J. Botsis, L. Sorensen, W. Smith, and C. Dransfeld, "Thin ply composites: Experimental characterization and modeling of size-effects," *Composites Science and Technology*, vol. 101, no. Supplement C, pp. 121–132, 2014.

[9] J. Andersons and M. König, "Dependence of fracture toughness of composite laminates on interface ply orientations and delamination growth direction," *Composites Science and Technology*, vol. 64, no. 13, pp. 2139 – 2152, 2004.

[10] A. Arteiro, "Structural Mechanics of Thin-Ply Laminated Composites," Ph.D. dissertation, 2016.

[11] A. Arteiro, G. Catalanotti, A. R. Melro, P. Linde, and P. P. Camanho, "Micro-mechanical analysis of the in situ effect in polymer composite laminates," *Composite Structures*, vol. 116, no. Supplement C, pp. 827–840, 2014.

[12] A. Arteiro, G. Catalanotti, J. Xavier, and P. P. Camanho, "Notched response of non-crimp fabric thin-ply laminates: Analysis methods," *Composites Science and Technology*, vol. 88, no. Supplement C, pp. 165–171, 2013.

[13] A. Arteiro, G. Catalanotti, J. Xavier, P. Linde, and P. P. Camanho, "Effect of tow thickness on the structural response of aerospace-grade spread-tow fabrics," *Composite Structures*, vol. 179, no. Supplement C, pp. 208–223, 2017.

[14] A. Arteiro, G. Catalanotti, A. R. Melro, P. Linde, and P. P. Camanho, "Micro-mechanical analysis of the effect of ply thickness on the transverse compressive strength of polymer composites," *Composites Part A: Applied Science and Manufacturing*, vol. 79, no. Supplement C, pp. 127–137, 2015.

[15] "Standard test method for compressive properties of uni-directional or cross-ply fiber-resin composites," ASTM International, West Conshohocken PA, USA, Standard, 1987.

[16] "Standard test method for measuring the damage resistance of a fiber-reinforced polymer matrix composite to a drop-weight impact event," ASTM International, West Conshohocken PA, USA, Standard, 2012.

[17] "Standard test method for compressive residual strength properties of damaged polymer matrix composite plates." ASTM International, West Conshohocken PA, USA, Standard, 2012.

[18] "Standard test method for tensile properties of polymer matrix composite materials." ASTM International, West Conshohocken PA, USA, Standard, 2014.

[19] "Standard test method for in-plane shear response of polymer matrix composite materials by tensile test of a $\pm 45^o$ laminate," ASTM International, West Conshohocken PA, USA, Standard, 2013.

[20] "Standard test method for shear properties of composite materials by the V-notched beam method," ASTM International, West Conshohocken PA, USA, Standard, 2012.

[21] "Standard test method for mode I interlaminar fracture toughness of unidirectional fiber-reinforced polymer matrix composites," ASTM International, West Conshohocken PA, USA, Standard, 2013.

[22] "Standard test method for mixed mode I - mode II interlaminar fracture toughness of unidirectional fiber reinforced polymer matrix composites," ASTM International, West Conshohocken PA, USA, Standard, 2013.

[23] C. Atas and O. Sayman, "An overall view on impact response of woven fabric composite plates," *Composite Structures*, vol. 82, no. 3, pp. 336–345, 2008.

[24] G. Bao and Z. Suo, "Remarks on crack bridging concepts," *Applied Mechanics Reviews*, vol. 45, no. 8, pp. 355–366, 1992.

[25] Z. P. Bažant and P. J, *Fracture and size effect in concrete and other quasi brittle materials*, C. Press, Ed., 1997.

[26] Z. P. Bažant and B. H. Oh, "Crack band theory for fracture of concrete," *Matériaux et Construction*, vol. 16, no. 3, pp. 155–177, 1983.

[27] M. L. Benzeggagh and M. Kenane, "Measurement of mixed-mode delamination fracture toughness of unidirectional glass/epoxy composites with mixed-mode bending apparatus," *Composites Science and Technology*, vol. 56, no. 4, pp. 439–449, 1996.

[28] S. M. Bishop, "Strength and failure of woven carbon-fibre reinforced plastics for high performance applications," *Elsevier Science Publishers, Textile Structural Composites,*, pp. 173–207, 1989.

[29] B. Blinzler and W. Binienda, "Macro-mechanical approach to modeling barely visible damage in braided composites," vol. 27, pp. 466–472, 06 2014.

[30] L. Boniface, P. A. Smith, M. G. Bader, and A. H. Rezaifard, "Transverse Ply Cracking in Cross-Ply CFRP Laminates—Initiation or Propagation Controlled?" *Journal of Composite Materials*, vol. 31, no. 11, pp. 1080–1112, 1997.

[31] R. Borg, L. Nilsson, and K. Simonsson, "Simulating dcb, enf and mmb experiments using shell elements and a cohesive zone model," *Composites Science and Technology*, vol. 64, no. 2, pp. 269 – 278, 2004.

[32] C. Bouvet, B. Castanié, M. Bizeul, and J. Barrau, "Low velocity impact modelling in laminate composite panels with discrete interface elements," *International Journal of Solids and Structures*, vol. 46, no. 14, pp. 2809–2821, 2009.

[33] P. P. Camanho, C. G. Dávila, and M. F. de Moura, "Numerical Simulation of Mixed-Mode Progressive Delamination in Composite Materials," *Journal of Composite Materials*, vol. 37, no. 16, pp. 1415–1438, 2003.

[34] P. P. Camanho, C. G. Dávila, S. T. Pinho, L. Iannucci, and P. Robinson, "Prediction of in situ strengths and matrix cracking in composites under transverse tension and in-plane shear," *Composites Part A: Applied Science and Manufacturing*, vol. 37, no. 2, pp. 165–176, 2006.

[35] P. Camanho, P. Maimí, and C. Dávila, "Prediction of size effects in notched laminates using continuum damage mechanics," *Composites Science and Technology*, vol. 67, no. 13, pp. 2715 – 2727, 2007.

[36] F. Caputo, A. D. Luca, G. Lamanna, R. Borrelli, and U. Mercurio, "Numerical study for the structural analysis of composite laminates subjected to low velocity impact," *Composites Part B: Engineering*, vol. 67, no. Supplement C, pp. 296–302, 2014.

[37] G. Catalanotti, A. Arteiro, M. Hayati, and P. P. Camanho, "Determination of the mode I crack resistance curve of polymer composites using the size-effect law," *Engineering Fracture Mechanics*, vol. 118, no. Supplement C, pp. 49–65, 2014.

[38] G. Catalanotti, C. Furtado, T. Scalici, G. Pitarresi, F. P. van der Meer, and P. P. Camanho, "The effect of through-thickness compressive stress on mode II interlaminar fracture toughness," *Composite Structures*, vol. 182, no. Supplement C, pp. 153–163, 2017.

[39] G. Catalanotti, J. Xavier, and P. P. Camanho, "Measurement of the compressive crack resistance curve of composites using the size effect law," *Composites Part A: Applied Science and Manufacturing*, vol. 56, no. Supplement C, pp. 300–307, 2014.

[40] F. Chang and M. Chen, "The In Situ Ply Shear Strength Distributions in Graphite/Epoxy Laminated Composites," *Journal of Composite Materials*, vol. 21, no. 8, pp. 708–733, 1987.

[41] L. N. S. Chiu, B. G. Falzon, R. Boman, B. Chen, and W. Yan, "Finite element modelling of composite structures under crushing load," *Composite Structures*, vol. 131, no. Supplement C, pp. 215–228, 2015.

[42] A. P. Christoforou and A. S. Yigit, "Characterization of impact in composite plates," *Composite Structures*, vol. 43, no. 1, pp. 15 – 24, 1998.

[43] N. R. Council and Others, *Going to extremes: meeting the emerging demand for durable polymer matrix composites*. National Academies Press, 2005.

[44] B. N. Cox, S. M. Spearing, and D. R. Mumm, "Practical challenges in formulating virtual tests for structural composites," in *Mechanical response of composites*. Springer, 2008, pp. 57–75.

[45] T. D. Dang and S. R. Hallett, "A numerical study on impact and compression after impact behaviour of variable angle tow laminates," *Composite Structures*, vol. 96, no. Supplement C, pp. 194–206, 2013.

[46] L. Daudeville, O. Allix, and P. Ladevèze, "Delamination analysis by damage mechanics: Some applications," *Composites Engineering*, vol. 5, no. 1, pp. 17–24, 1995.

[47] G. A. O. Davies and R. Olsson, "Impact on composite structures," *The Aeronautical Journal (1968)*, vol. 108, no. 1089, p. 541–563, 2004.

[48] C. G. Dávila, P. M. P. R. d. Camanho, A. Turon Travesa *et al.*, "Cohesive elements for shells," © *NASA TP Technical Reports, 2007, núm. 214869*, 2007.

[49] C. G. Dávila, P. P. Camanho, and C. A. Rose, "Failure Criteria for FRP Laminates," *Journal of Composite Materials*, vol. 39, no. 4, pp. 323–345, 2005.

[50] C. G. Dávila, C. A. Rose, and P. P. Camanho, "A procedure for superposing linear cohesive laws to represent multiple damage mechanisms in the fracture of composites," *International Journal of Fracture*, vol. 158, no. 2, pp. 211–223, aug 2009.

[51] A. B. de Morais, M. F. de Moura, A. T. Marques, and P. T. de Castro, "Mode-I interlaminar fracture of carbon/epoxy cross-ply composites," *Composites Science and Technology*, vol. 62, pp. 679–686, 2002.

[52] "Carbon fibre thermosetting resin unidirectional laminates - compression test parallel to fibre direction." Deutsches Institut fur Normung., Standard, 1998.

[53] M. V. Donadon, L. Iannucci, B. G. Falzon, J. M. Hodgkinson, and S. F. M. de Almeida, "A progressive failure model for composite laminates subjected to low velocity impact damage," *Computers & Structures*, vol. 86, no. 11, pp. 1232–1252, 2008.

[54] N. Dourado, M. de Moura, A. B. de Morais, and A. B. Pereira, "Bilinear approximations to the mode II delamination cohesive law using an inverse method," *Mechanics of Materials*, vol. 49, no. Supplement C, pp. 42–50, 2012.

[55] D. Dugdale, "Yielding of steel sheets containing slits," *Journal of the Mechanics and Physics of Solids*, vol. 8, pp. 100–104, 1960.

[56] G. J. Dvorak and N. Laws, "Analysis of Progressive Matrix Cracking In Composite Laminates II. First Ply Failure," *Journal of Composite Materials*, vol. 21, no. 4, pp. 309–329, 1987.

[57] E. Smith, "The size of the fully developed softening zone associated with a crack in a strain-softening material—I. A semi-infinite crack in a remotely loaded infinite solid," *International Journal of Engineering Science*, vol. 27, no. 3, pp. 301–307, 1989.

[58] H. M. EL-Dessouky and C. A. Lawrence, "Ultra-lightweight carbon fibre/thermoplastic composite material using spread tow technology," *Composites Part B*, vol. 50, no. Complete, pp. 91–97, 2013.

[59] A. Faggiani and B. G. Falzon, "Predicting low-velocity impact damage on a stiffened composite panel," *Composites Part A: Applied Science and Manufacturing*, vol. 41, no. 6, pp. 737–749, 2010.

[60] M. L. Falk, A. Needleman, and J. R. Rice, "A critical evaluation of cohesive zone models of dynamic fracture," in *Proceedings of the 5th European mechanics of materials conference on scale transitions from atomistics to continuum plasticity*, 2001, pp. 43–50.

[61] D. Feng and F. Aymerich, "Finite element modelling of damage induced by low-velocity impact on composite laminates," *Composite Structures*, vol. 108, no. Supplement C, pp. 161–171, 2014.

[62] G. Barenblatt, "The mathematical theory of equilibrium cracks in brittle fracture," *Advances in Applied Mechanics*, vol. 7, pp. 55–129, 1962.

[63] E. V. González, "Simulation of interlaminar and intralaminar damage in polymer-based composites for aeronautical applications under impact loading," Ph.D. dissertation, 2011.

[64] E. V. González, P. Maimí, P. P. Camanho, C. S. Lopes, and N. Blanco, "Effects of ply clustering in laminated composite plates under low-velocity impact loading," *Composites Science and Technology*, vol. 71, no. 6, pp. 805–817, 2011.

[65] E. V. González, P. Maimí, P. P. Camanho, A. Turon, and J. A. Mayugo, "Simulation of drop-weight impact and compression after impact tests on composite laminates," *Composite Structures*, vol. 94, no. 11, pp. 3364–3378, 2012.

[66] E. V. González, P. Maimí, A. Turon, P. Camanho, and J. Renart, "Simulation of delamination by means of cohesive elements using an explicit finite element code," *CMC-Computers Materials Continua*, vol. 9, pp. 51–92, 2009.

[67] E. González, P. Maimí, E. Martín-Santos, A. Soto, P. Cruz, F. M. de la Escalera, and J. S. de Aja, "Simulating drop-weight impact and compression after impact tests on composite laminates using conventional shell finite elements," *International Journal of Solids and Structures*, vol. 144-145, pp. 230 – 247, 2018. [Online]. Available: http://www.sciencedirect.com/science/article/pii/S0020768318301902

[68] G.R. Irwin, "Plastic zone near a crack and fracture toughness," in *Proceedings of the Seventh Sagamore Ordenance Materials Conference*, 1960, pp. 63–78.

[69] E. Greenhalgh, C. Meeks, A. Clarke, and J. Thatcher, "The effect of defects on the performance of post-buckled CFRP stringer-stiffened panels," *Composites Part A: Applied Science and Manufacturing*, vol. 34, no. 7, pp. 623–633, 2003.

[70] G. Guillamet, A. Turon, J. Costa, J. Renart, P. Linde, and J. A. Mayugo, "Damage occurrence at edges of non-crimp-fabric thin-ply laminates under off-axis uniaxial loading," *Composites Science and Technology*, vol. 98, no. Supplement C, pp. 44–50, 2014.

[71] Z. Gürdal, R. T. Haftka, and P. Hajela, *Design and optimization of laminated composite materials*. John Wiley & Sons, 1999.

[72] J. Harding, "Impact damage in composite materials," *Science and Engineering of Composite Materials*, vol. 1, no. 2, pp. 41–68, 1989.

[73] P. W. Harper and S. R. Hallett, "Cohesive zone length in numerical simulations of composite delamination," *Engineering Fracture Mechanics*, vol. 75, no. 16, pp. 4774–4792, nov 2008.

[74] V. Hawyes, P. Curtis, and C. Soutis, "Effect of impact damage on the compressive response of composite laminates," *Composites Part A: Applied Science and Manufacturing*, vol. 32, no. 9, pp. 1263 – 1270, 2001.

[75] A. Hillerborg, "Analysis of crack formation and crack growth in concrete by means of fracture mechanics and finite elements," *Cement and Concrete Research*, vol. 6, no. 1, pp. 773–782, 1976.

[76] M. Hinton, A. Kaddour, and P. Soden, "Failure criteria in fibre reinforced polymer composites," *Amsterdam, The Netherlands: Elsevier*, 2004.

[77] N. Hongkarnjanakul, C. Bouvet, and S. Rivallant, "Validation of low velocity impact modelling on different stacking sequences of CFRP laminates and influence of fibre failure," *Composite Structures*, vol. 106, no. Supplement C, pp. 549–559, 2013.

[78] J. P. Hou, N. Petrinic, C. Ruiz, and S. R. Hallett, "Prediction of impact damage in composite plates," *Composites Science and Technology*, vol. 60, no. 2, pp. 273–281, 2000.

[79] H. Hsiao and I. Daniel, "Strain rate behavior of composite materials," *Composites Part B: Engineering*, vol. 29, no. 5, pp. 521 – 533, 1998.

[80] L. Iannucci, "Progressive failure modelling of woven carbon composite under impact," *International Journal of Impact Engineering*, vol. 32, no. 6, pp. 1013–1043, 2006.

[81] S. A. E. International, S. of Automotive Engineers, and N. I. for Aviation Research (U.S.), *Composite Materials Handbook*, ser. Composite Materials Handbook. SAE International, 2012, no. v. 3.

[82] G. Irwin, "Analysis of stresses and strains near to the end of crack traversing a plate," *Journal of Applied Mechanics*, vol. 24, no. 24, pp. 361–364, 1957.

[83] "The determination of the mode II fracture resistance of unidirectional fibre-composites using the calibrated end loaded split C-ELS test and an effective crack length approach." International Organization for Standardization, Geneva, CH, Standard, 2014.

[84] J. Planas and M. Elices, "Nonlinear fracture of cohesive materials," *International Journal of Fracture*, vol. 51, pp. 139–157, 1991.

[85] P. Jerome, "Composite materials in the airbus A380-from history to future," 2001.

[86] A. F. Johnson, A. K. Pickett, and P. Rozycki, "Computational methods for predicting impact damage in composite structures," *Composites Science and Technology*, vol. 61, no. 15, pp. 2183–2192, 2001.

[87] H. E. Johnson, L. A. Louca, S. Mouring, and A. S. Fallah, "Modelling impact damage in marine composite panels," *International Journal of Impact Engineering*, vol. 36, no. 1, pp. 25–39, 2009.

[88] A. B. Kabeel, P. Maimí, N. Gascons, and E. V. González, "Net-tension strength of double lap joints taking into account the material cohesive law," *Composite Structures*, vol. 112, no. Supplement C, pp. 207–213, 2014.

[89] A. M. Kabeel, P. Maimí, N. Gascons, and E. V. González, "Nominal strength of quasi-brittle open hole specimens under biaxial loading conditions," *Composites Science and Technology*, vol. 87, no. Supplement C, pp. 42–49, 2013.

[90] K. Kawabe, T. Matsuo, and Z.-I. Maekawa, "New Technology for Opening Various Reinforcing Fiber Tows," *Journal of the Society of Materials Science, Japan*, vol. 47, no. 7, pp. 727–734, 1998.

[91] J. Kim and M. Scham, "Impact and delamination failure of woven-fabric composites," *Composites Science and Technology*, vol. 60, no. 5, pp. 745–761, 2000.

[92] D. Krajcinovic, "Continuum damage mechanics," *Applied Mechanics Review*, vol. 37, pp. 1–6, 1984.

[93] S. N. Kukureka, C. J. Hooke, M. Rao, P. Liao, and Y. K. Chen, "The effect of fibre reinforcement on the friction and wear of polyamide 66 under dry rolling–sliding contact," *Tribology International*, vol. 32, no. 2, pp. 107–116, 1999.

[94] M. Kutz, *Mechanical Engineers' Handbook, Volume 1: Materials and Engineering Mechanics*, ser. Mechanical Engineers' Handbook. Wiley, 2015.

[95] P. Ladevèze and E. LeDantec, "Damage modelling of the elementary ply for laminated composites," *Composites Science and Technology*, vol. 43, no. 3, pp. 257–267, 1992.

[96] L. Lammerant and I. Verpoest, "Modelling of the interaction between matrix cracks and delaminations during impact of composite plates," *Composites Science and Technology*, vol. 56, no. 10, pp. 1171 – 1178, 1996.

[97] V. Laš and R. Zemčík, "Progressive Damage of Unidirectional Composite Panels," *Journal of Composite Materials*, vol. 42, no. 1, pp. 25–44, 2008.

[98] C. S. Lopes, P. P. Camanho, Z. Gürdal, P. Maimí, and E. V. González, "Low-velocity impact damage on dispersed stacking sequence laminates. Part II: Numerical simulations," *Composites Science and Technology*, vol. 69, no. 7, pp. 937–947, 2009.

[99] C. S. Lopes, S. Sádaba, C. González, J. Llorca, and P. P. Camanho, "Physically-sound simulation of low-velocity impact on fiber reinforced laminates," *International Journal of Impact Engineering*, vol. 92, no. Supplement C, pp. 3–17, 2016.

[100] R. K. Luo, E. R. Green, and C. J. Morrison, "Impact damage analysis of composite plates," *International Journal of Impact Engineering*, vol. 22, no. 4, pp. 435–447, 1999.

[101] P. Maimí, P. P. Camanho, J. A. Mayugo, and C. G. Dávila, "A continuum damage model for composite laminates: Part I – Constitutive model," *Mechanics of Materials*, vol. 39, no. 10, pp. 897–908, 2007.

[102] P. Maimí, P. P. Camanho, J. A. Mayugo, and C. Dávila, "A continuum damage model for composite laminates: Part II – Computational implementation and validation," *Mechanics of Materials*, vol. 39, no. 10, pp. 909–919, 2007.

[103] P. Maimí, P. P. Camanho, J. A. Mayugo, and A. Turon, "Matrix cracking and delamination in laminated composites. Part I: Ply constitutive law, first ply failure and onset of delamination," *Mechanics of Materials*, vol. 43, no. 4, pp. 169–185, 2011.

[104] P. Maimí, E. V. González, N. Gascons, and L. Ripoll, "Size Effect Law and Critical Distance Theories to Predict the Nominal Strength of Quasibrittle Structures," *Applied Mechanics Reviews*, vol. 65, no. 2, p. 020803, may 2013.

[105] B. S. Martin R, Elms T, "Characterization of mode II delamination using the 4ENF," in *In: Proceedings of the 4th European conference on composites: testing and standardisation, Lisbon, 1998*.

[106] E. Martín-Santos, P. Maimí, E. V. González, and P. Cruz, "A continuum constitutive model for the simulation of fabric-reinforced composites," *Composite Structures*, vol. 111, no. Supplement C, pp. 122–129, 2014.

[107] R. Massabò and B. N. Cox, "Concepts for bridged Mode II delamination cracks," *Journal of the Mechanics and Physics of Solids*, vol. 47, pp. 1265–1300, 1999.

[108] A. Matzenmiller, J. Lubliner, and R. L. Taylor, "A constitutive model for anisotropic damage in fiber-composites," *Mechanics of Materials*, vol. 20, no. 2, pp. 125–152, 1995.

[109] P. Mendes and M. V. Donadon, "Numerical prediction of compression after impact behavior of woven composite laminates," *Composite Structures*, vol. 113, no. Supplement C, pp. 476–491, 2014.

[110] Y. Mi, M. A. Crisfield, G. A. O. Davies, and H. B. Hellweg, "Progressive Delamination Using Interface Elements," *Journal of Composite Materials*, vol. 32, no. 14, pp. 1246–1272, 1998.

[111] N. K. Naik and R. Ramasimha, "Estimation of compressive strength of delaminated composites," *Composite Structures*, vol. 52, no. 2, pp. 199–204, 2001.

[112] A. K. Noor, W. S. Burton, and C. W. Bert, "Computational Models for Sandwich Panels and Shells," *Applied Mechanics Reviews*, vol. 49, no. 3, pp. 155–199, mar 1996.

[113] J. Oliver, "A consistent characteristic length for smeared cracking models," *International Journal for Numerical Methods in Engineering*, vol. 28, no. 2, pp. 461–474, 1989.

[114] R. Olsson, "Mass criterion for wave controlled impact response of composite plates," *Composites Part A: Applied Science and Manufacturing*, vol. 31, no. 8, pp. 879 – 887, 2000.

[115] ——, "Analytical prediction of damage due to large mass impact on thin ply composites," *Composites Part A: Applied Science and Manufacturing*, vol. 72, pp. 184–191, 2015.

[116] R. Olsson, F. Ahlqvist, A. André, P. Hellström, E. Alvarez, E. V. González, J. Sainz de Aja, and F. de la Escalera, "Testing and modelling of tension after impact of a thin ply textile composite," in *17th European Conf on Composite Materials. Munich.*, 2016.

[117] R. Olsson, A. André, and P. Hellström, "Analytical modelling and FE simulation of impact response and damage growth in a thin-ply laminate," in *20th Int Conf on Composite Materials. Copenhagen.*, 2015.

[118] R. Olsson, "Analytical prediction of large mass impact damage in composite laminates," *Composites Part A: Applied Science and Manufacturing*, vol. 32, no. 9, pp. 1207–1215, 2001.

[119] R. Olsson, M. V. Donadon, and B. G. Falzon, "Delamination threshold load for dynamic impact on plates," *International Journal of Solids and Structures*, vol. 43, no. 10, pp. 3124–3141, 2006.

[120] A. C. Orifici, I. Herszberg, and R. S. Thomson, "Review of methodologies for composite material modelling incorporating failure," *Composite Structures*, vol. 86, no. 1, pp. 194–210, 2008.

[121] A. Ortega, P. Maimí, E. V. González, J. R. S. de Aja, F. M. de la Escalera, and P. Cruz, "Translaminar fracture toughness of interply hybrid laminates under tensile and compressive loads," *Composites Science and Technology*, vol. 143, no. Supplement C, pp. 1–12, 2017.

[122] A. Ortega, P. Maimí, E. V. González, and D. Trias, "Characterization of the translaminar fracture Cohesive Law," *Composites Part A: Applied Science and Manufacturing*, vol. 91, no. Part 2, pp. 501–509, 2016.

[123] M. Ortiz, "A constitutive theory for the inelastic behavior of concrete," *Mechanics of Materials*, vol. 4, no. 1, pp. 67–93, 1985.

[124] A. Palmer and J. Rice, "The growth of slip surfaces in the progressive failure of over consolidated clay," in *Proceedings of the Royal Society of London*, vol. 548, 1973, pp. 527–548.

[125] A. Parvizi, K. W. Garrett, and J. E. Bailey, "Constrained cracking in glass fibre-reinforced epoxy cross-ply laminates," *Journal of Materials Science*, vol. 13, no. 1, pp. 195–201, jan 1978.

[126] G. Perillo, J. K. Jørgensen, R. Cristiano, and A. Riccio, "A Numerical/Experimental Study on the Impact and CAI Behaviour of Glass Reinforced Composite Plates," *Applied Composite Materials*, jul 2017.

[127] M. F. Pernice, N. V. D. Carvalho, J. G. Ratcliffe, and S. R. Hallett, "Experimental study on delamination migration in composite laminates," *Composites Part A: Applied Science and Manufacturing*, vol. 73, pp. 20 – 34, 2015.

[128] S. Petit, C. Bouvet, A. Bergerot, and J.-J. Barrau, "Impact and compression after impact experimental study of a composite laminate with a cork thermal shield," *Composites Science and Technology*, vol. 67, no. 15, pp. 3286 – 3299, 2007.

[129] S. T. Pinho, P. Robinson, and L. Iannucci, "Fracture toughness of the tensile and compressive fibre failure modes in laminated composites," *Composites Science and Technology*, vol. 66, no. 13, pp. 2069–2079, 2006.

[130] J. Planas and M. Elices, "Asymptotic analysis of a cohesive crack: 1. Theoretical background," *International Journal of Fracture*, vol. 55, no. 2, pp. 153–177, 1992.

[131] S. Psarras, R. Muñoz, M. Ghajari, P. Robinson, D. Furfari, A. Hartwig, and B. Newman, *Compression after multiple impacts: modelling and experimental validation on composite curved stiffened panels*. Smart Intelligent Aircraft Structures (SARISTU): Proceedings of the Final Project Conference. Springer International Publishing, 2016, pp. 681–689.

[132] L. Raimondo, L. Iannucci, P. Robinson, and P. T. Curtis, "A progressive failure model for mesh-size-independent FE analysis of composite laminates subject to low-velocity impact damage," *Composites Science and Technology*, vol. 72, no. 5, pp. 624–632, 2012.

[133] M. M. Rehan, J. Rousseau, X. Gong, L. Guillaumat, and J. Ali, "Effects of fiber orientation of adjacent plies on the mode i crack propagation in a carbon-epoxy laminates," *Procedia Engineering*, vol. 10, pp. 3179 – 3184, 2011, 11th International Conference on the Mechanical Behavior of Materials (ICM11).

[134] A. Riccio, R. Ricchiuto, S. Saputo, A. Raimondo, F. Caputo, V. Antonucci, and V. Lopresto, "Impact behaviour of omega stiffened composite panels," *Progress in Aerospace Sciences*, vol. 81, no. Supplement C, pp. 41–48, 2016.

[135] J. R. Rice, "The initiation and growth of shear bands," *Plasticity and Soil Mechanics*, pp. 263–274, 1973.

[136] S. Rivallant, C. Bouvet, and N. Hongkarnjanakul, "Failure analysis of CFRP laminates subjected to compression after impact: FE simulation using discrete interface elements," *Composites Part A: Applied Science and Manufacturing*, vol. 55, no. Supplement C, pp. 83–93, 2013.

[137] H. Saito, M. Morita, K. Kawabe, M. Kanesaki, H. Takeuchi, M. Tanaka, and I. Kimpara, "Effect of ply-thickness on impact damage morphology in CFRP laminates," *Journal of Reinforced Plastics and Composites*, vol. 30, no. 13, pp. 1097–1106, 2011.

[138] C. Sarrado, A. Turon, J. Costa, and J. Renart, "An experimental analysis of the fracture behavior of composite bonded joints in terms of cohesive laws," *Composites Part A: Applied Science and Manufacturing*, vol. 90, no. Supplement C, pp. 234–242, 2016.

[139] J. C. J. Schellekens and R. de Borst, "A non-linear finite element approach for the analysis of mode-I free edge delamination in composites," *International Journal of Solids and Structures*, vol. 30, no. 9, pp. 1239–1253, 1993.

[140] J. Schön, "Coefficient of friction of composite delamination surfaces," *Wear*, vol. 237, no. 1, pp. 77–89, 2000.

[141] M. Schwab and H. Pettermann, "Modelling and simulation of damage and failure in large composite components subjected to impact loads," *Composite Structures*, vol. 158, pp. 208 – 216, 2016.

[142] M. Schwab, M. Todt, M. Wolfahrt, and H. E. Pettermann, "Failure mechanism based modelling of impact on fabric reinforced composite laminates based on shell elements," *Composites Science and Technology*, vol. 128, no. Supplement C, pp. 131–137, 2016.

[143] T. A. Sebaey, J. Costa, P. Maimí, Y. Batista, N. Blanco, and J. A. Mayugo, "Measurement of the in situ transverse tensile strength of composite plies by means of the real time monitoring of microcracking," *Composites Part B: Engineering*, vol. 65, no. Supplement C, pp. 40–46, 2014.

[144] T. A. Sebaey and E. Mahdi, "Using thin-plies to improve the damage resistance and tolerance of aeronautical CFRP composites," *Composites Part A: Applied Science and Manufacturing*, vol. 86, no. Supplement C, pp. 31–38, 2016.

[145] K. N. Shivakumar, W. Elber, and W. Illg, "Analysis of progressive damage in thin circular laminates due to static-equivalent impact loads," 1983.

[146] G. C. Sih, P. C. Paris, and G. R. Irwin, "On cracks in rectilinearly anisotropic bodies," *International Journal of Fracture Mechanics*, vol. 1, pp. 189–203, 1965.

[147] S. Sihn, R. Y. Kim, K. Kawabe, and S. W. Tsai, "Experimental studies of thin-ply laminated composites," *Composites Science and Technology*, vol. 67, no. 6, pp. 996–1008, 2007.

[148] P. O. Sjoblom, J. T. Hartness, and T. M. Cordell, "On low-velocity impact testing of composite materials," *Journal of composite materials*, vol. 22, no. 1, pp. 30–52, 1988.

[149] E. Smith, "The failure of a strain-softening material: I. Analytical approach for a double cantilever beam specimen," *Theoretical and Applied Fracture Mechanics*, vol. 11, no. 1, pp. 59–64, apr 1989.

[150] X. C. Sun and S. R. Hallett, "Barely visible impact damage in scaled composite laminates: Experiments and numerical simulations," *International Journal of Impact Engineering*, vol. 109, no. Supplement C, pp. 178–195, 2017.

[151] Z. Suo, "Delamination specimens for orthotropic materials," *Journal of Applied Mechanics*, vol. 57, pp. 627–634, 1990.

[152] Z. Suo, G. Bao, and B. Fan, "Delamination R-curve phenomena due to damage," *Journal of the Mechanics and Physics of Solids*, vol. 40, no. 1, pp. 1–16, 1992.

[153] A. Tabiei and R. Tanov, "A nonlinear higher order shear deformation shell element for dynamic explicit analysis:: Part I. Formulation and finite element equations," *Finite Elements in Analysis and Design*, vol. 36, no. 1, pp. 17–37, 2000.

[154] W. Tan, B. G. Falzon, L. N. S. Chiu, and M. Price, "Predicting low velocity impact damage and Compression-After-Impact (CAI) behaviour of composite laminates," *Composites Part A: Applied Science and Manufacturing*, vol. 71, no. Supplement C, pp. 212–226, 2015.

[155] A. Turon, P. P. Camanho, J. Costa, and C. G. Dávila, "A damage model for the simulation of delamination in advanced composites under variable-mode loading," *Mechanics of Materials*, vol. 38, no. 11, pp. 1072–1089, 2006.

[156] A. Turon, P. P. Camanho, J. Costa, and J. Renart, "Accurate simulation of delamination growth under mixed-mode loading using cohesive elements: Definition of interlaminar strengths and elastic stiffness," *Composite Structures*, vol. 92, no. 8, pp. 1857–1864, 2010.

[157] A. Turon, J. Costa, P. P. Camanho, and P. Maimí, "Analytical and Numerical Investigation of the Length of the Cohesive Zone in Delaminated Composite Materials," in *Mechanical response of composites*, S. Netherlands, Ed., 2008, ch. 4, pp. 77–97.

[158] A. Turon, C. Dávila, P. Camanho, and J. Costa, "An engineering solution for mesh size effects in the simulation of delamination using cohesive zone models," *Engineering Fracture Mechanics*, vol. 74, no. 10, pp. 1665–1682, jul 2007.

[159] A. Turon, E. V. González, C. Sarrado, G. Guillamet, and P. Maimí, "Accurate simulation of delamination under mixed-mode loading using a cohesive model with a mode-dependent penalty stiffness," *Composite Structures*, vol. 184, no. Supplement C, pp. 506–511, 2018.

[160] "Aerospace series. carbon fiber laminates. determination of the fibre, resin and void contents." CTN-AENOR, Standard, 1999.

[161] "Plastics - methods for determining the density of non-cellular plastics - part 1: Immersion method, liquid pyknometer method and titration method." CTN-AENOR, Standard, 2004.

[162] U. K. Vaidya, *Impact Response of Laminated and Sandwich Composites*. Vienna: Springer Vienna, 2011, pp. 97–191.

[163] A. Wagih, P. Maimí, N. Blanco, and J. Costa, "A quasi-static indentation test to elucidate the sequence of damage events in low velocity impacts on composite laminates," *Composites Part A: Applied Science and Manufacturing*, vol. 82, no. Supplement C, pp. 180–189, 2016.

[164] A. Wagih, P. Maimí, E. V. González, N. Blanco, J. R. S. de Aja, F. M. de la Escalera, R. Olsson, and E. Alvarez, "Damage sequence in thin-ply composite laminates under out-of-plane loading," *Composites Part A: Applied Science and Manufacturing*, vol. 87, no. Supplement C, pp. 66–77, 2016.

[165] J. D. Whitcomb, "Three-dimensional stress analysis of plain weave composites," in *Composite Materials: Fatigue and Fracture (Third Volume)*. ASTM International, 1991.

[166] K. V. Williams and R. Vaziri, "Application of a damage mechanics model for predicting the impact response of composite materials," *Computers & Structures*, vol. 79, no. 10, pp. 997–1011, 2001.

[167] K. V. Williams, R. Vaziri, and A. Poursartip, "A physically based continuum damage mechanics model for thin laminated composite structures," *International Journal of Solids and Structures*, vol. 40, no. 9, pp. 2267–2300, 2003.

[168] www.boeing.com/commercial/aeromagazine/articles/qtr_4_06/article_04_2.html, 1st May 2018.

[169] Y. Xiong, C. Poon, P. V. Straznicky, and H. Vietinghoff, "A prediction method for the compressive strength of impact damaged composite laminates," *Composite Structures*, vol. 30, no. 4, pp. 357–367, 1995.

[170] Q. Yang, B. Cox, R. Nalla, and R. Ritchie, "Fracture length scales in human cortical bone: The necessity of nonlinear fracture models," *Biomaterials*, vol. 27, pp. 2095–2113, 2006.

[171] A. S. Yigit and A. P. Christoforou, "Limits of asymptotic solutions in low-velocity impact of composite plates," *Composite Structures*, vol. 81, no. 4, pp. 568–574, 2007.

[172] T. Yokozeki, Y. Aoki, and T. Ogasawara, "Experimental characterization of strength and damage resistance properties of thin-ply carbon fiber/toughened epoxy laminates," *Composite Structures*, vol. 82, no. 3, pp. 382–389, 2008.

[173] T. Yokozeki, A. Kuroda, A. Yoshimura, T. Ogasawara, and T. Aoki, "Damage characterization in thin-ply composite laminates under out-of-plane transverse loadings," *Composite Structures*, vol. 93, no. 1, pp. 49–57, 2010.